UiO **: University of Oslo**

Björn Holger Heyn

Geodynamics of Earth's Large Low Shear Velocity Provinces

Interaction with mantle flow, plume initiation, and core-mantle boundary deformation

Thesis submitted for the degree of Philosophiae Doctor

The Centre for Earth Evolution and Dynamics (CEED)
Department of Geosciences
Faculty of Mathematics and Natural Sciences

CEED
The Centre for Earth Evolution and Dynamics

2019

To my family, for teaching me to be curious.

Knowledge is your only wealth that no one can take away

Preface

This thesis is submitted in partial fulfillment of the requirements for the degree of *Philosophiae Doctor* at the University of Oslo. The research presented here is conducted under the supervision of Professor Dr. Clinton P. Conrad, Professor Dr. Reidar G. Trønnes and Dr. Abigail Bull-Aller.

The topic I have been working on in the last three years is at first sight not easy to grasp: the interior of our planet, more specifically the region above the core-mantle boundary more than 2000 km beneath our feet. Most people I have talked to outside geoscience had problems imagining something that deep within the Earth, not even to mention the conditions prevailing there. Most of the time, they looked impressed, but rather lost. And I have to admit: I can understand that. The interior of our planet is a fascinating field of research, but not easy to convey to a broad audience. We have no direct images of the Earth's mantle, for example photos as we can take of stars in space, and convection is so slow that we don't see any significant changes within our lifetime. Sometimes I have the impression that the public knows more about space than about our own planet.

Some people have asked me why I study convection in the Earth's interior, how does it affect our lives? Well, that is a good question, since time scales in the mantle are in the range of millions to billions of years. Yet, the dynamics of Earth's mantle play a crucial role in the evolution of our planet. Plate tectonics, plume-related hotspot volcanism such as Hawaii, and even earthquakes, are consequences of motions in the mantle. Although I do not study these surface expressions, geodynamic models provide a link between them and the deep Earth. Hence, the answer to why I study the lower mantle is: sometimes you have to "dig a little deeper" to find the reason why things are the way they are. Curiosity is a strong driving force, and one of the best reasons to do research.

Although the work presented in this thesis focuses on numerical modeling, it tries to connect material properties expected to result from magma ocean crystallization early in Earth's history to convective evolution and dynamics, and predicts observations that might be used to test this theory. More specifically, the results shown here indicate that lateral viscosity contrasts associated with chemical heterogeneities, which may explain the degree-2 structure of the lower mantle, could be important for the preservation of mantle heterogeneities and can play a role in the initiation of plumes. Short-scale topography of the core-mantle boundary can provide means to measure the respective viscosity variations, and may enable us to predict locations of plume formation.

Acknowledgements

Doing a PhD is an interesting, but also challenging experience. Three years are a short time, yet they involve a lot of up and down between discovery and failure. In order to get through this period, you need people to support you.

First of all, I would like to thank my supervisors **Clint Conrad** and **Reidar Trønnes**. Both of you have been incredibly supportive during my whole PhD. **Clint**, in some way, you have been the ideal supervisor for me. You allowed me to work independently on my own, never forcing me to show my results before I was ready to do so. Still, you have always been there when I had doubts about my work and the quality of my results, giving me helpful feedback and comments. You encouraged me to go on, without ever putting pressure on me, yet gently pushed me out of my comfort zone when it was necessary. Without you, I would not have been able to evolve the way I did during my PhD.
Reidar, I would like to thank you for all the discussions we had, I don't want to miss any of them. I learned so much from you in all those hours that we discussed various topics, covering all kinds of aspects about the core and the mantle. Although you are busy, you always had time when I had a question, explaining patiently the background and implications of your answer. Most of my knowledge about geochemistry and mineral physics comes from what you told me. It is impressive how you can combine results from geochemistry, geodynamics and seismology within a discussion, and your knowledge and understanding of the greater context have been a great inspiration for me.

I am also very grateful to **Abigail Bull**, although she has not been here most of my PhD. Yet, she helped me a lot during the first months after I arrived here. Moreover, she made me aware to this PhD position and gave me the chance to come here. In this context, I also want to thank **Christine Thomas**, who was my supervisor during my masters and has made the contact to Abigail possible. Without the two of you, I might not have ended up at CEED.

CEED has been a fantastic place to work. Right from the beginning, I felt like being part of a big family in which everyone is helping each other. Whatever the problem, you are never left alone to deal with it, and there is always someone to cheer you up. I would like to thank all at CEED for your warm welcome and support, but especially by fellow PhD candidates **Joost**, **Alexandra**, **Eivind**, **Krister**, **Thea** and **Hans Jørgen**. It was always fun to talk to you, and I don't want to miss the time and the laughter we shared.
A special thanks to **Sruthi**, you have been a true friend throughout these three years. No matter what, I could always rely on you. We shared the joys and crises of PhD life, and I am not sure how well I would have managed my PhD without you. Your perspective often helped me to put things into the right context, to see that my problems are not as big as I thought. I am glad we took most courses and excursions together, for they would have been much less fun without you.

I also want to thank **Marcus**, **Denis**, **Kevin**, **Niklas** and **Alex**, my friends back in Münster, Germany. I know that I never managed to keep my promise to visit you during my PhD, and I am sorry for that. I have been thinking about it a couple of times, but in the end I was always too busy to put the plan into action. Yet, you managed that I still feel as part of your group, keeping our friendship alive. I will never forget the Zombicide evenings via Skype, which almost made me forget the distance between us. I hope that I will have more time for you after my PhD, I really miss the time with you to play board games, pool, or just relax at the Aasee.

A special thanks goes to **Elke**, **Svein** and **Oskar**, you have become my "family" far from home. I appreciate the help you gave me in the last three years, your time and the fantastic self-made cake, which gave me the energy to go the extra mile. Living in a foreign country is usually associated with certain challenges, and I am very grateful that you supported me during the process of getting accustomed to Norway. You are one of the reasons why I feel at home in Oslo, and I am very lucky that I have met you.

Finally, I would like to thank **my parents** and **my sister**, who have been my shelter for all storms. Despite the spatial distance, you were always close. Come what may, I knew I would never be alone, a feeling that is worth more than anything else. You have been there in times of joy and celebration, but you also gave me strength and confidence when I was doubting everything, helped me up when I was down. You always believed in me, even in my darkest hours, and encouraged me to go on. Without your support, I would never have been able to finish my PhD.

Björn Holger Heyn
Oslo, October 2019

List of Papers

Paper I

Heyn, Björn H., Conrad, Clinton P. and Trønnes, Reidar G.
Stabilizing Effect of Compositional Viscosity Contrasts on Thermochemical Piles. In: *Geophysical Research Letters* **45** (2018), pp. 7523-7532. doi: 10.1029/2018GL078799.

Paper II

Heyn, Björn H., Conrad, Clinton P. and Trønnes, Reidar G.
How thermochemical piles periodically generate plumes at their edges.
Under review for publication in *Journal of Geophysical Research: Solid Earth*

Paper III

Heyn, Björn H., Conrad, Clinton P. and Trønnes, Reidar G.
Core-mantle boundary topography and its relation to the viscosity structure of the lowermost mantle.
Under review for publication in *Earth and Planetary Science Letters*.

Other papers not included in this thesis

Reiss, Anne-Sophie, Thomas, Christine, van Driel, Jac, and Heyn, Björn
A hot midmantle anomaly in the area of the Indian Ocean Geoid Low.
In: *Geophysical Research Letters* **44** (2017), pp. 6702-6711. doi: 10.1002/2017GL073440.

Trønnes, Reidar G., Baron, Marzena A., Eigenmann, Katarina R., Guren, Marthe G., Heyn, Björn H., Løken, A., and Mohn, Chris E.
Core formation, mantle differentiation and core-mantle interaction within Earth and the terrestrial planets.
In: *Tectonophysics* **760** (2019), pp. 168-198. doi: 10.1016/j.tecto.2018.10.021.

Contents

Chapter 1

Introduction

1.1 The importance of Earth's lowermost mantle, its structure and dynamics

Despite all our technical possibilities, all the equipment that we have invented to investigate our planet and other objects in space, the deep Earth remains a mystery to us. Part of this is due to the fact that we, except for a few diamond inclusions, have no way of getting direct samples or impressions from the deep mantle. As first estimate, we might expect the mantle to be more or less homogeneous after 4.5 Gyr of stirring and mixing, since active convection has a tendency to entrain and distribute heterogeneities. However, analysis of Ocean Island Basalts (OIBs), which are thought to originate from deep-rooted mantle upwellings, show that the mantle must contain reservoirs of material that have escaped extensive mixing over Earth's history (e.g., Weis et al., 2011; Vidito et al., 2013; Jackson et al., 2014; Williams et al., 2015; Harrison et al., 2017). Yet, this type of study does not tell us where chemical heterogeneities can be found within Earth, leaving a broad range of conceptual models (Figure 1.1) to explain the data (Tackley, 2000, 2012; McNamara, 2019).

The early suggestion of stable mantle layering with an upper depleted mantle and a nearly isolated and primordial lower mantle tapped by deep mantle plumes (Wasserburg & DePaolo, 1979, Figure 1.1A) was later deemed untenable based on seismic tomography, showing that slabs penetrate deep into the lower mantle and thus indicating whole-mantle circulation (e.g., van der Hilst et al., 2013, originally published as printed book in AGU's Geodynamics Series, Volume 28, in 1998). However, based on the inferred seismic structure of the lowermost 1000-1500 km of the mantle, Kellogg et al. (1999) and van der Hilst and Kárason (1999) proposed the existence of a convectively isolated and more irregular and dynamically unstable domain with about 4 % density excess in the bottom third of the mantle. Because the range of lateral seismic velocity variations in the lower mantle above the D"-zone (approximately the lowermost 300 km of the mantle) is very small, this division is tenuous. More recently, seismological observations (e.g., Garnero & McNamara, 2008; Garnero et al., 2016; Cottaar & Lekic, 2016; Koelemeijer et al., 2017; McNamara, 2019) and numerical models (e.g., McNamara & Zhong, 2004; Nakagawa & Tackley, 2011; Tackley, 2012; Y. Li et al., 2014, 2015; Mulyukova et al., 2015) have investigated alternative locations, dynamics and properties of such refractory domains. Figure 1.1 (Tackley, 2000) shows six alternative conceptual models for the distribution of primitive or primordial mantle, depleted mantle and accumulations of recycled oceanic crust.
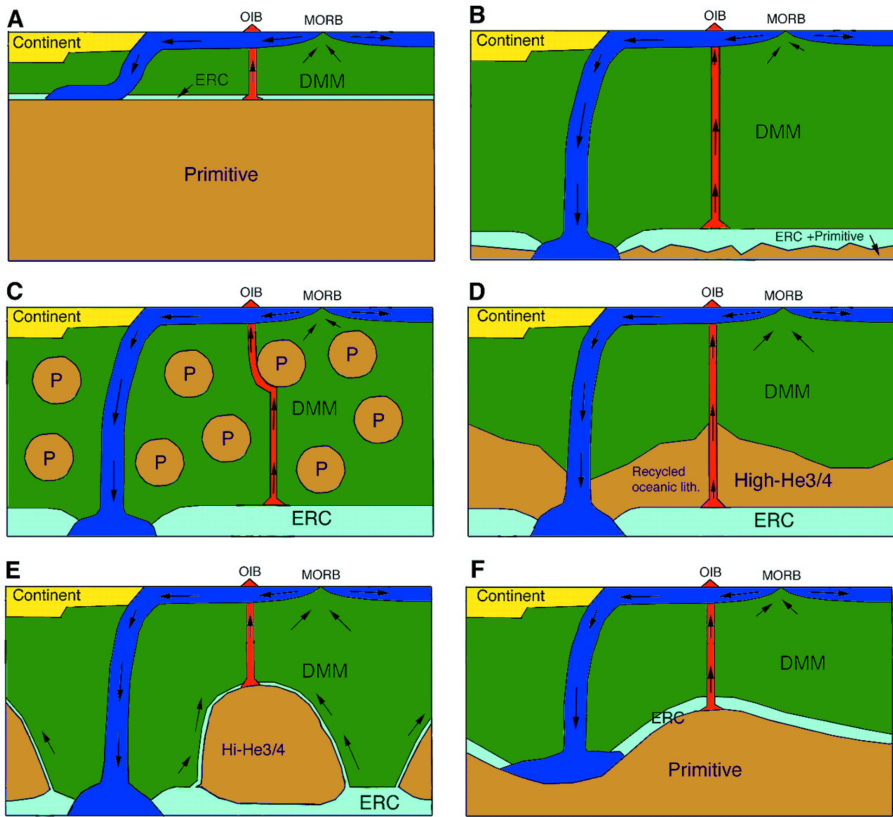
Figure 1.1: Various conceptual models invoked to explain the geochemical signature of ocean island basalts, including layered mantle structures ((A) and (F)), blob-like reservoirs ((C) and (E)), or more pile-shaped features ((B) and (D)), modified after Tackley (2000). Orange areas represent primordial or primitive material, while light blue reservoirs are enriched recycled crust (ERC), and green marks domains of depleted mantle (DMM). Plumes are indicated in red.

Seismic observations and geodynamic models generally agree that the convecting mantle circulation includes the sinking mantle flow under the current and former subduction zone regions in a longitudinal belt through East Asia, Australia, Antarctica, the Americas and the Arctic, a lateral D''-flow towards the two Large Low Shear Velocity Provinces (LLSVPs) under the Pacific and Africa, and ascending flow above the LLSVPs (e.g., Trønnes, 2010; Conrad et al., 2013; Torsvik et al., 2016; McNamara, 2019). The asthenosphere is also part of the convecting mantle cycle, and the degree-2 flow pattern is reflected by the residual geoid (e.g., Hager et al., 1985; Steinberger & Torsvik, 2010). Yet, the two seismically defined LLSVP domains at the core-mantle boundary might be partially isolated from this convective mantle circulation,

likely comprising relatively stable thermochemical piles of Fe-rich cumulates from the late crystallization stage of a basal magma ocean (Labrosse et al., 2007; Trønnes et al., 2019) and/or recycled oceanic crust (ROC, e.g., Hirose et al., 2005; Trønnes et al., 2019). Ballmer et al. (2016), Torsvik et al. (2016) and Torsvik et al. (2019) suggested that the piles might be composite with a viscous and stable sole of bridgmanitic cumulates with overlying and less stable piles dominated by ROC, as discussed later. Another partly isolated reservoir in the lowermost mantle might be the ultra-low velocity zones (ULVZs), which appear to be largely confined to the root zones of major plumes around the LLSVP edges (e.g., McNamara, 2019, and references therein).

In addition to these seismically observed and largely isolated domains, the lower mantle must contain refractory and viscous bridgmanitic blobs or BEAMS (Bridgmanite-Enriched Ancient Mantle Structures Ballmer et al., 2017), which may have originated partly as early cumulates from upper parts of a basal magma ocean (BMO, Labrosse et al., 2007) and partly as residues from early melting and melt extraction above the BMO (Trønnes et al., 2019). Viscous blobs tend to deform slowly (Manga, 1996; Becker et al., 1999; Manga, 2010), and may therefore remain mostly isolated through Earth's history if they are large enough (Becker et al., 1999; Ballmer et al., 2017). Relatively high diffusion rates of the light noble gases in bridgmanite for temperatures close to the liquidus will favor diffusional recharging of primordial-like He and Ne into bridgmanitic domains within 50-500 Myr during the magma ocean stage in the Hadean; significantly lower potential mantle temperatures in the last 4 Gyr, associated with lower diffusion rates, and convective accumulation of small-scale heterogeneities into larger structures would prevent diffusional obliteration of this primordial signal in the bridgmanitic blobs (see Trønnes et al., 2019, for a more detailed discussion). Plume entrainment of some of this refractory bridgmanitic material may explain the high ^{3}He/^{4}He ratios observed in OIBs. In the upper mantle melting zone, the material converted to pyroxenite is less refractory, and melting homogenisation of a large volume of plume material might explain the OIB chemical arrays between a FOZO component with primordial-like He-isotope ratios (Hart et al., 1992), and enriched components.

Seismology is our most important tool to obtain direct observations of mantle structure for the full globe, although results may be limited by the available combinations of earthquakes and receivers. Seismic data can give us an impression of how the structure of the mantle looks like today, but there are a few limitations in itself: (1) The data we obtain is only a snapshot in time and does not tell us how the current state evolved or how the evolution began; (2) Both tomography and body wave studies have a resolution which is limited to a few hundred to thousands of kilometers in the lowermost mantle (Schlaphorst et al., 2015; Cottaar & Lekic, 2016). Normal mode data has even lower lateral sensitivity and is best used to infer long-wavelength structures (Koelemeijer et al., 2012, 2017). (3) Seismic velocities depend on bulk and shear moduli, and density. As both composition and temperature can affect density

3

and the elastic properties, wave velocities cannot be uniquely converted into mantle structure, and obtaining viscosities is impossible. As a consequence, seismology does provide observations of Earth's internal structure, but is often not able to discriminate between different potential explanations for a given structure (Ritsema et al., 2007; Bull et al., 2009; Schuberth, Bunge, & Ritsema, 2009), for example between plume clusters (Figure 1.2a) and thermochemical piles (Figure 1.2b-d). The former are accumulations of plumes swept together by mantle flow, with the low velocities being explained by thermal effects alone (e.g., Schuberth, Bunge, Steinle-Neumann, et al., 2009; Davies et al., 2012), while the latter comprises chemically distinct material and may exhibit different types of piles with respect to form, stability and dynamics (Figure 1.2b-d), and compositions.
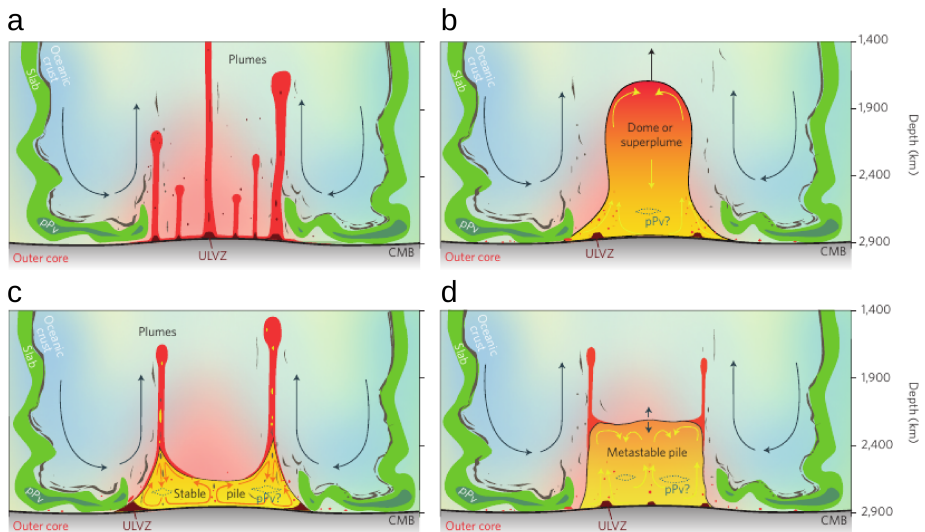
Figure 1.2: Conceptual models of a plume cluster (a) and various types of thermochemical piles, depending on their excess density ((b)-(d)), after Garnero et al. (2016). For low excess densities, thermochemical material may form domes or superplumes (b), that can rise and sink depending on their thermal evolution, while higher densities result in metastable (d) to stable (c) piles. Ultra-low velocity zones (ULVZs) seem to reside predominantly at the base of mantle plumes. Post-bridgmanite (pPv) is expected to be present in subducted slabs (dark green areas), but may also form within the thermochemical piles (dashed regions).

In combination with seismology, geochemical experiments and geodynamic modeling can provide the required additional insight into deep Earth structure and dynamics. While the former can give information about the composition and phase relations of minerals (see e.g., Trønnes et al., 2019, and references therein), the latter can be used to investigate the evolution of (a fictive) Earth

over time (e.g., McNamara & Zhong, 2004; Nakagawa & Tackley, 2011; M. Li & McNamara, 2013; Y. Li et al., 2014; Mulyukova et al., 2015). Yet, neither experiments (or ab initio computations) nor numerical modeling can fully capture Earth's complexities as all experiments or models are bases on assumptions and simplifications defined in their setup. For geodynamic models, this includes, for example, the initial condition or the distribution of chemical and rheological heterogeneities, which are treated as variable parameters in the models. Furthermore, for deep Earth, both geochemistry and geodynamics can only predict likely scenarios given the respective circumstances (e.g. initial condition, material, structure), but depend on seismic observations for confirmation due to the lack of more direct measurements.

In short, seismology provides the observations but fails to give the explanation, while geochemistry and geodynamics provide possible solutions that require observations to discriminate between them. As a consequence, we have to combine seismological observations with data obtained from geochemistry and the results of geodynamic models to gain a more complete understanding of the interior our planet. Thus, although the work presented here focuses on the modeling part, we tried to use constraints from geochemistry to justify our choices, and, where applicable, predict potential observations that could be confirmed by seismology.

1.1.1 LLSVPs and their properties

Although we know little about the deep mantle, it is expected to play a crucial role in the evolution of our planet. Tomographic images reveal a strong degree-2 structure of the lowermost mantle (Figure 1.3), with very strong perturbations in velocities between the so-called **L**arge **L**ow **S**hear **V**elocity **P**rovinces (LLSVPs) and the belt of high velocities between them (Garnero & McNamara, 2008; Dziewonski et al., 2010; Cottaar & Lekic, 2016; Garnero et al., 2016). The edges of these LLSVPs are thought to be the source locations of deep-roted mantle upwellings, which express themselves in eruptions of Large Igneous Provinces (LIPs), kimberlites and long-lived hotspots (Torsvik et al., 2006, 2010; French & Romanowicz, 2015). As mentioned above, geochemistry of Ocean Island Basalts (OIBs) shows that their source material is different from that of mid-ocean ridge basalts, indicating contributions from a primordial and other partly isolated reservoir deep in the mantle (Weis et al., 2011; Vidito et al., 2013; Jackson et al., 2014; Williams et al., 2015). Some of the hotspots, like Hawaii or Galapagos, even develop two or three parallel chains of islands with different magma compositions with respect to enrichment in incompatible elements (Weis et al., 2011; Jackson et al., 2014; Harrison et al., 2017). The enriched trend seemingly faces the projected margin of the LLSVPs, leading to the suggestion that the (bilateral) zoning is caused by entrainment of LLSVP material in plumes (compare also Figure 1.6). Numerical models have shown this to be a feasible explanation (e.g., Dannberg & Gassmöller, 2018; Farnetani et al., 2018).
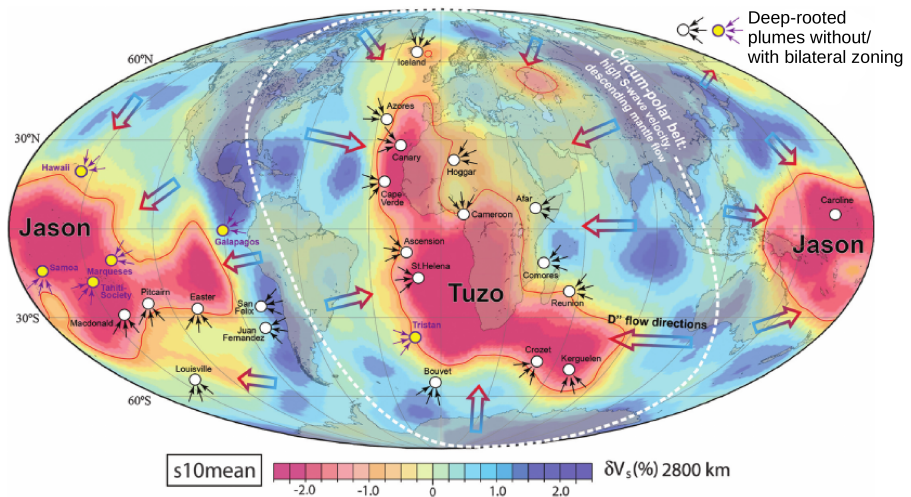
Figure 1.3: Seismic tomography model s10mean (Doubrovine et al., 2016), showing the two Large Low Shear Velocity Provinces (LLSVPs) in red and the belt of subduction with fast velocities surrounding them in blue. Deep-rooted plumes from French and Romanowicz (2015) are indicated by circles, with purple marking plumes with bilateral zoning. Modified after Torsvik et al. (2016).

In order to explain primordial signals and different types of enrichment in plumes, we would require respective reservoirs that are partially isolated from mantle convection and mixing. As outlined above, primordial ^{3}He/^{4}He ratios are best explained by bridgmanitic blobs (BEAMS) consisting of early cumulates formed during the Hadean or early Archean, since the fractionation of the main radioactive elements U and Th into melt would destroy any primordial He-signal in the residual BMO (Corgne et al., 2005; Trønnes et al., 2019). Other types of enrichment in plumes likely originates from the LLSVPs, representing a reservoir of recycled oceanic crust (ROC) and/or iron-enriched late-stage cumulates of the basal magma ocean (Labrosse et al., 2007; Trønnes et al., 2019). The latter would have to survive billions of years as (more or less) coherent structure at the base of the mantle without taking active part in mantle convection. Based on their composition, both basaltic and iron-rich bridgmanitic material are expected to have a density and/or viscosity contrast relative to the ambient mantle (see discussion about LLSVP origin further down).

Numerical studies have shown that a certain chemical excess density is required to avoid extensive erosion and mixing of pile material due to thermal buoyancy within 4 Gyr (see e.g. review by Tackley, 2012). Thermal and compositonal viscosity contrasts play a slightly more ambiguous role (Davaille et al., 2002; Tackley, 2012; Y. Li et al., 2014). Several numerical studies have indicated that a strong temperature-dependence of viscosity is crutial for pile

stability, whereas compositional viscosity contrasts play a minor role in these cases (e.g., McNamara & Zhong, 2004; Y. Li et al., 2014). On the other hand, analogue models have indicated that the pile viscosity may be more important than previously thought, although the density contrast remains the controlling parameter for pile survival (e.g., Davaille et al., 2002). In Paper I, we show, based on numerical models, that there is a trade-off between the three parameters (excess density, thermal viscosity contrast, compositonal viscosity contrast) in terms of the survival of pile material over billions of years of active mantle convection.

1.1.2   LLSVPs and locations of plumes

One of the most important questions about the deep mantle is how plate tectonics may be linked to the structure and dynamics of the LLSVPs and the circum-polar high-velocity belt (Figure 1.3). It is usually thought that the positions of subduction zones dictate where the pile material is located, and most geodynamic models show that subduction history plays an important role in focusing the piles in present-day locations (Davies et al., 2012; Bull et al., 2014; M. Li & Zhong, 2017). It has even been suggested that the lower mantle structure might alternate between degree-1 and the current degree-2 structure during supercontinent cycles (Zhong et al., 2007; Zhong & Liu, 2016), although this hypothesis has been questioned (Bull et al., 2014). Such a change would require to split up a single large pile into two by a subducted slab dropping on top of the pile. Yet, the degree-2 structure in seismic tomography including the high-velocity circum-polar belt with sinking slabs covering several hundered million years is very dominant (Figure 1.3). Some studies even indicate that the presence of upwelling associated with LLSVPs may reverse the dip direction of subducted slabs in the lower mantle, as observed for a slab associated with the subduction of the Thetys ocean in the southern Indian Ocean (Wang et al., 2018). Moreover, reconstructions of eruption sites of LIPS and kimberlites (e.g., Torsvik et al., 2006, 2010, 2016; Torsvik, 2019) and net plate motions during the last 250 Myrs (Conrad et al., 2013) indicate that the LLSVPS, and as such the centres of upwelling and plate divergence, have been stable for at least 250-300 Myrs. This is also confirmed by reconstructed paths of True Polar Wander (TPW), which reflect changes in Earth's rotation axis due to changes of mass within the Earth (e.g., Dziewonski et al., 2010). Since these paths are confined to areas where seismic tomography indicates sinking slabs, Dziewonski et al. (2010) suggested that LLSVPs might be the controlling parameter in global plate tectonics by localising upward and downward flow.

The correlation between LLSVP margins and the eruption sites of hotspots and LIPs (Doubrovine et al., 2016; Torsvik et al., 2016, 2019) requires a mechanism that explains how plumes predominantly form and rise at the margins of dense piles. Lateral flow along the CMB induced by sinking slabs tends to push rising plumes towards the LLSVP edges, but may not be sufficient to reproduce the observations for plumes initated randomly from a growing thermal

boundary layer (M. Li & Zhong, 2017, 2019). Hence, plume formation directly at the pile margins might be a more viable explanation. In fact, the presence of a dense pile at the base of the mantle is expected to force the lateral flow upwards at the pile edges, which may eventually give rise to plumes (e.g., Torsvik et al., 2016; Dannberg & Gassmöller, 2018). However, this passive effect of dense piles is not the only possible mechanism of plume initiation at LLSVP margins, since piles can interact with the rising plumes (M. Li et al., 2018). In Paper II, we show that a local collapse of the pile margin can provide a mechanisms for (periodic) plume generation directly at the edges of LLSVPs that may explain the observed correlation.

1.1.3 Deformation of the core-mantle boundary

Apart from affecting the surface by localising upwellings, the lower mantle may also affect the outer core via coupling across the core-mantle boundary. Although a chemical exchange reaction might have been quite active in early Earth, it probably came to an end when the basal magma ocean crystallized (Trønnes et al., 2019). However, mantle flow can deform the boundary between the viscous mantle and the liquid outer core (Figure 1.4), similar to deformations observed at the Earth's surface (e.g., Yoshida, 2008; Tanaka, 2010; Koelemeijer et al., 2012; Schlaphorst et al., 2015; Deschamps et al., 2017). Since convection in the outer core is responsible for Earth's magnetic field, undulations in the core-mantle boundary might cause turbulence or introduce a torque in core flow (Burmann & Noir, 2018; Glane & Buffett, 2018) and be related to secular variations in Earth's magentic field (Roberts & Aurnou, 2012). The torque due to CMB topography has also been invoked to explain exchange of angular momentum between the core and the mantle, which is reflected in the length of day (LOD) variations (Ding & Chao, 2018; Glane & Buffett, 2018). The effect of torque exchange between mantle and core may even be enhanced by the presence of a stable compositional stratification of the outer core, as indicated by Glane and Buffett (2018). Seismic velocity profiles of Earth's outer core have been hinting at the presence of a stagnant E' layer for a long time (see e.g. Trønnes et al., 2019, and references therein). More recently, geochemical experiments have confirmed the plausibility of exchange reactions between the core and the mantle during the basal magma ocean stage, thereby providing a mechanism to form such a stable layer (Trønnes et al., 2019).

Motivated by its potential influence on core convection, core-mantle boundary topography has been studied using seismic methods (e.g., Tanaka, 2010; Koelemeijer et al., 2012; Schlaphorst et al., 2015) and geodynamic models (e.g., Yoshida, 2008; Deschamps et al., 2017), with focus on long wavelengths resolvable with normal modes and body waves (Tanaka, 2010; Koelemeijer et al., 2012). Since CMB topography is caused by density heterogeneities and associated radial mantle flow (Figure 1.4), amplitudes, which locally scale with viscosity, and patterns of topography can also be used to get constraints the viscosity and density structure of the lowermost mantle. While we can get additional
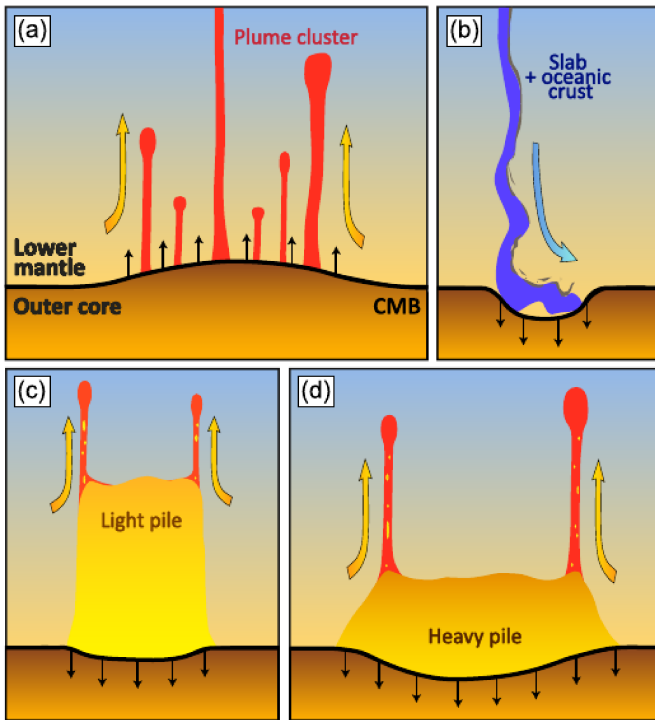
Figure 1.4: Schematic illustration of expected CMB topography for plume clusters (a), downwellings associated with slabs (b), and different types of thermochemical piles ((c) and (d)), after Deschamps et al. (2017). While plume clusters will cause an elevation of the CMB due to light, rising flow, sinking slabs or dense piles will depress the CMB.

information on the excess density of piles from normal model data (Ishii & Tromp, 1999; Moulik & Ekström, 2016; Koelemeijer et al., 2017) and Earth's tides (Lau et al., 2017), CMB topography may be the best available proxy for the viscosity structure. In Paper III, we demonstrate that short-wavelength topography at the margins of dense piles is sensitive to compositional viscosity contrasts between pile and ambient mantle, while the pile density and the viscosity drop across the hot lower thermal boundary layer are insignificant. Hence, if seismically observed, this characteristic topography would provide additional insight into pile material and properties.

1.2   Origin of LLSVPs

As indicated above, LLSVPs have been suggested to be chemically distinct in order to explain their existence, properties and the different compositions of Ocean Island Basalts (OIBs). Yet, the origin and composition of LLSVPs is still debated. In the following, I will give a short overview over current LLSVP

hypotheses and explain why the assumption of increased density and viscosity is reasonable. A more extensive discussion of the different hypotheses can be found in Garnero et al. (2016), McNamara (2019) and Trønnes et al. (2019), and references therein.

1.2.1 Thermal origin

Since a reduction in shear wave velocity, which is the main characteristic of the LLSVPs, can also be explained by increased temperature, some studies have suggested that LLSVPs are simply a cluster of hot mantle upwellings (compare Figure 1.2a) swept together by mantle flow (Schuberth, Bunge, & Ritsema, 2009; Schuberth, Bunge, Steinle-Neumann, et al., 2009; Schuberth et al., 2012; Davies et al., 2012). Davies et al. (2012) have shown that recent subduction history can focus upwellings in the regions of current-day LLSVPs. Moreover, seismic observations, such as sharp edges with respect to elastic properties or anticorrelation of bulk sound and shear wave velocities, have also been tried to explain by thermal effects alone (Schuberth, Bunge, Steinle-Neumann, et al., 2009; Schuberth et al., 2012; Davies et al., 2012). However, plume clusters would be highly time-dependent and therefore may not be able to explain why observed plumes and plume-related eruptions (LIPs and kimberlites) cluster at the LLSVP margins (e.g., Torsvik et al., 2010; Torsvik, 2019), although this correlation has been questioned as well (Austermann et al., 2014; Davies et al., 2015).

In addition, most tomographic models show a much stronger velocoty perturbation in the lowermost few hundred kilometers of the LLSVP regions than in the upper part of the lower mantle (e.g., Koelemeijer et al., 2015), which may be seen as indication that the lowermost LLSVPs are chemically distinct. In fact, studies using normal models (Koelemeijer et al., 2017) and Earth's solid tides (Lau et al., 2017) tried to estimate the excess density of LLSVPs and obtained results of approximately neutral to about 0.5-1% denser LLSVPs, respectively. However, these estimates include both the effect of thermal expansion (making hot material lighter) and a potential chemical density increase, and average over up to 1000 km (Lau et al., 2017). Consequently, neither of the methods are able to exclude an approximately 100 km thick dense base of LLSVPs (Koelemeijer et al., 2017).

1.2.2 Thermochemical origin

Apart from the correlation between LLSVP margins and erupted LIPs, arguments in favor of a thermochemical origin of LLSVPs come from seismological observations and geochemistry. From a seismological perspective, both the sharp edges and the anticorrelation of velocities may easily be explained by the effect of composition, especially enrichment in iron (Bull et al., 2009; Trønnes et al., 2019). An increased iron content would also explain the excess density that is required in geodynamic models to keep the material at the base of the mantle and avoid complete entrainment (e.g., Tackley, 2012; Y. Li et al., 2014; Heyn et

al., 2018). Furthermore, the presence of dense piles may explain the stability of a degree-2 structure in the lower mantle for at least about 250-300 Myrs (Torsvik et al., 2010; Conrad et al., 2013; Torsvik, 2019), and the (presumed) correlation between LLSVP edges and eruption sites of LIPs and kimberlites (Torsvik et al., 2006, 2010, 2016; Torsvik, 2019). Two potential candidate materials have been suggested, primordial iron-rich cumulates or recycled oceanic crust, which are discussed in more detail below.

For the models presented in the papers, we assume a thermochemical origin of LLSVPs, with a focus on primordial material. However, our results are also more or less directly applicable to piles of recycled oceanic crust, depending on their properties (density, viscosity). A more detailed discussion of the influence of pile material on our model results is given in the respective papers. In Paper III, we predict a CMB topography pattern that may be used to test the validity of the hypothesis of thermochemical piles (rather than plume clusters) based on associated viscosity contrasts.

1.2.2.1 Dense cumulates

Iron-enrichment of LLSVP material is strongly supported by the geochemistry of Earth's mantle. Based on partitioning coefficients of various elements under realistic Earth-like conditions, it has been shown that the crystallization of the magma ocean after the moon-forming event has likely produced a basal and an outer magma ocean (Labrosse et al., 2007; Trønnes et al., 2019). This could have been caused by the magma ocean adiabat crossing the curved peridotite liquidus at about 1800 km depth, inducing the first crystallization there (Stixrude et al., 2009; Trønnes et al., 2019). Bridgmanite crystals formed below and above the neutral buoyancy level would float and sink, respectively, to that level. Alternatively, without an initial bridgmanite-melt density crossover within the mantle pressure range, the magma ocean would have started to crystallize at the CMB. The bridgmanite-melt Fe/Mg partitioning, resulting in a rapid increase in the Fe/Mg ratio of the melt, however, would soon lead to melt migration towards the CMB and a neutral buoyancy level migrating upwards with progressive solidification. In either case, solidification of the magma ocean (MO) would therefore lead to a basal magma ocean (BMO, Figure 1.5), which would be partially insulated and therefore long-lived (Labrosse et al., 2007; Trønnes et al., 2019). Without an extensive core-BMO chemical exchange (see below), the residual BMO material would have developed a rapidly increasing Fe/Mg ratio and crystallized both bridgmanite (bm) and ferropericlase.

The high temperatures during core formation in large terrestrial planets like Earth and Venus would have driven the equilibrium $2Fe^{core} + SiO_2^{MO} = Si^{core} + 2FeO^{MO}$ to the product side (right-hand side), resulting in high Si-content in the core, combined with high oxygen fugacity (i.e. high FeO-content) in the MO. As the Earth cooled, the same equilibrium would have been displaced towards the reactants (left-hand side), setting the stage for the diffusional
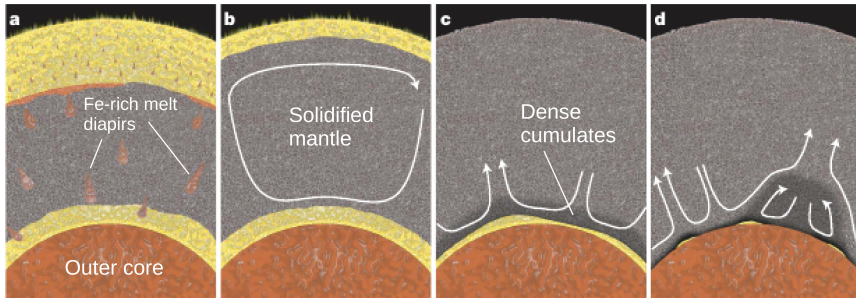
Figure 1.5: The concept of magma ocean crystallization after Labrosse et al. (2007), starting from the mid-mantle and creating two seperate layers of remaining melt (yellow regions): the outer and the basal magma ocean. While the magma ocean at the surface would solidify rather quickly, the basal magma ocean lasts longer and would provide the iron-enriched material of LLSVPs.

migration of FeO from the magma ocean (and later the BMO) to the core, and SiO_2 in the opposite direction (e.g., Trønnes et al., 2019). The phase relations in the system Fe-Si-O may also indicate that silica could have crystallized in the core and floated up to and dissolved into the BMO melt (Hirose et al., 2017). The BMO-core exchange of FeO and SiO_2 would have increased the Si/(Fe+Mg) and Mg/Fe ratios of the basal magma ocean, and thereby promoted more extensive bridgmanite crystallization. Since the viscosity of ferro-periclase is significantly lower than that of bridgmanite, the enrichment in bridgmanite also increases the viscosity of the LLSVP material (Trønnes et al., 2019). As a consequence, LLSVPs resulting from a basal magma ocean are likely to be dense and viscous.

1.2.2.2 Recycled oceanic crust

The other material that is abundant in the lowermost mantle is basaltic crust brought down to the CMB by the subduction of oceanic plates. The basaltic oceanic crust may segregate from the lithospheric mantle under lower mantle conditions (Hirose et al., 2005, see Figure 1.6A) and accumulate over time at the base of the mantle (M. Li & McNamara, 2013; M. Li et al., 2014; Mulyukova et al., 2015; McNamara, 2019). Due to its composition including both bridgmanite and a high-pressure polymorph of silica, basaltic material is expected to have increased bulk modulus (Ballmer et al., 2016; Garnero et al., 2016; Trønnes et al., 2019) and may have increased viscosity as well. Yet, due to a significant lower enrichment in iron, its excess density is likely small, resulting in neutral to slightly negative buoyancy at lowermost mantle conditions (M. Li & McNamara, 2013; Ballmer et al., 2016; Trønnes et al., 2019). This may cause difficulties in accumulating enough material to form stable LLSVPs (M. Li & McNamara, 2013), but basaltic crust may still be one of the components of LLSVPs, e.g. as a layer above a primordial base (Ballmer et al., 2016; Torsvik et al., 2016, compare also Figure 1.6).
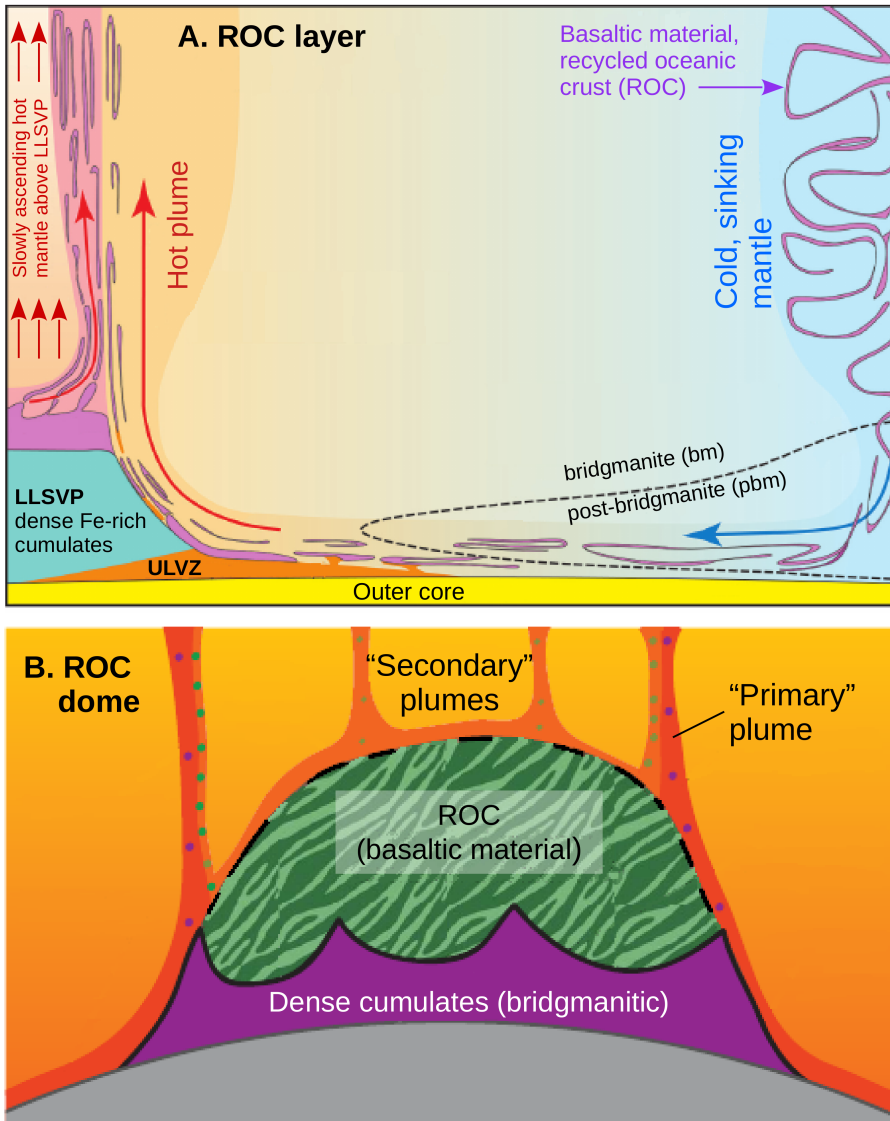
Figure 1.6: Two concepts of a heterogeneous internal structure of LLSVPs, including both primordial material and recycled oceanic crust (after (A) Torsvik et al. (2016) and (B) Ballmer et al. (2016)). The latter may form a layer or dome on top of the iron-enriched dense cumulates. Plumes may entrain either or both components, depending on where they rise, with the enriched side of the conduit facing the LLSVPs. Internally zoned plumes may explain the observed bilateral zoning of hotspot tracks at the surface (e.g., Weis et al., 2011; Dannberg & Gassmöller, 2018).

1.3 Methodology

In the following part, I briefly outline the method of geodynamic modeling used in this work. To this end, I will describe the basic equations, whose derivation can be found in the literature (e.g., Schubert et al., 2001). There, you will also find the full Navier-Stokes equation for fluid dynamics, which in this case is simplified to the conservation equation of momentum (Equation (1.2)). In the second part, I will discuss the setup of meshes, as this is an important parameter in geodynamic studies. Yet, I will not touch the finite element method itself or how this is implemeneted in the community codes we use, as this discussion would go beyond the scope of this work. Details about numerical methods and their mathematical background can be found in the respective code descriptions and references therein (Zhong et al., 2000; Tan et al., 2006; Kronbichler et al., 2012; Heister et al., 2017; Bangerth et al., 2018, 2019).

1.3.1 Governing equations

To investigate convective behavior inside Earth's mantle over time, we run numerical simulations using the community codes CitcomS (Zhong et al., 2000; Tan et al., 2006) and ASPECT (Kronbichler et al., 2012; Heister et al., 2017; Bangerth et al., 2018, 2019). These codes solve the conservation equations of mass, momentum and energy (temperature) (Equations (1.1) to (1.3))

$$\nabla \cdot (\rho \mathbf{u}) = 0, \tag{1.1}$$

$$-\nabla \cdot \left[2\eta \left(\frac{1}{2}(\nabla \mathbf{u} + \nabla \mathbf{u}^T) - \frac{1}{3}(\nabla \cdot \mathbf{u})\mathbf{I} \right) \right] + \nabla p = \rho \mathbf{g}, \tag{1.2}$$

$$\rho C_P \left(\frac{\partial T}{\partial t} + \mathbf{u} \cdot \nabla T \right) - \nabla \cdot k \nabla T = \rho H + \Phi + \alpha T (\mathbf{u} \cdot \nabla p) + Q_L, \tag{1.3}$$

for a mesh of finite elements. Parameters in these equations are velocity $\mathbf{u}$, density ρ, viscosity η, unity matrix $\mathbf{I}$, pressure p, gravitational acceleration $\mathbf{g}$, specific heat capacity C_P, temperature T, thermal diffusivity k, internal heating H, thermal expansivity α, viscous dissipation heating Φ and latent heat due to phase transitions Q_L. Equation (1.2) is a force balance between viscous forces associated with deformation of the fluid, separated into shear deformation ($\frac{1}{2}(\nabla \mathbf{u} + \nabla \mathbf{u}^T)$) and volume changes $\frac{1}{3}(\nabla \cdot \mathbf{u})\mathbf{I}$, pressure forces ∇p and gravity forces $\rho \mathbf{g}$. Inertia forces included in the full Navier-Stokes equation can be neglected in mantle convection due to the high viscosity of the mantle fluid.

In our simulations, we use the Boussinesq approximation, which assumes that the material is incompressible ($\nabla \cdot \mathbf{u} = 0$), i.e. that the volume of fluid elements does not change. As a consequence, density variations are ignored except for the buoyancy term $\rho \mathbf{g}$ on the right-hand side of Equation (1.2). We further assume that we can describe density variations due to temperature by the linear relation $\rho(T) = \rho_0 - \alpha \rho_0 (T - T_0)$ with reference density ρ_0 obtained

at a reference temperature T_0, and that the pressure $p = p' + \bar{p}$ can be split into a dynamic, p', and a hydrostatic part, $\bar{p} = \rho_0 g$. Thus, we can simplify the set of Equations (1.1) to (1.3) to

$$\nabla \cdot \mathbf{u} = 0 \tag{1.4}$$

$$-\nabla \cdot \left[2\eta \left(\frac{1}{2} (\nabla \mathbf{u} + \nabla \mathbf{u}^T) \right) \right] + \nabla p' = -\alpha \rho_0 T \mathbf{g} \tag{1.5}$$

$$\rho C_P \left(\frac{\partial T}{\partial t} + \mathbf{u} \cdot \nabla T \right) - \nabla \cdot k \nabla T = \rho H. \tag{1.6}$$

For a more detailed discussion of the basic equations, their approximations and how they are solved, see e.g., Schubert et al. (2001) and Bangerth et al. (2019).

Compositional fields, which represent the material of dense thermochemical piles (LLSVPs) in our models, are either introduced as active tracer particles as in CitcomS (McNamara & Zhong, 2004) or as dynamic fields as in ASPECT using the Discontinous Galerkin Method (He et al., 2017). For the former, particles with prescribed properties (e.g. density and viscosity) are advected with the flow and their influence on the convection is evaluated by the tracer-ratio method (Tackley & King, 2003), for which the ratio between normal (tracer value 0) and enriched (tracer value 1) tracers is calculated for each cell. Cell properties are then modified by the obtained ratio. For dynamic fields, the conservation equation for each compositonal field c_i

$$\frac{\partial c_i}{\partial t} + \mathbf{u} \cdot \nabla c_i \tag{1.7}$$

is solved for each time step. As the field representing LLSVPs is characterized by increased density relative to the ambient mantle ($\Delta \rho_C$), we have to account for this effect on density in the buoyancy term in Equation (1.5), which is modified to

$$-\nabla \cdot \left[2\eta \left(\frac{1}{2} (\nabla \mathbf{u} + \nabla \mathbf{u}^T) \right) \right] + \nabla p' = (-\alpha \rho_0 T + C \Delta \rho_C) \mathbf{g}. \tag{1.8}$$

1.3.2 Mesh design

The meshes on which these equations are solved can be defined in two ways: static or adaptive meshes. Static meshes are defined by the user via a certain number of nodes (CitcomS), which will then remain static throughout the whole simulation time. In these cases, the user has to make sure that individual cells of the mesh have a reasonable aspect ratio, i.e. are close to square elements (in 2-D, approximately cubic elements in 3-D), as elongated elements can have an undesired effect on the observed dynamics. The aspect ratio of cells is especially important for studies in which entrainment and mixing play a significant role, e.g. studies about LLSVP survival and stability, since elongated mesh elements may considerably over- or underestimate entrainment. Although meshes are static and do not change with time, they can easily be refined in radial (or

vertical) direction at the base (Figure 1.7) or the top of the domain (as done e.g. in Y. Li et al., 2014, 2015; Heyn et al., 2018). Such a refinement is helpful to increase resolution in areas where plate deformation (top) or LLSVP entrainment (base) are most important, while keeping computation times within a reasonable range. Yet, the refinement area has to be set properly a priori, thus a reasonable knowledge of overall dynamics (or respective test runs) are necessary to find a good trade-off between resolution and computation time. The advantage of these static meshes is that each mesh node is always at the same position in space and the number of nodes remains constant, which simplifies post-processing of data.
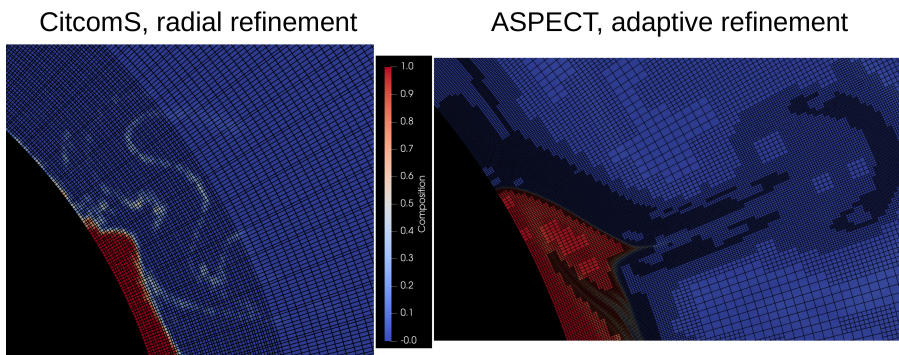
Figure 1.7: Different mesh types for models using CitcomS (left) and ASPECT (right), shown for a zoom-in on the margin of thermochemical piles. For CitcomS, meshes are refined radially in the lowermost 800 km, while ASPECT uses adaptive mesh refinement based on specific refinement criteria, e.g. compositional gradients. As can be seen, meshes for CitcomS are regular, but elements are not preserving a square-shape everywhere, i.e. cells are becoming more rectangular higher up in the mantle. In contrast, ASPECT cells are always close to quadratic, but meshes are very irregular.

In contrast to CitcomS, ASPECT uses so-called adaptive meshes. The base of this mesh type is a very coarse mesh with almost square (cubic) cells that is refined a specified number of times before the first time step by dividing each cell into four for every refinement level (initial refinement). During the simulation, refinement is then adjusted within a certain fraction (refinement and coarsening fraction) based on user-specified criteria, for example compositional or viscosity gradients. Cells are then coarsened in the fraction of the domain where the specified criteria are least important, while meshes are refined in regions where the criteria are important (Figure 1.7). A constant minimum refinement level determines the lowest mesh resolution. Since this type of mesh is dynamically determined and adjusted at specific times during the simulation, both number and position of mesh nodes vary significantly during model run time. As a consequence, post-processing of data, e.g. calculations of LLSVP volumes and masses, is made more complicated by the highly variable meshes.

1.4 Summary of Papers

Paper I We use the convection code CitcomS to address the requirements of dense primordial material to survive 4.5 Gyr of convection without being mixed into the background mantle. Based on our simulations of a wide parameter range of viscosity and density contrasts, we identify a new trade-off between density and viscosity structure required for thermochemical LLSVPs to survive billions of years of mantle convection.

A higher intrinsic viscosity of dense material can become crucial for rather small density contrasts to avoid rapid entrainment, especially during periods of strong pile deformation. The latter may be related to changes in subduction configuration during supercontinent cycles, e.g. a slab dropping on top of a pile and splitting it up, or during the formation of the thermochemical piles after magma ocean crystallization. In contrast, chemical viscosity contrasts play a less important role for large excess densities of pile material or a strong temperature-dependence of viscosity.

Paper II In this paper, we aim at understanding the mechanism of plume formation and the role of thermochemical piles in this process. For the first time, we are able to show why and how plumes may preferentially form and rise at the margins of thermochemical piles. In our ASPECT models, plumes are periodically initiated at margins of thermochemical piles (LLSVPs) by a local collapse of the pile edge before they would naturally arise from the lower thermal boundary layer.

Plumes rising at the pile margin increase the local pile thickness for a few hundred million years, until the plume is pushed towards the pile interior by lateral mantle flow and the plume strength at the plume root decreases. The collapsing pile spreads along the core-mantle boundary and increases the thermal boundary layer thickness outside its margin. Thus, periods of plume initiation for a constant subduction configuration reflect the strength of the lateral flow along the core-mantle boundary, which is controlled by the sinking rate of slabs in the lower mantle and the subduction velocity. Another reason for a pile collapse can be a change in subduction configuration. The latter may be related to retreating subduction zones or a decrease in subduction flux, e.g. during a supercontinent cycle, and may cause accumulations of plumes in spatial and temporal proximity.

Paper III We use ASPECT model to investigate undulations of the core-mantle boundary and their relation to the properties of thermochemical piles, with a focus on short wavelengths that are more sensitive to viscosity heterogeneities. As we discover, CMB topography at length scales of approximately 100 km can provide a tool to discriminate between thermal and thermochemical structures, which may finally answer the question of LLSVP origin, and to get better constraints on lower mantle viscosity structure.

If the piles have a higher intrinsic viscosity than the ambient mantle, a characteristic short-scale (about 80-120 km wide) depression will form just outside the LLSVP margins, which is related to a relative uplift of the pile margin and a wegde of thermal boundary layer material that is compressed against the dense pile. As a stiffer pile focuses more stresses outside its margin, depth and symmetry of this valley can tell us more about the relative viscosity contrasts in the deep Earth. Detection of this characteristic topography may be possible with core-reflected waves or correlated noise.

References

Austermann, J., Kaye, B. T., Mitrovica, J. X., & Huybers, P. (2014, 01). A statistical analysis of the correlation between large igneous provinces and lower mantle seismic structure. *Geophysical Journal International*, *197*(1), 1–9. Retrieved from https://doi.org/10.1093/gji/ggt500 doi: 10.1093/gji/ggt500

Ballmer, M. D., Houser, C., Hernlund, J. W., Wentzcovitch, R. M., & Hirose, K. (2017, February). Persistence of strong silica-enriched domains in the earth's lower mantle. *Nature Geoscience*, *10*, 236. Retrieved from https://www.nature.com/articles/ngeo2898#supplementary-information doi: 10.1038/ngeo2898; 10.1038/ngeo2898

Ballmer, M. D., Schumacher, L., Lekic, V., Thomas, C., & Ito, G. (2016). Compositional layering within the large low shear-wave velocity provinces in the lower mantle. *Geochemistry, Geophysics, Geosystems*, *17*(12), 5056–5077. Retrieved from https://agupubs.onlinelibrary.wiley.com/doi/abs/10.1002/2016GC006605 doi: 10.1002/2016GC006605

Bangerth, W., Dannberg, J., Gassmoeller, R., Heister, T., et al. (2018, June). *ASPECT v2.0.1 [software].* Davis, CA. Retrieved from https://doi.org/10.5281/zenodo.1297145 doi: 10.5281/zenodo.1297145

Bangerth, W., Dannberg, J., Gassmöller, R., Heister, T., et al. (2019, April). ASPECT: Advanced solver for problems in earth's convection, user manual. Retrieved from https://doi.org/10.6084/m9.figshare.4865333 (doi:10.6084/m9.figshare.4865333) doi: 10.6084/m9.figshare.4865333

Becker, T. W., Kellogg, J. B., & O'Connell, R. J. (1999). Thermal constraints on the survival of primitive blobs in the lower mantle. *Earth and Planetary Science Letters*, *171*(3), 351–365. Retrieved from http://www.sciencedirect.com/science/article/pii/S0012821X99001600 doi: 10.1016/S0012-821X(99)00160-0

Bull, A. L., Domeier, M., & Torsvik, T. H. (2014). The effect of plate motion history on the longevity of deep mantle heterogeneities. *Earth and Planetary Science Letters*, *401*, 172–182. Re-

trieved from `http://www.sciencedirect.com/science/article/pii/S0012821X14003859` doi: 10.1016/j.epsl.2014.06.008

Bull, A. L., McNamara, A. K., & Ritsema, J. (2009). Synthetic tomography of plume clusters and thermochemical piles. *Earth and Planetary Science Letters*, *278*(3), 152–162. Retrieved from `http://www.sciencedirect.com/science/article/pii/S0012821X08007309` doi: 10.1016/j.epsl.2008.11.018

Burmann, F., & Noir, J. (2018). Effects of bottom topography on the spin-up in a cylinder. *Physics of Fluids*, *30*(10), 106601. Retrieved from `https://doi.org/10.1063/1.5051111` doi: 10.1063/1.5051111

Conrad, C. P., Steinberger, B., & Torsvik, T. H. (2013, June). Stability of active mantle upwelling revealed by net characteristics of plate tectonics. *Nature*, *498*, 479–482. Retrieved from `https://www.nature.com/articles/nature12203#supplementary-information` doi: 10.1038/nature12203; 10.1038/nature12203

Corgne, A., Liebske, C., Wood, B. J., Rubie, D. C., & Frost, D. J. (2005). Silicate perovskite-melt partitioning of trace elements and geochemical signature of a deep perovskitic reservoir. *Geochimica et Cosmochimica Acta*, *69*(2), 485–496. Retrieved from `http://www.sciencedirect.com/science/article/pii/S0016703704005381` doi: 10.1016/j.gca.2004.06.041

Cottaar, S., & Lekic, V. (2016, 08). Morphology of seismically slow lower-mantle structures. *Geophysical Journal International*, *207*(2), 1122–1136. Retrieved from `https://doi.org/10.1093/gji/ggw324` doi: 10.1093/gji/ggw324

Dannberg, J., & Gassmöller, R. (2018). Chemical trends in ocean islands explained by plume–slab interaction. *Proceedings of the National Academy of Sciences*, *115*(17), 4351–4356. Retrieved from `https://www.pnas.org/content/115/17/4351` doi: 10.1073/pnas.1714125115

Davaille, A., Girard, F., & Bars, M. L. (2002). How to anchor hotspots in a convecting mantle? *Earth and Planetary Science Letters*, *203*(2), 621–634. Retrieved from `http://www.sciencedirect.com/science/article/pii/S0012821X0200897X` doi: 10.1016/S0012-821X(02)00897-X

Davies, D. R., Goes, S., Davies, J., Schuberth, B., Bunge, H.-P., & Ritsema, J. (2012). Reconciling dynamic and seismic models of earth's lower mantle: The dominant role of thermal heterogeneity. *Earth and Planetary Science Letters*, *353-354*, 253–269. Retrieved from `http://www.sciencedirect.com/science/article/pii/S0012821X1200444X` doi: 10.1016/j.epsl.2012.08.016

Davies, D. R., Goes, S., & Sambridge, M. (2015). On the relationship between volcanic hotspot locations, the reconstructed eruption sites of large igneous provinces and deep mantle seismic structure. *Earth and Planetary Science Letters*, *411*, 121–130. Retrieved from `http://www.sciencedirect.com/science/article/pii/S0012821X14007523` doi: 10.1016/j.epsl.2014.11.052

Deschamps, F., Rogister, Y., & Tackley, P. J. (2017, 09). Constraints

on core–mantle boundary topography from models of thermal and thermochemical convection. *Geophysical Journal International*, *212*(1), 164–188. Retrieved from `https://doi.org/10.1093/gji/ggx402` doi: 10.1093/gji/ggx402

Ding, H., & Chao, B. F. (2018). A 6-year westward rotary motion in the earth: Detection and possible micg coupling mechanism. *Earth and Planetary Science Letters*, *495*, 50–55. Retrieved from `http://www.sciencedirect.com/science/article/pii/S0012821X18302802` doi: 10.1016/j.epsl.2018.05.009

Doubrovine, P. V., Steinberger, B., & Torsvik, T. H. (2016). A failure to reject: Testing the correlation between large igneous provinces and deep mantle structures with edf statistics. *Geochemistry, Geophysics, Geosystems*, *17*(3), 1130–1163. Retrieved from `https://agupubs.onlinelibrary.wiley.com/doi/abs/10.1002/2015GC006044` doi: 10.1002/2015GC006044

Dziewonski, A. M., Lekic, V., & Romanowicz, B. A. (2010). Mantle anchor structure: An argument for bottom up tectonics. *Earth and Planetary Science Letters*, *299*(1), 69–79. Retrieved from `http://www.sciencedirect.com/science/article/pii/S0012821X10005236` doi: 10.1016/j.epsl.2010.08.013

Farnetani, C. G., Hofmann, A. W., Duvernay, T., & Limare, A. (2018). Dynamics of rheological heterogeneities in mantle plumes. *Earth and Planetary Science Letters*, *499*, 74–82. Retrieved from `http://www.sciencedirect.com/science/article/pii/S0012821X1830428X` doi: 10.1016/j.epsl.2018.07.022

French, S. W., & Romanowicz, B. (2015, September). Broad plumes rooted at the base of the earth's mantle beneath major hotspots. *Nature*, *525*, 95. Retrieved from `https://www.nature.com/articles/nature14876#supplementary-information` doi: 10.1038/nature14876; 10.1038/nature14876

Garnero, E. J., & McNamara, A. K. (2008). Structure and dynamics of earth's lower mantle. *Science*, *320*(5876), 626–628. Retrieved from `https://science.sciencemag.org/content/320/5876/626` doi: 10.1126/science.1148028

Garnero, E. J., McNamara, A. K., & Shim, S.-H. (2016, June). Continent-sized anomalous zones with low seismic velocity at the base of earth's mantle. *Nature Geoscience*, *9*, 481–489. Retrieved from `https://www.nature.com/articles/ngeo2733#supplementary-information` doi: 10.1038/ngeo2733; 10.1038/ngeo2733

Glane, S., & Buffett, B. (2018). Enhanced core-mantle coupling due to stratification at the top of the core. *Frontiers in Earth Science*, *6*, 171. Retrieved from `https://www.frontiersin.org/article/10.3389/feart.2018.00171` doi: 10.3389/feart.2018.00171

Hager, B. H., Clayton, R. W., Richards, M. A., Comer, R. P., & Dziewonski, A. M. (1985). Lower mantle heterogeneity, dynamic topography and the geoid. *Nature*, *313*(6003), 541–545. doi: 10.1038/313541a0; 10.1038/313541a0

Harrison, L. N., Weis, D., & Garcia, M. O. (2017). The link between

hawaiian mantle plume composition, magmatic flux, and deep mantle geodynamics. *Earth and Planetary Science Letters*, *463*, 298–309. Retrieved from `http://www.sciencedirect.com/science/article/pii/S0012821X17300390` doi: 10.1016/j.epsl.2017.01.027

Hart, S. R., Hauri, E. H., Oschmann, L. A., & Whitehead, J. A. (1992). Mantle plumes and entrainment: Isotopic evidence. *Science*, *256*(5056), 517–520. Retrieved from `http://www.jstor.org/stable/2877213`

He, Y., Puckett, E. G., & Billen, M. I. (2017). A discontinuous Galerkin method with a bound preserving limiter for the advection of non-diffusive fields in solid earth geodynamics. *Physics of the Earth and Planetary Interiors*, *263*, 23–37. Retrieved from `https://doi.org/10.1016/j.pepi.2016.12.001` doi: 10.1016/j.pepi.2016.12.001

Heister, T., Dannberg, J., Gassmöller, R., & Bangerth, W. (2017). High accuracy mantle convection simulation through modern numerical methods. II: Realistic models and problems. *Geophysical Journal International*, *210*(2), 833–851. Retrieved from `https://doi.org/10.1093/gji/ggx195` doi: 10.1093/gji/ggx195

Heyn, B. H., Conrad, C. P., & Trønnes, R. G. (2018). Stabilizing effect of compositional viscosity contrasts on thermochemical piles. *Geophysical Research Letters*, *45*(15), 7523–7532. Retrieved from `https://agupubs.onlinelibrary.wiley.com/doi/abs/10.1029/2018GL078799` doi: 10.1029/2018GL078799

Hirose, K., Morard, G., Sinmyo, R., Umemoto, K., Hernlund, J., Helffrich, G., & Labrosse, S. (2017, February). Crystallization of silicon dioxide and compositional evolution of the earth's core. *Nature*, *543*, 99–102. doi: 10.1038/nature21367; 10.1038/nature21367

Hirose, K., Takafuji, N., Sata, N., & Ohishi, Y. (2005). Phase transition and density of subducted morb crust in the lower mantle. *Earth and Planetary Science Letters*, *237*(1), 239–251. Retrieved from `http://www.sciencedirect.com/science/article/pii/S0012821X0500419X` doi: 10.1016/j.epsl.2005.06.035

Ishii, M., & Tromp, J. (1999). Normal-mode and free-air gravity constraints on lateral variations in velocity and density of earth's mantle. *Science*, *285*(5431), 1231–1236. Retrieved from `https://science.sciencemag.org/content/285/5431/1231` doi: 10.1126/science.285.5431.1231

Jackson, M. G., Hart, S. R., Konter, J. G., Kurz, M. D., Blusztajn, J., & Farley, K. A. (2014, October). Helium and lead isotopes reveal the geochemical geometry of the samoan plume. *Nature*, *514*, 355–358. Retrieved from `https://www.nature.com/articles/nature13794#supplementary-information` doi: 10.1038/nature13794; 10.1038/nature13794

Kellogg, L. H., Hager, B. H., & van der Hilst, R. D. (1999). Compositional stratification in the deep mantle. *Science*, *283*(5409), 1881–1884. Retrieved from `https://science.sciencemag.org/content/283/5409/1881` doi: 10.1126/science.283.5409.1881

Koelemeijer, P. J., Deuss, A., & Ritsema, J. (2017, May). Density structure

of earth's lowermost mantle from stoneley mode splitting observations. *Nature Communications*, *8*, 15241. Retrieved from `https://www.nature.com/articles/ncomms15241#supplementary-information` doi: 10.1038/ncomms15241; 10.1038/ncomms15241

Koelemeijer, P. J., Deuss, A., & Trampert, J. (2012, 07). Normal mode sensitivity to earth's d layer and topography on the core-mantle boundary: what we can and cannot see. *Geophysical Journal International*, *190*(1), 553–568. Retrieved from `https://doi.org/10.1111/j.1365-246X.2012.05499.x` doi: 10.1111/j.1365-246X.2012.05499.x

Koelemeijer, P. J., Ritsema, J., Deuss, A., & van Heijst, H.-J. (2015, 12). Sp12rts: a degree-12 model of shear- and compressional-wave velocity for earth's mantle. *Geophysical Journal International*, *204*(2), 1024–1039. Retrieved from `https://doi.org/10.1093/gji/ggv481` doi: 10.1093/gji/ggv481

Kronbichler, M., Heister, T., & Bangerth, W. (2012). High accuracy mantle convection simulation through modern numerical methods. *Geophysical Journal International*, *191*, 12–29. Retrieved from `http://dx.doi.org/10.1111/j.1365-246X.2012.05609.x` doi: 10.1111/j.1365-246X.2012.05609.x

Labrosse, S., Hernlund, J. W., & Coltice, N. (2007, December). A crystallizing dense magma ocean at the base of the earth's mantle. *Nature*, *450*, 866–869. Retrieved from `https://www.nature.com/articles/nature06355#supplementary-information` doi: 10.1038/nature06355; 10.1038/nature06355

Lau, H. C. P., Mitrovica, J. X., Davis, J. L., Tromp, J., Yang, H.-Y., & Al-Attar, D. (2017, November). Tidal tomography constrains earth's deep-mantle buoyancy. *Nature*, *551*, 321–326. doi: 10.1038/nature24452; 10.1038/nature24452

Li, M., & McNamara, A. K. (2013). The difficulty for subducted oceanic crust to accumulate at the earth's core-mantle boundary. *Journal of Geophysical Research: Solid Earth*, *118*(4), 1807–1816. Retrieved from `https://agupubs.onlinelibrary.wiley.com/doi/abs/10.1002/jgrb.50156` doi: 10.1002/jgrb.50156

Li, M., McNamara, A. K., & Garnero, E. J. (2014, March). Chemical complexity of hotspots caused by cycling oceanic crust through mantle reservoirs. *Nature Geoscience*, *7*, 366–370. Retrieved from `https://www.nature.com/articles/ngeo2120#supplementary-information` doi: 10.1038/ngeo2120; 10.1038/ngeo2120

Li, M., & Zhong, S. (2017). The source location of mantle plumes from 3d spherical models of mantle convection. *Earth and Planetary Science Letters*, *478*, 47–57. Retrieved from `http://www.sciencedirect.com/science/article/pii/S0012821X17304806` doi: 10.1016/j.epsl.2017.08.033

Li, M., & Zhong, S. (2019). Lateral motion of mantle plumes in 3-d geodynamic models. *Geophysical Research Letters*, *46*(9), 4685–4693. Retrieved from `https://agupubs.onlinelibrary.wiley.com/doi/abs/10.1029/2018GL081404` doi: 10.1029/2018GL081404

Li, M., Zhong, S., & Olson, P. (2018). Linking lowermost mantle structure, core-mantle boundary heat flux and mantle plume formation. *Physics of the Earth and Planetary Interiors*, *277*, 10–29. Retrieved from `http://www.sciencedirect.com/science/article/pii/S0031920117302625` doi: 10.1016/j.pepi.2018.01.010

Li, Y., Deschamps, F., & Tackley, P. J. (2014, 09). The stability and structure of primordial reservoirs in the lower mantle: insights from models of thermochemical convection in three-dimensional spherical geometry. *Geophysical Journal International*, *199*(2), 914–930. Retrieved from `https://doi.org/10.1093/gji/ggu295` doi: 10.1093/gji/ggu295

Li, Y., Deschamps, F., & Tackley, P. J. (2015). Effects of the post-perovskite phase transition properties on the stability and structure of primordial reservoirs in the lower mantle of the earth. *Earth and Planetary Science Letters*, *432*, 1–12. Retrieved from `http://www.sciencedirect.com/science/article/pii/S0012821X15006159` doi: 10.1016/j.epsl.2015.09.040

Manga, M. (1996). Mixing of heterogeneities in the mantle: Effect of viscosity differences. *Geophysical Research Letters*, *23*(4), 403–406. Retrieved from `https://agupubs.onlinelibrary.wiley.com/doi/abs/10.1029/96GL00242` doi: 10.1029/96GL00242

Manga, M. (2010). Low-viscosity mantle blobs are sampled preferentially at regions of surface divergence and stirred rapidly into the mantle. *Physics of the Earth and Planetary Interiors*, *180*(1), 104–107. Retrieved from `http://www.sciencedirect.com/science/article/pii/S0031920110000476` doi: 10.1016/j.pepi.2010.02.013

McNamara, A. K. (2019). A review of large low shear velocity provinces and ultra low velocity zones. *Tectonophysics*, *760*, 199–220. Retrieved from `http://www.sciencedirect.com/science/article/pii/S0040195118301586` (Linking Plate Tectonics and Volcanism to Deep Earth Dynamics – a tribute to Trond H. Torsvik) doi: 10.1016/j.tecto.2018.04.015

McNamara, A. K., & Zhong, S. (2004). Thermochemical structures within a spherical mantle: Superplumes or piles? *Journal of Geophysical Research: Solid Earth*, *109*(B7). Retrieved from `https://agupubs.onlinelibrary.wiley.com/doi/abs/10.1029/2003JB002847` doi: 10.1029/2003JB002847

Moulik, P., & Ekström, G. (2016). The relationships between large-scale variations in shear velocity, density, and compressional velocity in the earth's mantle. *Journal of Geophysical Research: Solid Earth*, *121*(4), 2737–2771. Retrieved from `https://agupubs.onlinelibrary.wiley.com/doi/abs/10.1002/2015JB012679` doi: 10.1002/2015JB012679

Mulyukova, E., Steinberger, B., Dabrowski, M., & Sobolev, S. V. (2015). Survival of llsvps for billions of years in a vigorously convecting mantle: Replenishment and destruction of chemical anomaly. *Journal of Geophysical Research: Solid Earth*, *120*(5), 3824–3847. Retrieved from `https://agupubs.onlinelibrary.wiley.com/doi/abs/10.1002/2014JB011688` doi: 10.1002/2014JB011688

Nakagawa, T., & Tackley, P. J. (2011). Effects of low-viscosity post-perovskite on thermo-chemical mantle convection in a 3-d spherical shell. *Geophysical Research Letters*, *38*(4). Retrieved from `https://agupubs.onlinelibrary.wiley.com/doi/abs/10.1029/2010GL046494` doi: 10.1029/2010GL046494

Ritsema, J., McNamara, A. K., & Bull, A. L. (2007). Tomographic filtering of geodynamic models: Implications for model interpretation and large-scale mantle structure. *Journal of Geophysical Research: Solid Earth*, *112*(B1). Retrieved from `https://agupubs.onlinelibrary.wiley.com/doi/abs/10.1029/2006JB004566` doi: 10.1029/2006JB004566

Roberts, P. H., & Aurnou, J. M. (2012). On the theory of core-mantle coupling. *Geophysical & Astrophysical Fluid Dynamics*, *106*(2), 157–230. Retrieved from `https://doi.org/10.1080/03091929.2011.589028` doi: 10.1080/03091929.2011.589028

Schlaphorst, D., Thomas, C., Holme, R., & Abreu, R. (2015, 12). Investigation of core–mantle boundary topography and lowermost mantle with p4kp waves. *Geophysical Journal International*, *204*(2), 1060–1071. Retrieved from `https://doi.org/10.1093/gji/ggv496` doi: 10.1093/gji/ggv496

Schubert, G., Turcotte, D., & Olson, P. (2001). *Mantle convection in the earth and planets.* Cambridge University Press. Retrieved from `https://books.google.no/books?id=2lwnV2xCMmoC`

Schuberth, B. S. A., Bunge, H.-P., & Ritsema, J. (2009). Tomographic filtering of high-resolution mantle circulation models: Can seismic heterogeneity be explained by temperature alone? *Geochemistry, Geophysics, Geosystems*, *10*(5). Retrieved from `https://agupubs.onlinelibrary.wiley.com/doi/abs/10.1029/2009GC002401` doi: 10.1029/2009GC002401

Schuberth, B. S. A., Bunge, H.-P., Steinle-Neumann, G., Moder, C., & Oeser, J. (2009). Thermal versus elastic heterogeneity in high-resolution mantle circulation models with pyrolite composition: High plume excess temperatures in the lowermost mantle. *Geochemistry, Geophysics, Geosystems*, *10*(1). Retrieved from `https://agupubs.onlinelibrary.wiley.com/doi/abs/10.1029/2008GC002235` doi: 10.1029/2008GC002235

Schuberth, B. S. A., Zaroli, C., & Nolet, G. (2012, 03). Synthetic seismograms for a synthetic earth: long-period p- and s-wave traveltime variations can be explained by temperature alone. *Geophysical Journal International*, *188*(3), 1393–1412. Retrieved from `https://doi.org/10.1111/j.1365-246X.2011.05333.x` doi: 10.1111/j.1365-246X.2011.05333.x

Steinberger, B., & Torsvik, T. H. (2010). Toward an explanation for the present and past locations of the poles. *Geochemistry, Geophysics, Geosystems*, *11*(6). Retrieved from `https://agupubs.onlinelibrary.wiley.com/doi/abs/10.1029/2009GC002889` doi: 10.1029/2009GC002889

Stixrude, L., de Koker, N., Sun, N., Mookherjee, M., & Karki, B. B. (2009). Thermodynamics of silicate liquids in the deep earth. *Earth and Planetary Science Letters*, *278*(3), 226–232. Retrieved from `http://www.sciencedirect.com/science/article/pii/`

S0012821X08007565 doi: 10.1016/j.epsl.2008.12.006

Tackley, P. J. (2000). Mantle convection and plate tectonics: Toward an integrated physical and chemical theory. *Science*, *288*(5473), 2002–2007. Retrieved from https://science.sciencemag.org/content/288/5473/2002 doi: 10.1126/science.288.5473.2002

Tackley, P. J. (2012). Dynamics and evolution of the deep mantle resulting from thermal, chemical, phase and melting effects. *Earth-Science Reviews*, *110*(1), 1–25. Retrieved from http://www.sciencedirect.com/science/article/pii/S0012825211001486 doi: 10.1016/j.earscirev.2011.10.001

Tackley, P. J., & King, S. D. (2003). Testing the tracer ratio method for modeling active compositional fields in mantle convection simulations. *Geochemistry, Geophysics, Geosystems*, *4*(4). Retrieved from https://agupubs.onlinelibrary.wiley.com/doi/abs/10.1029/2001GC000214 doi: 10.1029/2001GC000214

Tan, E., Choi, E., Thoutireddy, P., Gurnis, M., & Aivazis, M. (2006). Geoframework: Coupling multiple models of mantle convection within a computational framework. *Geochemistry, Geophysics, Geosystems*, *7*(6). Retrieved from https://agupubs.onlinelibrary.wiley.com/doi/abs/10.1029/2005GC001155 doi: 10.1029/2005GC001155

Tanaka, S. (2010). Constraints on the core-mantle boundary topography from p4kp-pcp differential travel times. *Journal of Geophysical Research: Solid Earth*, *115*(B4). Retrieved from https://agupubs.onlinelibrary.wiley.com/doi/abs/10.1029/2009JB006563 doi: 10.1029/2009JB006563

Torsvik, T. H. (2019). Earth history: A journey in time and space from base to top. *Tectonophysics*, *760*, 297–313. Retrieved from http://www.sciencedirect.com/science/article/pii/S0040195118303147 (Linking Plate Tectonics and Volcanism to Deep Earth Dynamics – a tribute to Trond H. Torsvik) doi: 10.1016/j.tecto.2018.09.009

Torsvik, T. H., Burke, K., Steinberger, B., Webb, S. J., & Ashwal, L. D. (2010, July). Diamonds sampled by plumes from the core–mantle boundary. *Nature*, *466*, 352–355. Retrieved from https://www.nature.com/articles/nature09216#supplementary-information doi: 10.1038/nature09216; 10.1038/nature09216

Torsvik, T. H., Smethurst, M. A., Burke, K., & Steinberger, B. (2006). Large igneous provinces generated from the margins of the large low-velocity provinces in the deep mantle. *Geophysical Journal International*, *167*(3), 1447–1460. Retrieved from https://onlinelibrary.wiley.com/doi/abs/10.1111/j.1365-246X.2006.03158.x doi: 10.1111/j.1365-246X.2006.03158.x

Torsvik, T. H., Steinberger, B., Ashwal, L. D., Doubrovine, P. V., & Trønnes, R. G. (2016). Earth evolution and dynamics—a tribute to kevin burke. *Canadian Journal of Earth Sciences*, *53*(11), 1073–1087. Retrieved from https://doi.org/10.1139/cjes-2015-0228 doi: 10.1139/cjes-2015-

0228

Torsvik, T. H., Steinberger, B., Shephard, G. E., Doubrovine, P. V., Gaina, C., Domeier, M., . . . Sager, W. W. (2019). Pacific-panthalassic reconstructions: Overview, errata and the way forward. *Geochemistry, Geophysics, Geosystems*, *20*(7), 3659–3689. Retrieved from `https://agupubs.onlinelibrary.wiley.com/doi/abs/10.1029/2019GC008402` doi: 10.1029/2019GC008402

Trønnes, R. G. (2010, Jul 01). Structure, mineralogy and dynamics of the lowermost mantle. *Mineralogy and Petrology*, *99*(3), 243–261. Retrieved from `https://doi.org/10.1007/s00710-009-0068-z` doi: 10.1007/s00710-009-0068-z

Trønnes, R. G., Baron, M., Eigenmann, K., Guren, M., Heyn, B., Løken, A., & Mohn, C. (2019). Core formation, mantle differentiation and core-mantle interaction within earth and the terrestrial planets. *Tectonophysics*, *760*, 165–198. Retrieved from `http://www.sciencedirect.com/science/article/pii/S0040195118303494` (Linking Plate Tectonics and Volcanism to Deep Earth Dynamics – a tribute to Trond H. Torsvik) doi: 10.1016/j.tecto.2018.10.021

van der Hilst, R. D., Widiyantoro, S., Creager, K. C., & Mcsweeney, T. J. (2013). Deep subduction and aspherical variations in p-wavespeed at the base of earth's mantle. In *The core-mantle boundary region* (pp. 5–20). American Geophysical Union (AGU). Retrieved from `https://agupubs.onlinelibrary.wiley.com/doi/abs/10.1029/GD028p0005` doi: 10.1029/GD028p0005

van der Hilst, R. D., & Kárason, H. (1999). Compositional heterogeneity in the bottom 1000 kilometers of earth's mantle: Toward a hybrid convection model. *Science*, *283*(5409), 1885–1888. Retrieved from `https://science.sciencemag.org/content/283/5409/1885` doi: 10.1126/science.283.5409.1885

Vidito, C., Herzberg, C., Gazel, E., Geist, D., & Harpp, K. (2013). Lithological structure of the galápagos plume. *Geochemistry, Geophysics, Geosystems*, *14*(10), 4214–4240. Retrieved from `https://agupubs.onlinelibrary.wiley.com/doi/abs/10.1002/ggge.20270` doi: 10.1002/ggge.20270

Wang, H., Wang, Y., Gurnis, M., Zahirovic, S., & Leng, W. (2018). A long-lived indian ocean slab: Deep dip reversal induced by the african llsvp. *Earth and Planetary Science Letters*, *497*, 1–11. Retrieved from `http://www.sciencedirect.com/science/article/pii/S0012821X18303339` doi: 10.1016/j.epsl.2018.05.050

Wasserburg, G. J., & DePaolo, D. J. (1979). Models of earth structure inferred from neodymium and strontium isotopic abundances. *Proceedings of the National Academy of Sciences*, *76*(8), 3594–3598. Retrieved from `https://www.pnas.org/content/76/8/3594` doi: 10.1073/pnas.76.8.3594

Weis, D., Garcia, M. O., Rhodes, J. M., Jellinek, M., & Scoates, J. S. (2011, November). Role of the deep mantle in generating the compositional asymmetry of the hawaiian mantle plume. *Nature Geoscience*, *4*, 831. Retrieved from `https://www.nature.com/articles/ngeo1328#`

supplementary-information doi: 10.1038/ngeo1328; 10.1038/n-geo1328

Williams, C. D., Li, M., McNamara, A. K., Garnero, E. J., & van Soest, M. C. (2015, November). Episodic entrainment of deep primordial mantle material into ocean island basalts. *Nature Communications*, *6*, 8937. Retrieved from https://www.nature.com/articles/ncomms9937#supplementary-information doi: 10.1038/ncomms9937; 10.1038/ncomms9937

Yoshida, M. (2008). Core-mantle boundary topography estimated from numerical simulations of instantaneous mantle flow. *Geochemistry, Geophysics, Geosystems*, *9*(7). Retrieved from https://agupubs.onlinelibrary.wiley.com/doi/abs/10.1029/2008GC002008 doi: 10.1029/2008GC002008

Zhong, S., & Liu, X. (2016). The long-wavelength mantle structure and dynamics and implications for large-scale tectonics and volcanism in the phanerozoic. *Gondwana Research*, *29*(1), 83–104. Retrieved from http://www.sciencedirect.com/science/article/pii/S1342937X15001859 doi: 10.1016/j.gr.2015.07.007

Zhong, S., Zhang, N., Li, Z.-X., & Roberts, J. H. (2007). Supercontinent cycles, true polar wander, and very long-wavelength mantle convection. *Earth and Planetary Science Letters*, *261*(3), 551–564. Retrieved from http://www.sciencedirect.com/science/article/pii/S0012821X07004761 doi: 10.1016/j.epsl.2007.07.049

Zhong, S., Zuber, M. T., Moresi, L., & Gurnis, M. (2000). Role of temperature-dependent viscosity and surface plates in spherical shell models of mantle convection. *Journal of Geophysical Research: Solid Earth*, *105*(B5), 11063–11082. Retrieved from https://agupubs.onlinelibrary.wiley.com/doi/abs/10.1029/2000JB900003 doi: 10.1029/2000JB900003

Chapter 2

Conclusions and outlook

2.1 Summary of main results

Convection has a tendency to homogenize a fluid. Consequently, a chemically distinct reservoir in Earth has to escape extensive mixing and entrainment in plumes in order to remain isolated over geological times. The ability of plumes to entrain material depends on their buoyancy flux (plume strength), but also on the properties (i.e. viscosity, density) of the thermochemical reservoir. In **Paper I**, we have shown that compositional viscosity contrasts in the lowermost mantle may be more important than previously thought:

- A high intrinsic viscosity of thermochemical piles at the core-mantle boundary reduces entrainment of the dense pile material, stabilizing piles for longer time periods.

- We identify a trade-off between the density and viscosity contrasts that are required to maintain pile stability, with viscosity contrasts being more important for smaller excess densities (Figure 2.1).

- During periods of strong deformation-induced entrainment, e.g. pile formation or a change in the structural degree of mantle convection, pile stability requires higher viscosity contrasts and/or excess densities.

Most geodynamic studies require a strongly temperature-dependent viscosity to obtain dense thermochemical piles that survive 4.5 Gyr of convection (e.g., McNamara & Zhong, 2004; Deschamps et al., 2012; Y. Li et al., 2014b). In these cases, density plays a major role in determining the stability and shape of the piles (Tackley, 2012; McNamara & Zhong, 2004; Y. Li et al., 2014b). In contrast, viscosity variations associated with a different composition of the dense piles have been shown to mainly affect the shape of piles (McNamara & Zhong, 2004, 2005; Y. Li et al., 2014b). However, this no longer holds true for significantly smaller thermal viscosity contrasts or pile excess densities, which make compositional viscosity variations more important (as summarized in Figure 2.1). In both cases, an intrinsic viscosity increase of about a factor of 10 for pile material reduces the entrainment with time signifcantly and may increase the mass remaining after 4.5 Gyr from approximately 20% of the inital amount to more than 80%. The importance of compositional viscosity variations for entrainment is further supported by fluid dynamic experiments (e.g., Davaille et al., 2002). In case of increased internal heating within dense piles, the viscosity may play an even more complex role in determining the stability of LLSVPs (Y. Li et al., 2019).
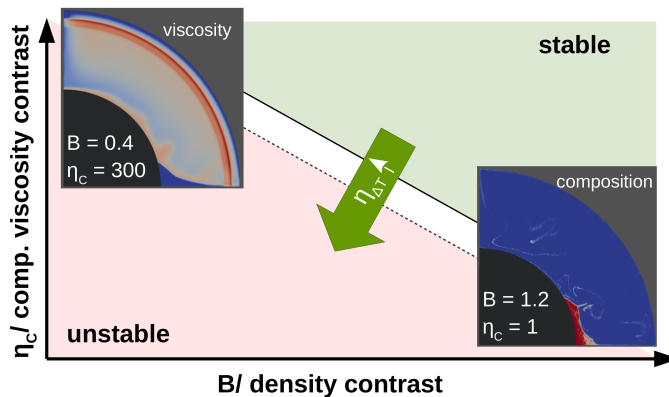
Figure 2.1: Summary of the results of Paper I. For small pile excess densities B, a compositional viscosity contrast η_C becomes more important (upper left corner), while a large excess density stabilises piles for any viscosity structure (lower right corner). An increasing temperature-dependence of viscosity $\eta_{\Delta T}$ moves the transition between stable and unstable piles towards smaller density and viscosity contrasts (green arrow).

As for the entrainment of dense material in plumes, the overall viscosity and density structure of the lowermost mantle also play a dominant role for the initiation of plumes. However, since plumes form from the thermal boundary layer outside the thermochemical piles, pile properties (i.e. their density and viscosity) are less important than the thermal viscosity contrast, which is predominantly affecting the viscosity of the ambient mantle. As has been shown by M. Li et al. (2018), plumes and dense piles may interact with each other, with piles being uplifted by the drag of rising plumes. In **Paper II**, we describe a new mechanism of plume generation associated with lateral motion of the pile margins, which causes "early" plume initiation at the pile margin before a plume would naturally form via conductive growth of the TBL (Deschamps & Tackley, 2008; M. Li & Zhong, 2017):

- A plume rising at the margins of thermochemical piles locally increases the pile thickness, thereby reducing the area of CMB that is covered by the dense pile (Figure 2.2A).

- When the plume root becomes weaker and/or moves towards the pile centre due to lateral mantle flow, the thickened pile edge collapses under the influence of gravity (Figure 2.2B-C).

- The collapsing pile spreads along the core-mantle boundary and increases the thickness of the thermal boundary layer (TBL) next to the pile margin, triggering a new plume (Figure 2.2C).

- The period of plume initiation is controlled by the velocity of lateral mantle flow along the core-mantle boundary.
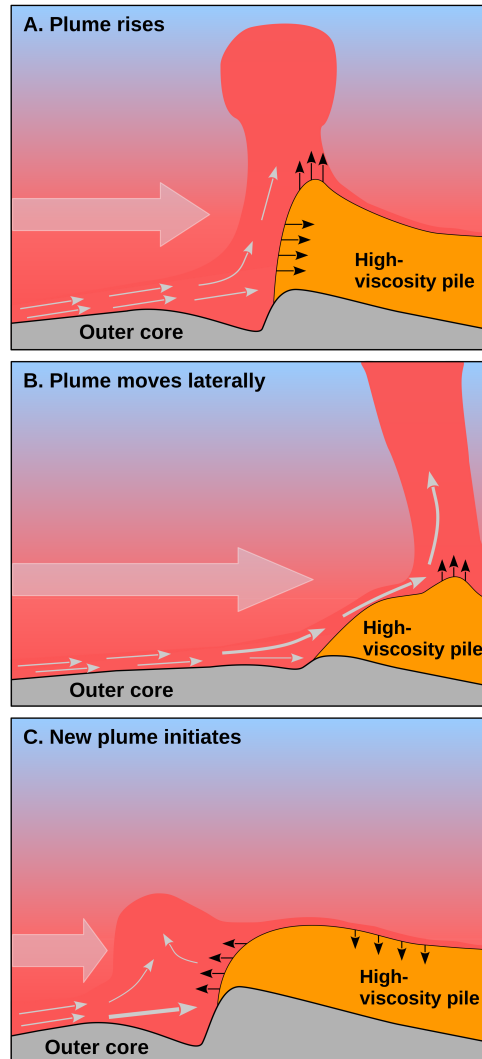
Figure 2.2: Schematic summary of the results shown in Paper II and Paper III. Plumes are formed periodically at the pile margin due to the interaction of piles and rising plumes, which is associated with vertical and lateral motion of the pile boundaries (indicated by black arrows). The large-scale mantle flow (thick arrow) pushes the plume slowly towards the pile centre, moving the position of maximum pile thickness with the plume root. A part of the lateral flow in the thermal boundary layer (shown as grey arrows) is dragged into the plume, but the lowermost part of the flow will be trapped in a wedge of hot material that is compressed against the pile if the pile has a high intrinsic viscosity. The amount of material in the compressed TBL wedge (indicated by the thickness of the grey arrows) depends on the lateral motion of the pile margin and its steepness, both of which reflect the stage within the plume cycle.

For an approximately constant lateral TBL flow, i.e. a stable convective pattern with ongoing subduction of the same plate velocity, this mechanism of interaction between plumes and piles results in an almost periodic plume initiation. The plume period is then determined by the slab sinking rate, i.e. the temperature-dependence of viscosity, and the plate velocity. The pile density and viscosity have minor effects on the observed plume period, but they determine the lateral and vertical motion of the pile margin during the plume cycle. A periodic change in subduction velocity, e.g. as may be expected for supercontinent cycles, can excite plume initiation at pile margins with the same period as the plate velocity. Moreover, a change in subduction configuration, i.e. an advancing and retreating subduction zone associated with supercontinent breakup (Matthews et al., 2016), may also trigger a local pile edge collapse and cause a larger number of plumes in close spatial and temporal proximity, as has been observed between 95 and 155 Ma at the southeastern corner of the African LLSVP (Torsvik et al., 2016; Torsvik, 2019).

Both the density and viscosity structure of the lowermost mantle and the plume cycle further affect how the CMB deforms due to isostatic and dynamic stresses. Dense piles or sinking flow associated with slabs cause depressions in the CMB, while rising flow in plumes elevates the CMB (Lassak et al., 2007, 2010; Deschamps et al., 2017; Deschamps & Li, 2019). This long-wavelength topography can be used as an indicator for pile density, since a pile requires an excess density of about 1.8-2.0% to form a noticable depression, otherwise the effect of thermal expansion is dominant and the CMB is uplifted (Lassak et al., 2007; Yoshida, 2008; Lassak et al., 2010; Deschamps et al., 2017; Deschamps & Li, 2019). A lateral viscosity contrast between dense piles and the ambient mantle does not modify this pattern, yet we discovered a characteristic short-scale topography at the pile margin (Figure 2.2) as shown in **Paper III**:

- A pile with high intrinsic viscosity causes an approximately 80-120 km wide depression around the pile margins, allowing for the discrimination between piles with and without increased intrinsic viscosity.

- The depression is caused by a wedge of TBL material that becomes compressed agains the pile, combined with an uplift of the CMB beneath the pile margin relative to its surroundings (Figure 2.2).

- The depth and symmetry of the depression constrain the viscosity contrast between the ambient mantle and the dense pile, while neither the background viscosity structure nor the pile density affect the shape or size of the depression.

- The topography is most pronounced and asymmetric at the base of initiating plumes, potentially allowing for the identification of active plume generation zones in Earth (Figure 2.2C).

The presence of a (dense) pile at the CMB forces lateral flow to change its direction at the pile margins. However, a pile with high viscosity does not accomodate large lateral velocity gradients, but focuses them in a wedge of TBL material just outside the pile. The compression of this material wegde, in combination with a relative uplift of the pile margin, causes the characteristic depression around the margins of high-viscosity piles. Relative uplift of the CMB beneath the pile is caused by the high pile viscosity, which increases the coupling between the mantle and the CMB, and thus topography amplitudes (Deschamps et al., 2017; Deschamps & Li, 2019)). Consequently, seismic observations of this topographic structure around the LLSVP margins would give constraints on the nature of the LLSVPs (thermal vs. thermochemical), the magnitude of a potential viscosity contrast between ambient mantle and pile, and at which stage in the plume cycle the respective part of the LLSVP edge may be. Core-reflected waves (e.g., Wu et al., 2014; Schlaphorst et al., 2015; Shen et al., 2016) or the correlation of seismic noise (Mancinelli & Shearer, 2016) may provide the required resolution to detect our predicted topography.

Based on the geochemistry of the lower mantle, and associated phase equilibria and phase transitions, viscosity and/or density contrasts in the lower mantle between (dense) piles and the ambient mantle are likely to occur, independent of whether the LLSVPs are composed of bridgmanitic cumulates or basaltic material (Hirose et al., 2005; Ballmer et al., 2016; Trønnes et al., 2019). Although these contrasts are difficult to measure directly, they have a strong effect on lower mantle dynamics. The density of piles determines the thickness and topography of the thermochemical structures, their stability with respect to entrainment and the long-wavelength CMB topography beneath the piles (e.g., McNamara & Zhong, 2004; Lassak et al., 2010; Tackley, 2012; Deschamps et al., 2017). With a higher intrinsic viscosity than the ambient mantle due to compositional viscosity contrasts, piles may have a better chance to survive vigorous mantle convection, show reduced mobility of pile edges during plume initiation (although this does not affect the mechanism of plume generation), and cause a characteristic short-scale CMB topography surrounding them that could be used to constrain the nature of LLSVPs. Thermal viscosity contrasts predominantly affect the period of plume initiation at the pile margins, which relates to the entrainment and stability of dense piles, and modify amplitudes of CMB the long-wavelength topography.

Thus, using the stability of the dense material, its interaction with plumes (plume period and plume source locations) and the observed core-mantle boundary topography (existence of short-scale topography and its magnitude), we may be able to get constraints on relative (and absolute?) viscosities and pile densities. Moreover, we may finally be able to answer the question about whether LLSVPs are thermal (e.g., Davies et al., 2012; Schuberth et al., 2012) or thermochemical structures (e.g., McNamara & Zhong, 2004; Deschamps et al., 2012; M. Li & McNamara, 2013; Y. Li et al., 2014b). Although each of these

predictions has its trade-offs between different parameters, a combination of such predictions and respective observations may be able to resolve the structure of the lowermost mantle and the origin of the LLSVPs.

2.2 Model assumptions and limitations

The models presented in Papers I to III have several underlying assumptions and limitations. Some of them are specific for the problem considered, as discussed in the respective sections in the papers, but others are common to all results shown in this thesis. In the following, I will discuss the most important of these common limitations.

The most obvious simplification is the geometry that we use, which is a quarter of a 2-D spherical annulus instead of a 3-D spherical shell. This geometry allows for the evaluation of a broader parameter range at reduced computational costs. Moreover, is has been shown that the spherical annulus geometry can capture mantle dynamics reasonably well as long as the problem is not strongly dependent on 3-D effects (Hernlund & Tackley, 2008). However, our models cannot capture the lateral flow as it would occur within Earth, which may have an effect on the location of plume initiation and lateral motion of plumes (M. Li & Zhong, 2017, 2019, see also discussion in Paper II). With respect to our results, we do not expect any significant modifications of the plume formation mechanism, except for a less pronounced periodicity. The estimated effect of a 3-D geometry on entrainment of pile material and CMB topography are even smaller, as discussed in the respective papers. Global models with the resolution as required in the work presented here (between 1 and 17 km) require a lot of computation time and are not feasible for exploring the range of densities and viscosities shown in this work.

In addition to being 2-D, our model domain only comprises a quarter of a spherical annulus. This introduces two additional boundaries, both of which are set to free-slip. Although these boundaries force the flow into radial direction (subduction at the surface and upwelling at the CMB above the dense pile), we do not expect this to have a significant impact on our results. First of all, the interaction between slabs, plumes and dense piles, which is our interest, takes place approximately in the centre of the domain and is thus not impacted by boundary effects. Both entrainment by plumes, plume initiation, and CMB topography are localized around the pile margin, which is far enough from side boundaries to be unaffected by them. However, a 3-D spherical shell geometry may tend to increase pile stability (while reducing the persistence of the degree-2 structure), because our 2-D models overestimate the number of plumes forming at each section of the LLSVP margin. On the other hand, plumes might be stronger in 3-D since they contain more thermal boundary layer material, which would increase the rate of entrainment per plume. A full spherical annulus with two symmetric subduction zones and two piles would result in a similar configuration as in our models with reflective boundaries, in which the other

parts of the domain can be imagined by mirroring at the side boundaries. Yet, the smaller domain has a significant advantage with respect to computational costs.

Apart from the geometry itself, we use a strong simplification of subduction processes by imposing a surface velocity to force subduction. In our models, we do this to reproduce the observed degree-2 structure of the lowermost mantle (e.g., Dziewonski et al., 2010; Cottaar & Lekic, 2016). If we do not impose plate velocities, our model setup would not create subduction zones with sinking slabs, but would instead form lithospheric drips that sink through the mantle, i.e. a different type of convection regime. In order to get self-consistent subduction, we would have to include weakening mechanisms for plates, e.g. yielding, which makes the viscosity law more complicated (e.g. Y. Li et al., 2015; Deschamps et al., 2017). Moreover, we could no longer control the structural degree of the lower mantle or the subduction velocity, which play significant roles in the underlying dynamics of interaction between slabs, plumes and dense piles. Where relevant, we investigated the effect of the degree of lower mantle structure and the plate velocity (Paper I and Paper II).

Finally, we simplify the set of equations solved numerically by using the Boussinesq approximation, i.e. the assumption of incompressible flow (see Section 1.3.1). Although this simplification is not strictly necessary since both codes used in this study can solve compressible flow, it makes the calculations much faster (Bangerth et al., 2019). Moreover, the effect of compressibility is small for large-scale convection problems such as entrainment or plume initiation, as can be seen when comparing studies using compressible (e.g., Y. Li et al., 2014b, 2014a, 2015, 2019) and incompressible flow (e.g., McNamara & Zhong, 2004, 2005; M. Li & McNamara, 2013; Mulyukova et al., 2015; M. Li et al., 2018; Heyn et al., 2018). The same holds true for models that predict core-mantle boundary topography, which agree well between compressible (Deschamps et al., 2017; Deschamps & Li, 2019) and incompressible flow (Lassak et al., 2007, 2010, and Paper III). Yet, differences between compressible and incompressible flow calculations have to be taken into account when converting parameters between different studies.

2.3 Future directions

In order to use the predicted short-scale topography to discriminate between thermal and (viscous) thermochemical LLSVPs, we require observations or comfirmed lack of observations of the characteristic depression. Hence, a first step would be to input our predicted CMB topography into a seismic wave propagation program and calculate synthetic seismograms to see how this changes the wave field. This would inform us about whether the structure can be detected or not, and which methods and waves may be used to look for this type of topography within the Earth. Based on recent studies, core reflected waves such as PcP/ ScP (Wu et al., 2014; Gassner et al., 2015; Shen et al.,

2016) or P4KP (Schlaphorst et al., 2015) may be viable choices. Focusing and defocusing effects of CMB topography on seismic energy, and thus amplitudes, may provide a resolution that is high enough to detect the predicted structure (Wu et al., 2014; Shen et al., 2016). As soon as we know whether we can reliably detect topography of the predicted wavelength and amplitude, seismic studies investigating the CMB around the LLSVP margins may provide the answer to the question about the nature of LLSVPs. Moreover, it might give us insight into where plumes are currently initiated or started to rise through the mantle, enabling us to predict when and where plume heads may reach the surface.

With respect to modeling, it may be advisable to repeat the CMB topography study with either a "sticky core", comparable to a "sticky air" layer (Crameri et al., 2012), or a freely deformable CMB as "free base", analogous to the free surface of Crameri et al. (2012). For subduction processes, it has been shown that the choice of stress-derived topography may give inaccurate results, especially for short wavelength topography, which are absent for the "sticky air" or "free surface" approaches (Crameri et al., 2012, 2017). However, the focus for CMB topography has up to now been on long wavelengths (e.g., Lassak et al., 2010; Deschamps et al., 2017; Deschamps & Li, 2019), and no study so far has applied a similar method for the base of the mantle. Yet, since our predicted topography in Paper III is only about 120 km wide, it might be useful to apply one of the methods above. Preliminary tests with models as described in Paper III, but featuring a "free base", indicate that the topographic pattern does not change.

Since our models are in 2-D, a natural extension would be to repeat the simulations in 3-D spherical geometry, especially for the plume cycle (Paper II) and the CMB topography (Paper III). In these cases, we would either have to impose plate velocities as obtained from plate reconstructions for the last few hundred Myr (Matthews et al., 2016), as done e.g. in M. Li and Zhong (2017), or enable self-consistent generation of subduction zones (e.g. Deschamps et al., 2017). Furthermore, a more realistic viscosity structure of the upper mantle, including phase transitions, would add another component of dynamic behavior, for example slab stagnation within the transition zone and slab avalanches into the lower mantle. However, a phase change of bridgmanite to post-bridgmanite in the lower mantle, including its associated viscosity drop (Ammann et al., 2010), is expected to be more important for lower mantle dynamics (e.g., Y. Li et al., 2014a, 2015; Deschamps & Li, 2019). In addition, an uneven distribution of internal heating rate due to fractionation of radioactive elements may have a stronger effect than previously thought (Y. Li et al., 2019), and could be implemented in our models.

Finally, there may be other chemical heterogeneities in the lower mantle. One of them are the ultra-low velocity zones (ULVZs), observed predominantly at the base of plumes, which may represent dense partial melt or very iron-rich material (see e.g., review by McNamara, 2019). Depending on their density and

viscosity, ULVZs can impact the shape and size of the characteristic short-scale depression around the pile margins. On the other hand, a circum-pile depression may help to focus and trap ULVZs at the roots of plumes along the LLSVP margins. Another reservoir of (primordial) bridgmanitic material within the mantle might present in form of the so-called Bridgmanite Enriched Ancient Mantle Structures (BEAMS, Ballmer et al. (2017)). In contrast to piles of dense cumulates, these structures are neutrally buoyant in the upper part of the lower mantle, and would be floating at mid-mantle depths. Due to their high viscosity (Ballmer et al., 2017; Trønnes et al., 2019), BEAMS may exort a key control on the convective planfrom by preventing slabs and plumes from penetrating through them, focusing up- and downwellings into specific areas instead. As such, BEAMS may stabilize a degree-2 convection system, or potentially even enforce it in the first place. Consequently, the interaction between BEAMS, slabs, piles and plumes will be an important topic for future investigation.
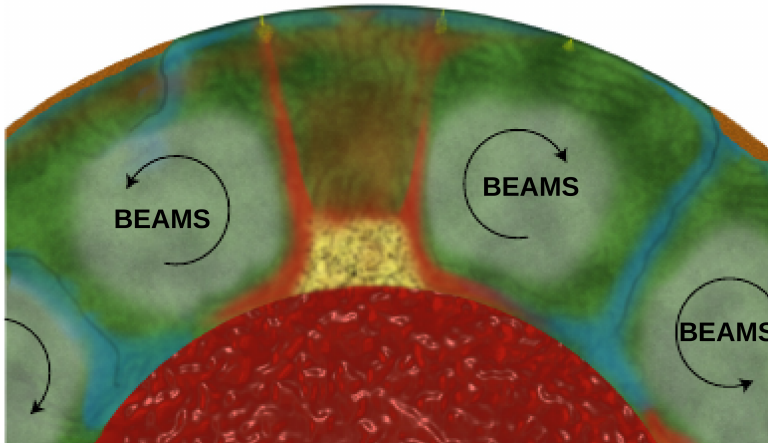

Figure 2.3: Conceptual model of BEAMS that control mantle circulation patterns, after Ballmer et al. (2017). BEAMS are expected to form in the middle of the mantle, in between the belt of subduction and the positions of LLSVPs. Due to their high viscosity, these structures may prevent subducted slabs from sinking into the lower mantle close to LLSVPs, and thus focus up- and downwellings in the lower mantle into a long-wavelength structure.

References

Ammann, M. W., Brodholt, J. P., Wookey, J., & Dobson, D. P. (2010, May). First-principles constraints on diffusion in lower-mantle minerals and a weak d layer. *Nature*, *465*, 462–465. Retrieved from `https://www.nature.com/articles/nature09052#supplementary-information`   doi: 10.1038/nature09052; 10.1038/nature09052

Ballmer, M. D., Houser, C., Hernlund, J. W., Wentzcovitch, R. M., & Hirose, K. (2017, February). Persistence of strong silica-enriched domains in the earth's lower mantle. *Nature Geoscience*, *10*, 236. Retrieved from `https://www.nature.com/articles/ngeo2898#supplementary-information` doi: 10.1038/ngeo2898; 10.1038/ngeo2898

Ballmer, M. D., Schumacher, L., Lekic, V., Thomas, C., & Ito, G. (2016). Compositional layering within the large low shear-wave velocity provinces in the lower mantle. *Geochemistry, Geophysics, Geosystems*, *17*(12), 5056–5077. Retrieved from `https://agupubs.onlinelibrary.wiley.com/doi/abs/10.1002/2016GC006605` doi: 10.1002/2016GC006605

Bangerth, W., Dannberg, J., Gassmöller, R., Heister, T., et al. (2019, April). ASPECT: Advanced solver for problems in earth's convection, user manual. Retrieved from `https://doi.org/10.6084/m9.figshare.4865333` (doi:10.6084/m9.figshare.4865333) doi: 10.6084/m9.figshare.4865333

Cottaar, S., & Lekic, V. (2016, 08). Morphology of seismically slow lower-mantle structures. *Geophysical Journal International*, *207*(2), 1122–1136. Retrieved from `https://doi.org/10.1093/gji/ggw324` doi: 10.1093/gji/ggw324

Crameri, F., Lithgow-Bertelloni, C., & Tackley, P. (2017). The dynamical control of subduction parameters on surface topography. *Geochemistry, Geophysics, Geosystems*, *18*(4), 1661–1687. Retrieved from `https://agupubs.onlinelibrary.wiley.com/doi/abs/10.1002/2017GC006821` doi: 10.1002/2017GC006821

Crameri, F., Schmeling, H., Golabek, G. J., Duretz, T., Orendt, R., Buiter, S. J. H., . . . Tackley, P. J. (2012, 04). A comparison of numerical surface topography calculations in geodynamic modelling: an evaluation of the 'sticky air' method. *Geophysical Journal International*, *189*(1), 38–54. Retrieved from `https://doi.org/10.1111/j.1365-246X.2012.05388.x` doi: 10.1111/j.1365-246X.2012.05388.x

Davaille, A., Girard, F., & Bars, M. L. (2002). How to anchor hotspots in a convecting mantle? *Earth and Planetary Science Letters*, *203*(2), 621–634. Retrieved from `http://www.sciencedirect.com/science/article/pii/S0012821X0200897X` doi: 10.1016/S0012-821X(02)00897-X

Davies, D. R., Goes, S., Davies, J., Schuberth, B., Bunge, H.-P., & Ritsema, J. (2012). Reconciling dynamic and seismic models of earth's lower mantle: The dominant role of thermal heterogeneity. *Earth and Planetary Science Letters*, *353-354*, 253–269. Retrieved from `http://www.sciencedirect.com/science/article/pii/S0012821X1200444X` doi: 10.1016/j.epsl.2012.08.016

Deschamps, F., Cobden, L., & Tackley, P. J. (2012). The primitive nature of large low shear-wave velocity provinces. *Earth and Planetary Science Letters*, *349-350*, 198–208. Retrieved from `http://www.sciencedirect.com/science/article/pii/S0012821X12003718` doi: 10.1016/j.epsl.2012.07.012

Deschamps, F., & Li, Y. (2019). Core-mantle boundary dynamic topography:

Influence of postperovskite viscosity. *Journal of Geophysical Research: Solid Earth*, *124*(8), 9247–9264. Retrieved from `https://agupubs.onlinelibrary.wiley.com/doi/abs/10.1029/2019JB017859` doi: 10.1029/2019JB017859

Deschamps, F., Rogister, Y., & Tackley, P. J. (2017, 09). Constraints on core–mantle boundary topography from models of thermal and thermochemical convection. *Geophysical Journal International*, *212*(1), 164–188. Retrieved from `https://doi.org/10.1093/gji/ggx402` doi: 10.1093/gji/ggx402

Deschamps, F., & Tackley, P. J. (2008). Searching for models of thermochemical convection that explain probabilistic tomography: I. principles and influence of rheological parameters. *Physics of the Earth and Planetary Interiors*, *171*(1), 357–373. Retrieved from `http://www.sciencedirect.com/science/article/pii/S0031920108000824` (Recent Advances in Computational Geodynamics: Theory, Numerics and Applications) doi: 10.1016/j.pepi.2008.04.016

Dziewonski, A. M., Lekic, V., & Romanowicz, B. A. (2010). Mantle anchor structure: An argument for bottom up tectonics. *Earth and Planetary Science Letters*, *299*(1), 69–79. Retrieved from `http://www.sciencedirect.com/science/article/pii/S0012821X10005236` doi: 10.1016/j.epsl.2010.08.013

Gassner, A., Thomas, C., Krüger, F., & Weber, M. (2015). Probing the core–mantle boundary beneath europe and western eurasia: A detailed study using pcp. *Physics of the Earth and Planetary Interiors*, *246*, 9–24. Retrieved from `http://www.sciencedirect.com/science/article/pii/S0031920115000965` doi: 10.1016/j.pepi.2015.06.007

Hernlund, J. W., & Tackley, P. J. (2008). Modeling mantle convection in the spherical annulus. *Physics of the Earth and Planetary Interiors*, *171*(1), 48–54. Retrieved from `http://www.sciencedirect.com/science/article/pii/S0031920108001921` (Recent Advances in Computational Geodynamics: Theory, Numerics and Applications) doi: 10.1016/j.pepi.2008.07.037

Heyn, B. H., Conrad, C. P., & Trønnes, R. G. (2018). Stabilizing effect of compositional viscosity contrasts on thermochemical piles. *Geophysical Research Letters*, *45*(15), 7523–7532. Retrieved from `https://agupubs.onlinelibrary.wiley.com/doi/abs/10.1029/2018GL078799` doi: 10.1029/2018GL078799

Hirose, K., Takafuji, N., Sata, N., & Ohishi, Y. (2005). Phase transition and density of subducted morb crust in the lower mantle. *Earth and Planetary Science Letters*, *237*(1), 239–251. Retrieved from `http://www.sciencedirect.com/science/article/pii/S0012821X0500419X` doi: 10.1016/j.epsl.2005.06.035

Lassak, T. M., McNamara, A. K., Garnero, E. J., & Zhong, S. (2010). Core–mantle boundary topography as a possible constraint on lower mantle chemistry and dynamics. *Earth and Planetary Science Letters*, *289*(1), 232–241. Retrieved from `http://www.sciencedirect.com/science/`

`article/pii/S0012821X09006591` doi: 10.1016/j.epsl.2009.11.012

Lassak, T. M., McNamara, A. K., & Zhong, S. (2007). Influence of thermochemical piles on topography at earth's core–mantle boundary. *Earth and Planetary Science Letters*, *261*(3), 443–455. Retrieved from `http://www.sciencedirect.com/science/article/pii/S0012821X07004499` doi: 10.1016/j.epsl.2007.07.015

Li, M., & McNamara, A. K. (2013). The difficulty for subducted oceanic crust to accumulate at the earth's core-mantle boundary. *Journal of Geophysical Research: Solid Earth*, *118*(4), 1807–1816. Retrieved from `https://agupubs.onlinelibrary.wiley.com/doi/abs/10.1002/jgrb.50156` doi: 10.1002/jgrb.50156

Li, M., & Zhong, S. (2017). The source location of mantle plumes from 3d spherical models of mantle convection. *Earth and Planetary Science Letters*, *478*, 47–57. Retrieved from `http://www.sciencedirect.com/science/article/pii/S0012821X17304806` doi: 10.1016/j.epsl.2017.08.033

Li, M., & Zhong, S. (2019). Lateral motion of mantle plumes in 3-d geodynamic models. *Geophysical Research Letters*, *46*(9), 4685–4693. Retrieved from `https://agupubs.onlinelibrary.wiley.com/doi/abs/10.1029/2018GL081404` doi: 10.1029/2018GL081404

Li, M., Zhong, S., & Olson, P. (2018). Linking lowermost mantle structure, core-mantle boundary heat flux and mantle plume formation. *Physics of the Earth and Planetary Interiors*, *277*, 10–29. Retrieved from `http://www.sciencedirect.com/science/article/pii/S0031920117302625` doi: 10.1016/j.pepi.2018.01.010

Li, Y., Deschamps, F., & Tackley, P. J. (2014a). Effects of low-viscosity post-perovskite on the stability and structure of primordial reservoirs in the lower mantle. *Geophysical Research Letters*, *41*(20), 7089–7097. Retrieved from `https://agupubs.onlinelibrary.wiley.com/doi/abs/10.1002/2014GL061362` doi: 10.1002/2014GL061362

Li, Y., Deschamps, F., & Tackley, P. J. (2014b, 09). The stability and structure of primordial reservoirs in the lower mantle: insights from models of thermochemical convection in three-dimensional spherical geometry. *Geophysical Journal International*, *199*(2), 914–930. Retrieved from `https://doi.org/10.1093/gji/ggu295` doi: 10.1093/gji/ggu295

Li, Y., Deschamps, F., & Tackley, P. J. (2015). Effects of the post-perovskite phase transition properties on the stability and structure of primordial reservoirs in the lower mantle of the earth. *Earth and Planetary Science Letters*, *432*, 1–12. Retrieved from `http://www.sciencedirect.com/science/article/pii/S0012821X15006159` doi: 10.1016/j.epsl.2015.09.040

Li, Y., Deschamps, F., Yang, J., Chen, L., Zhao, L., & Tackley, P. J. (2019). Effects of the compositional viscosity ratio on the long-term evolution of thermochemical reservoirs in the deep mantle. *Geophysical Research Letters*, *46*(16), 9591–9601. Retrieved from `https://agupubs.onlinelibrary.wiley.com/doi/abs/10.1029/2019GL083668` doi: 10.1029/2019GL083668

Mancinelli, N., & Shearer, P. (2016). Scattered energy from a rough core-

mantle boundary modeled by a monte carlo seismic particle method: Application to pkkp precursors. *Geophysical Research Letters*, *43*(15), 7963–7972. Retrieved from `https://agupubs.onlinelibrary.wiley.com/doi/abs/10.1002/2016GL070286` doi: 10.1002/2016GL070286

Matthews, K. J., Maloney, K. T., Zahirovic, S., Williams, S. E., Seton, M., & Müller, R. D. (2016). Global plate boundary evolution and kinematics since the late paleozoic. *Global and Planetary Change*, *146*, 226–250. Retrieved from `http://www.sciencedirect.com/science/article/pii/S0921818116302417` doi: 10.1016/j.gloplacha.2016.10.002

McNamara, A. K. (2019). A review of large low shear velocity provinces and ultra low velocity zones. *Tectonophysics*, *760*, 199–220. Retrieved from `http://www.sciencedirect.com/science/article/pii/S0040195118301586` (Linking Plate Tectonics and Volcanism to Deep Earth Dynamics – a tribute to Trond H. Torsvik) doi: 10.1016/j.tecto.2018.04.015

McNamara, A. K., & Zhong, S. (2004). Thermochemical structures within a spherical mantle: Superplumes or piles? *Journal of Geophysical Research: Solid Earth*, *109*(B7). Retrieved from `https://agupubs.onlinelibrary.wiley.com/doi/abs/10.1029/2003JB002847` doi: 10.1029/2003JB002847

McNamara, A. K., & Zhong, S. (2005). Thermochemical structures beneath africa and the pacific ocean. *Nature*, *437*(7062), 1136–1139. doi: 10.1038/nature04066; 10.1038/nature04066

Mulyukova, E., Steinberger, B., Dabrowski, M., & Sobolev, S. V. (2015). Survival of llsvps for billions of years in a vigorously convecting mantle: Replenishment and destruction of chemical anomaly. *Journal of Geophysical Research: Solid Earth*, *120*(5), 3824–3847. Retrieved from `https://agupubs.onlinelibrary.wiley.com/doi/abs/10.1002/2014JB011688` doi: 10.1002/2014JB011688

Schlaphorst, D., Thomas, C., Holme, R., & Abreu, R. (2015, 12). Investigation of core–mantle boundary topography and lowermost mantle with p4kp waves. *Geophysical Journal International*, *204*(2), 1060–1071. Retrieved from `https://doi.org/10.1093/gji/ggv496` doi: 10.1093/gji/ggv496

Schuberth, B. S. A., Zaroli, C., & Nolet, G. (2012, 03). Synthetic seismograms for a synthetic earth: long-period p- and s-wave traveltime variations can be explained by temperature alone. *Geophysical Journal International*, *188*(3), 1393–1412. Retrieved from `https://doi.org/10.1111/j.1365-246X.2011.05333.x` doi: 10.1111/j.1365-246X.2011.05333.x

Shen, Z., Ni, S., Wu, W., & Sun, D. (2016). Short period scp phase amplitude calculations for core–mantle boundary with intermediate scale topography. *Physics of the Earth and Planetary Interiors*, *253*, 64–73. Retrieved from `http://www.sciencedirect.com/science/article/pii/S0031920116000200` doi: 10.1016/j.pepi.2016.02.002

Tackley, P. J. (2012). Dynamics and evolution of the deep mantle resulting from thermal, chemical, phase and melting effects. *Earth-Science Reviews*, *110*(1), 1–25. Retrieved from `http://`

www.sciencedirect.com/science/article/pii/S0012825211001486
doi: 10.1016/j.earscirev.2011.10.001

Torsvik, T. H. (2019). Earth history: A journey in time and space from base to top. *Tectonophysics*, *760*, 297–313. Retrieved from http://www.sciencedirect.com/science/article/pii/S0040195118303147 (Linking Plate Tectonics and Volcanism to Deep Earth Dynamics – a tribute to Trond H. Torsvik) doi: 10.1016/j.tecto.2018.09.009

Torsvik, T. H., Steinberger, B., Ashwal, L. D., Doubrovine, P. V., & Trønnes, R. G. (2016). Earth evolution and dynamics—a tribute to kevin burke. *Canadian Journal of Earth Sciences*, *53*(11), 1073–1087. Retrieved from https://doi.org/10.1139/cjes-2015-0228 doi: 10.1139/cjes-2015-0228

Trønnes, R. G., Baron, M., Eigenmann, K., Guren, M., Heyn, B., Løken, A., & Mohn, C. (2019). Core formation, mantle differentiation and core-mantle interaction within earth and the terrestrial planets. *Tectonophysics*, *760*, 165–198. Retrieved from http://www.sciencedirect.com/science/article/pii/S0040195118303494 (Linking Plate Tectonics and Volcanism to Deep Earth Dynamics – a tribute to Trond H. Torsvik) doi: 10.1016/j.tecto.2018.10.021

Wu, W., Ni, S., & Shen, Z. (2014). Constraining the short scale core–mantle boundary topography beneath kenai peninsula (alaska) with amplitudes of core-reflected pcp wave. *Physics of the Earth and Planetary Interiors*, *236*, 60–68. Retrieved from http://www.sciencedirect.com/science/article/pii/S0031920114002003 doi: 10.1016/j.pepi.2014.09.001

Yoshida, M. (2008). Core-mantle boundary topography estimated from numerical simulations of instantaneous mantle flow. *Geochemistry, Geophysics, Geosystems*, *9*(7). Retrieved from https://agupubs.onlinelibrary.wiley.com/doi/abs/10.1029/2008GC002008 doi: 10.1029/2008GC002008

Papers

Paper I

Stabilizing Effect of Compositional Viscosity Contrasts on Thermochemical Piles

I

Björn H. Heyn, Clinton P. Conrad, Reidar G. Trønnes

Abstract

The large low shear velocity provinces (LLSVPs) observed in the lowermost mantle are widely accepted as chemically distinct thermochemical "piles", but their origin and long-term evolution remain poorly understood. The survival time and shape of the LLSVPs are thought to be mainly controlled by their compositional density, while their viscosity has beeen considered less important. Based on recent constraints on chemical reactions between mantle and core, a more complex viscosity structure of the lowermost mantle, possibly including high viscosity thermochemical pile material, seems reasonable. In this study, we use numerical models to identify a trade-off between compositional viscosity and density contrasts required for long-term stability of thermochemical piles, which permits lower-density and higher-viscosity piles. Moreover, our results indicate more restrictive stability conditions during periods of strong deformation-induced entrainment, e.g. during initial pile formation, which suggests long-term pile survival.

I.1 Introduction

The presence of a dominant degree-2 structure of low seismic velocities in the lowermost mantle has been revealed by seismic tomography models throughout the last decades, (e.g., Hager et al., 1985; Dziewonski et al., 2010; Garnero et al., 2016). Although all tomographic models agree on the position of the so-called large low shear velocity provinces (LLSVPs) (Garnero & McNamara, 2008; Dziewonski et al., 2010; Garnero et al., 2016) beneath Africa and the Pacific (Garnero & McNamara, 2008; Lekic et al., 2012; Cottaar & Lekic, 2016), their origin and evolution with time is still under debate. While some studies suggest a purely thermal origin of the observed structures (e.g., Schuberth, Bunge,

Steinle-Neumann, et al., 2009; Schuberth, Bunge, & Ritsema, 2009; Schuberth et al., 2012; Davies et al., 2012) or indicate a dominant effect of temperature (Simmons et al., 2009), most geodynamic models involve a compositionally distinct and dense pile material (e.g., McNamara & Zhong, 2004, 2005; Nakagawa & Tackley, 2011; Tackley, 2012; Y. Li et al., 2014, 2015; Mulyukova et al., 2015). Typical arguments supporting chemical piles include their sharp boundaries (see review by Garnero et al., 2016), although they might also be explained by strong temperature gradients (Schuberth, Bunge, Steinle-Neumann, et al., 2009; Schuberth et al., 2012; Davies et al., 2012).

Two different possible candidate materials for chemical LLSVPs, recycled oceanic crust (MORB) (Nakagawa & Tackley, 2011; M. Li & McNamara, 2013; M. Li et al., 2014; Mulyukova et al., 2015), or primordial iron-rich cumulates (McNamara & Zhong, 2004, 2005; Nakagawa & Tackley, 2011; Y. Li et al., 2014, 2015), imply different pile formation histories. While MORB would accumulate over time to form the observed structures (M. Li & McNamara, 2013; Mulyukova et al., 2015), primordial material would start as a layer at the core-mantle boundary (CMB) after crystallization of the magma ocean (Labrosse et al., 2007) and subsequently be deformed by mantle convection to form two antipodal piles (e.g., McNamara & Zhong, 2004; Y. Li et al., 2014, 2015). In both cases, composition may affect the viscosity, which considerably widens the range of possible viscosities in the pile (Torsvik et al., 2016).

Apart from the composition of the piles, their evolution is still under debate. Stability of piles can refer to the evolution of their spatial distribution within the mantle or their survival time. Since we observe these structures 4.5 Gyrs after Earth's formation, temporal stability (survival) has to be fulfilled. However, constraints for spatial stability are not as obvious. For at least the last 300 Myrs, stability of the current degree-2 structure of LLSVPs has been inferred by Torsvik et al. (2010, 2014, 2016) based on reconstructions of large igneous provinces and kimberlites, which are both related to plumes rising at the LLSVP margins. Additionally, Conrad et al. (2013) showed persistent tectonic divergence above the two LLSVPs for at least the last 250 Myrs, suggesting stable upwellings there. Here we consider the conditions necessary to maintain temporal stability of the piles under the simplifying assumption of spatial stability of mantle flow and surface tectonics, which gives us the minimum requirements of pile survival.

Survival of thermochemical piles at the CMB is thought to be mostly controlled by the chemical density contrast between the pile and the surrounding mantle (e.g., Tackley, 2012). Y. Li et al. (2014) showed that large temperature-induced viscosity contrasts (factor of 10^6) help to stabilize piles, while comparably small compositional viscosity contrasts (≤ 100 times) are less important for strongly temperature-controlled viscosity profiles. However, a higher intrinsic pile viscosity may be required for material with high bulk modulus (Bower et al., 2013). Laboratory experiments of Davaille et al. (2002) also indicate the importance of higher viscosity to reduce entrainment of the dense component.

Reactions between the core and a thermally insulated and long-lived basal magma ocean (BMO) (Labrosse et al., 2007) may provide late-stage bridgmanitic residues with high viscosity and elevated Fe/Mg-ratio and density. Since the core is undersaturated in oxygen and oversaturated in silica (Frost et al., 2010; Hirose et al., 2017), SiO_2 from the core would be exchanged with FeO from the BMO (Hirose et al., 2017), increasing the bridgmanite-to-ferropericlase ratio and thus the viscosity of the solid material. Another possible origin of dense bridgmanite could be an overturn by diapiric sinking of Fe-rich cumulates from the upper magma ocean, with subsequent melting and re-equilibration with the host rock (Ballmer et al., 2017). Fe-enriched bridgmanite has also been identified as a reasonable material to explain the anti-correlation of bulk sound and shear wave velocity, while basalt does not reproduce the observations (Deschamps et al., 2012).

Constraints on the temperature-dependence of viscosity in the lowermost mantle are limited. Most numerical models assume large thermal viscosity contrasts (e.g. Y. Li et al., 2014), although geoid constraints argue for a weak temperature-dependence (e.g. Yang & Gurnis, 2016). In contrast, the overall density of the LLSVPs has been estimated by Koelemeijer et al. (2017) and Lau et al. (2017), who argue for a neutral buoyancy of the LLSVP volume or a small excess density of about 0.5-1% in the lower part of the LLSVPs, respectively. This also agrees with geoid observations indicating that the upwelling material above the LLSVPs has to overcompensate dense material at the CMB to produce a geoid high (e.g. Liu & Zhong, 2015). However, these measured densities are smaller than those typically required for stability in numerical models of thermochemical convection, even when accounting for both chemical density and thermal expansion. In this work, we will show that a compositionally-dependent viscosity can strongly increase the temporal stability of thermochemical piles for smaller excess densities and lower temperature-dependence of viscosity compared to previous work.

I.2 Model setup

Our numerical models are run in 2-D spherical geometry using the finite element code CitcomS (Zhong et al., 2000; Tan et al., 2006). Conservation equations of mass, energy and momentum are solved using the Boussinesq approximation. Parameters described below are given in non-dimensional form and are listed in the Supporting Information (Table S1). The Rayleigh number describes the vigour of convection and is set to 10^7. The domain is a quarter of an annulus chosen along the equator with a grid of 313 by 91 nodes in longitude and depth, respectively. The mesh is refined in the lowermost 809 km, so that the effective resolution at the CMB is 17 km by 17 km. As discussed later, this resolution is not sufficient to capture the entrainment rates precisely, but allows for interpretation of time-integrated pile masses relevant for long-term stability. A constant uniform velocity boundary condition of 1.48 cm/year (Figure I.1a) is

imposed on the surface to force a single-plate degree-2 flow structure, while all other boundaries are free-slip. Heat is introduced into the system by basal and moderate internal heating. We track the advection of composition using tracer particles (McNamara & Zhong, 2004), 20 particles per element (a total of ~ 1.1 million), and the tracer-ratio method (Tackley & King, 2003) to determine the composition within each element. The density contrast between enriched and regular mantle is defined via the buoyancy ratio

$$B = \frac{\Delta \rho_C}{\alpha \rho \Delta T},$$

where $\Delta \rho_C$ is the density difference due to composition. α, ΔT and ρ are the thermal expansion coefficient, temperature difference and density, respectively.

Viscosity depends on temperature, depth and the composition, given by

$$
\begin{aligned}
\eta(z, T, C) &= \eta_0(z) \eta_{\Delta T}(z, T) \exp\left[C \ln \eta_C \right] \\
&= \eta_0(z) \exp\left[\frac{E_\eta(z)}{T^* + T_\eta(z)} - \frac{E_\eta(z)}{1 + T_\eta(z)} + C \ln \eta_C \right]
\end{aligned}
$$

with the non-dimensional temperature $T^* = \min(\max(T, 0), 1)$. The depth-dependence is implemented as stepwise adjustments of the viscosity prefactor η_0, the activation energy E_η and the temperature offset T_η (see Table S2). η_C is the viscosity contrast due to composition, and C is the composition value between 0 and 1. The thermal viscosity contrast $\eta_{\Delta T}$ describes the maximum potential viscosity variations due to temperature in the lower mantle and is varied in the range 2.3 to 330, while η_C assumes values between 1 and 20.

Models start with a dense layer at the core-mantle boundary (see Figure I.1a) and are run for at least 4.5 Gyrs. We calculate the remaining mass m and volume of the pile for each time step by defining elements as belonging to the pile if their composition is above a contour value of $cl = 0.8$ ($> 80\%$ pile material) and if they are connected to another pile element below or at the same depth. This algorithm hence accounts for all compositionally distinct patches connected to the core-mantle boundary and does not discriminate between all material occurring in a single pile or distributed between two or more.

I.3 Observed pile structures

Piles are characterized by the mass remaining after 4.5 Gyrs. Piles with about 80% retained mass can be considered stable, while piles with approximately 50% of the original mass are metastable. "Stable" piles with $> 80\%$ mass remaining are compact and have only small heterogeneities (Figure I.1c, $m \sim 91\%$), while almost no dense material is entrained in the mantle. In contrast, both entrainment and internal heterogeneities increase with decreasing compositional viscosity contrast (Figure I.1d, $m \sim 62\%$) and density (Figure I.1e, $m \sim 34\%$).

As a consequence, the mass remaining in the pile is significantly reduced. During the formation of the pile (compare Figure I.1b), the dense component is strongly deformed and parts of the material can get ripped off the coherent structure, but may later sink back towards the pile.
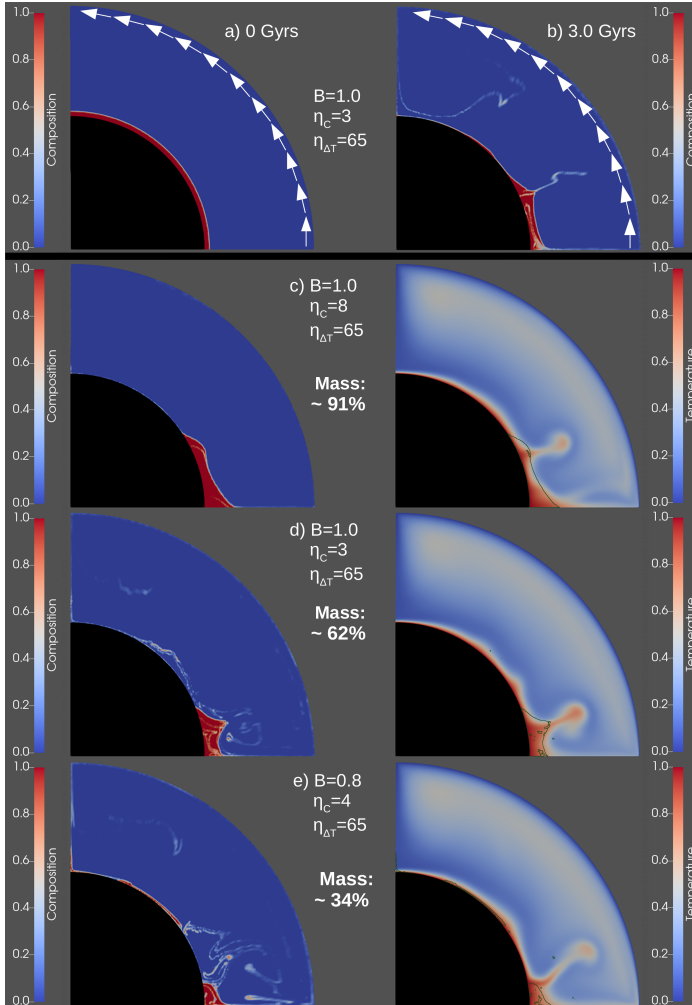

Figure I.1: (a) Initial condition and (b) snapshot after 3.0 Gyrs show composition for models that start with a dense layer and assume $B = 1.0$, $\eta_{\Delta T} = 65$ and $\eta_C = 3$, showing deformation and increased entrainment during the transition from a layer to a pile. White arrows indicate imposed plate velocity. (c)-(e) show examples of (left) the composition and (right) temperature of piles with remaining mass of (c) 91%, (d) 62%, and (e) 34% after 4.5 Gyrs, and the parameter combinations used to produce them. Dark lines in the temperature fields indicate the pile shapes for $cl = 0.8$.

For pile masses $< 50\%$, we observe a range of different structures. All of them are characterized by significant material loss, but pile shapes are considerably affected by the buoyancy ratio and the viscosity contrast. Patches of dense material can get detached from the pile and subsequently be advected with the flow (as seen in Figure I.1e). This process is amplified for low buoyancy ratios or in models where mixing between dense components and ambient mantle considerably reduces the initial density contrast. However, an increased viscosity allows patches of dense material to survive one or more mantle overturns before they are completely entrained. Metastable piles (around 50% mass) are in general strongly time-dependent, show a pronounced topography and an increased mobility both in lateral and in radial directions.

As can be seen in the temperature field (see Figures I.1c - I.1e, right panel), plumes rise primarily at the edges of the dense piles, as inferred from hotspots, large igneous provinces, and kimberlites (Steinberger & Torsvik, 2012; Torsvik et al., 2014, 2016), although these correlations have been questioned (Austermann et al., 2014; Davies et al., 2015). However, thermal instabilities grow along the CMB and are subsequently pushed towards the pile, where they reshape the edge of the dense material during ascent. Part of the dense component is entrained in the rising plume and may reach the surface. Less buoyant upwellings, consisting of plumes that have lost most of their excess temperature and were pushed on top of the pile, can be seen in Figure I.1c (right). This broader upwelling is strongly time-dependent and can entrain variable amounts of dense material, which may provide a potential source for heterogeneities observed in magmas of weak hotspots above LLSVPs (e.g. Chauvel et al., 2012).

I.4   Trade-off between buoyancy ratio and viscosity contrast

For models with a moderate buoyancy number of $B = 0.8$ (excess density of $\approx 2.6\%$ for $\Delta T = 3200\,\mathrm{K}$, see Table S1), stable piles can be obtained for $\eta_{\Delta T} = 65$ and $\eta_C = 6$ (Figure I.2a). However, almost 30% of the initial mass is lost and the pile exhibits heterogeneities within, indicating that stability may only be temporal. A higher compositional viscosity contrast of $\eta_C = 10$ as for the case in Figure I.2e increases the pile mass to about 87% and results in a more homogeneous pile. A similar, though less pronounced effect can be observed for a higher thermal viscosity contrast of $\eta_{\Delta T} = 330$ (Figure I.2c). In contrast to η_C, $\eta_{\Delta T}$ causes the pile to flatten instead of doming up (McNamara & Zhong, 2004; Bower et al., 2013) as observed in Figure I.2e.

If we increase the buoyancy ratio to $B = 1.0$, the pile mass does not change significantly, but the pile contains slightly fewer heterogeneities (Figure I.2f). However, the resulting pile structure exhibits a less pronounced topography. A reduction of the buoyancy ratio, or a lower viscosity contract η_C, both result in significantly more entrainment of dense material, which agrees with Davaille et al. (2002), and small, highly heterogeneous piles. Between $B = 0.7$ and $B = 1.2$

the chemical viscosity contrast necessary for stability increases with decreasing buoyancy ratio.
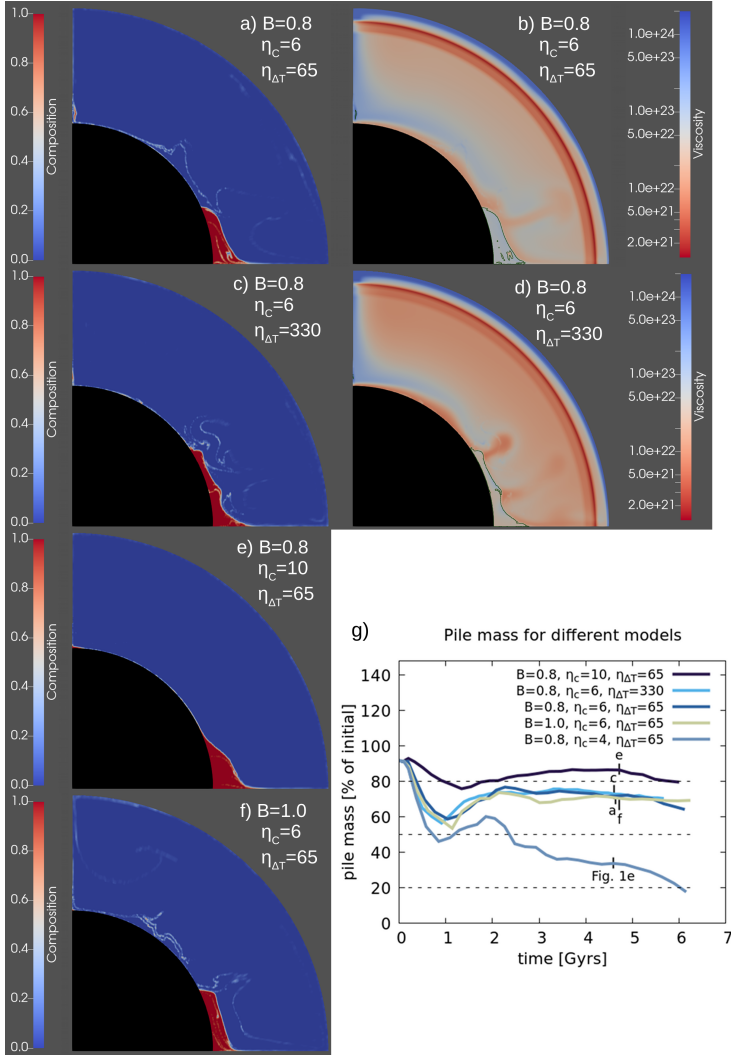

Figure I.2: Snapshots of different thermochemical models at 4.5 Gyrs. (a) Compositional and (b) viscosity fields for $B = 0.8$, $\eta_{\Delta T} = 65$, $\eta_C = 6$, and for the same parameters except $\eta_{\Delta T} = 330$ ((c) and (d), respectively). Dark lines in the viscosity fields outline the pile shapes for $cl = 0.8$. (e) and (f) Composition fields for $B = 0.8$, $\eta_{\Delta T} = 65$, $\eta_C = 10$ and $B = 1.0$, $\eta_{\Delta T} = 65$ and $\eta_C = 6$. (g) Temporal evolution of pile masses ($cl = 0.8$) for models discussed in (a)-(f) and Figure I.1e.

I. Stabilizing Effect of Compositional Viscosity Contrasts on Thermochemical Piles

The temporal evolution of the pile mass for five models discussed above is shown in Figure I.2g. As can be seen, all of them show a more or less pronounced loss of material during the first 1-2 Gyrs, while the pile mass slightly recovers afterwards for most models. This initial loss is caused by deformation of the starting layer (Figure I.1b) that depends on the initial temperature condition (McNamara & Zhong, 2004). During this period, η_C has more importance than B as both the case in Figure I.2a and Figure I.2f loose the same amount of mass, while the case in Figure I.2e does not. After ≈ 1.5 Gyrs, when material starts to reaccumulate to the pile, both B and η_C control how much ambient mantle will be included in the dense pile. This determines the effective density and viscosity of the pile and thus its long-term behavior, favoring dense piles for times beyond 6 Gyrs.
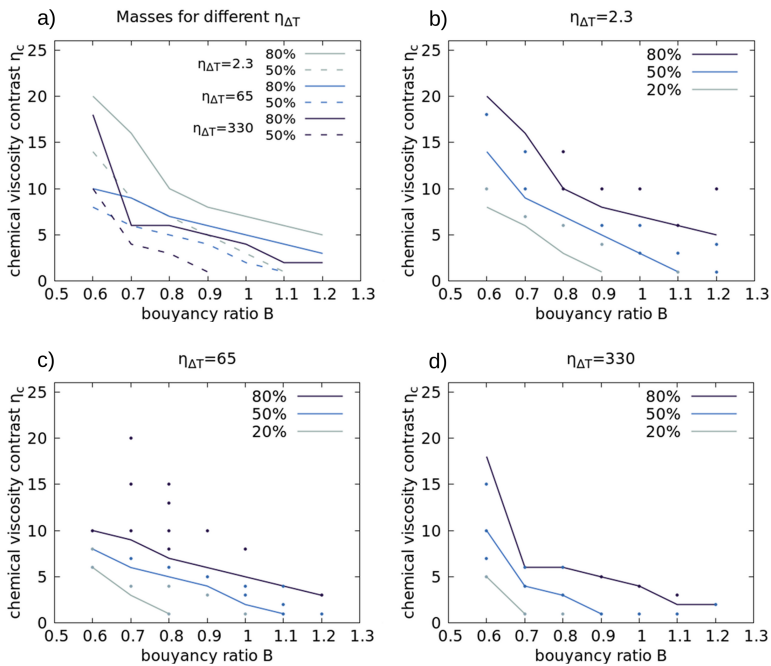

Figure I.3: (a) Overview of contour lines for 50% and 80% remaining mass as a function of B, $\eta_{\Delta T}$ and η_C. (b)-(d) show the observed fields of pile masses with dots indicating the tested parameter combinations for $\eta_{\Delta T} = 2.3$ (b), 65 (c) and 330 (d). Solid lines mark the expected contours of 20%, 50% and 80% mass remaining.

An overview of contour lines for the remaining mass as a function of buoyancy ratio B, compositional viscosity contrast η_C and thermal viscosity contrast $\eta_{\Delta T}$ (Figure I.3a) shows the trade-offs between these parameters. More detailed figures for thermal viscosity contrasts of $\eta_{\Delta T} = 2.3$, 65 and 330, including our tested models as data points (Figures I.3b - I.3d), show that the compositional

viscosity contrast necessary for pile stability decreases with increasing buoyancy ratio or increasing thermal viscosity contrast. This trend is consistent for all our models, except for some deviations for $B = 0.6$ (about 1.9% excess density), which marks a lower limit of stability. Models with smaller B (not shown) require significantly higher thermal or chemical viscosity contrasts $\eta_C > 100$ to avoid extensive entrainment of the dense material within 4.5 Gyrs. The observation of increased stability with larger $\eta_{\Delta T}$ is consistent with the results of Y. Li et al. (2014), although we need significantly lower thermal viscosity contrasts when adding even a small compositional viscosity contrast η_C. Our results indicate that the pile does not have to be more viscous than the slab (compare Figures I.2b and I.2d), but the plume-pile viscosity contrast (controlled by η_C) plays a major role.

I.5 Stability conditions for different pile deformation histories

Little is known about the initial conditions of pile formation. A compositionally layered mantle with a temperature gradient is a straightforward, but simplified, assumption. To explore the full range of possible initial conditions for composition, we also perform simulations in which we start our models with a fully-developed pile structure, which we obtain after 5.0 Gyrs for $B = 1.2$, $\eta_C = 10$ and $\eta_{\Delta T} = 2.3$. The thermal viscosity contrast is set to $\eta_{\Delta T} = 65$ and we observe a similar trade-off between buoyancy ratio and compositional viscosity contrast as before. However, significantly decreasing either (or even both) B and η_C still results in stable thermochemical piles. As can be seen in Figures I.4c and I.4d, a buoyancy ratio of $B = 0.9$ for $\eta_C = 3$ or no compositional viscosity contrast ($\eta_C = 1$) for $B = 1.0$ are sufficient to keep entrainment low, while these combinations of parameters are not suitable to form stable piles if we start with a layer of dense material (Figures I.4a and I.4b).

If we compare the temporal evolution of the pile mass for models starting with a pile to those that start with a dense basal layer as shown in Figure I.4e, the strong influence of deformation-induced entrainment during pile formation becomes apparent. The pile mass for models with preformed structures stays almost constant or decreases only slightly with time, while calculations starting with a dense layer show the characteristic mass loss during the first 1-2 Gyrs as discussed above, without permanent recovery. Hence, the requirements for stability depend on the initial configuration of the dense material and temperature, and the observed entrainment during pile formation may result from destruction of the initial temperature gradient. This is because strong deformation, e.g. as required to form piles, is accompanied by increased entrainment and mixing between dense material and ambient mantle.
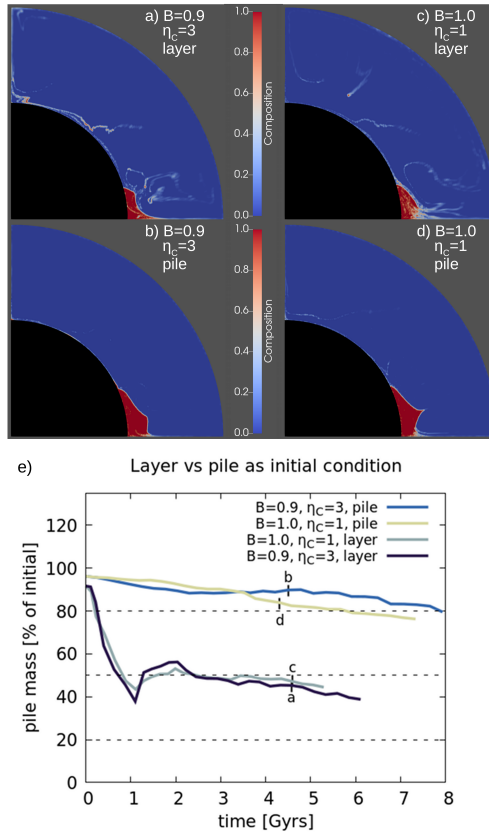
Figure I.4: Comparison of compositional structures 4.5 Gyrs after starting models with (top row) a dense basal layer and (bottom row) a fully-developed pile. (a) and (b) compare results for $B = 0.9$ and $\eta_C = 3$; (c) and (d) compare results for $B = 1.0$ and $\eta_C = 1$; all models use $\eta_{\Delta T} = 65$. (e) Temporal evolution of the pile mass ($cl = 0.8$) for models in (a)-(d). The higher mass at $t = 0$ for pile models is due to compaction and reduction of surface area during pile formation for $B = 1.2$.

I.6 Discussion

As already mentioned in Section I.2, the chosen resolution is not sufficient to resolve details of the entrainment rate, which occurs on length scales $<1\,\mathrm{km}$ (e.g. Davaille et al., 2002; Jellinek & Manga, 2002). To ensure that our models still qualitatively capture the dynamics of the dense material, we performed tests with different resolutions. The results show a similar behavior, although lower resolution overestimates material loss (cf. Figure S1). A more detailed discussion can be found in the Supporting Information. In general, our model setup may underestimate the entrainment after pile formation because we

assume a stable convection pattern, which might not be true throughout Earth's history. However, tests with reversed plate velocity after pile formation indicate that piles tend to persist if they survive formation with $m > 80\%$ (Figure S2).

Since we force the flow to a degree-2 structure, we cannot fully investigate stability with respect to pile position or spherical harmonic degree. However, piles react to changes in mantle flow, e.g. thermal instabilities next to the pile margin. Growing instabilities deflect the pressure that downwellings apply to the pile, allowing the dense material to flatten. When the plume is finally pushed against the edge of the pile, the LLSVP structure is compressed and lifted upwards, resulting in steep sides. A lower density contrast or a lower compositional viscosity of the pile amplifies this radial and horizontal movement because the material can react more rapidly.

In our models, we assume primordial material as a source for the LLSVPs, in agreement with e.g. Deschamps et al. (2012). However, subducted MORB accumulating at the CMB may also be a candidate (e.g. Mulyukova et al., 2015), although this process is still under debate (M. Li & McNamara, 2013). The high bulk modulus of basalt reduces its excess density with depth, which causes almost neutral buoyancy of the material at CMB conditions (M. Li & McNamara, 2013; Mulyukova et al., 2015; Ballmer et al., 2016). In our models, even intrinsically strong piles require an original excess density of $\sim 1.9\%$ during pile formation, which argues for primordial material. This inferred excess density is larger than estimated by Koelemeijer et al. (2017) and Lau et al. (2017), but most of our piles contain small portions of ambient mantle, which reduces the pile's overall excess density. A similar reduction would be caused by small portions of basalt mixing into the primordial material (Ballmer et al., 2016), but MORB's intrinsic high viscosity would not impact pile viscosity as much (Ballmer et al., 2016). Consequently, we do not expect a significant impact on pile stability for small fractions of basalt mixing into the pile after its formation.

I.7 Conclusions

Our 2-D calculations indicate a strong impact of compositional viscosity contrasts on the stability of dense pile structures, especially for low thermal viscosity contrasts (e.g. Yang & Gurnis, 2016). In agreement with Davaille et al. (2002), internal viscosity due to composition significantly reduces pile entrainment rates, especially during stages of strong deformation of the dense material. In general, the chemical viscosity contrasts necessary for pile stability decrease with increasing thermal viscosity contrast and/or buoyancy ratio. For our calculations, a limit of stability is reached at about 1.9% excess density ($B = 0.56$), as lower excess density requires considerably higher compositional and/or thermal viscosity contrasts than we used. Requirements for stability are lower if the dense material does not have to survive an initial overturn event. However, if the reaction between mantle and core has been extensive enough to convert

the dense component to pure bridgmanite, we may expect a chemical viscosity increase of up to 3 orders of magnitude, which may stabilize piles for even smaller excess densities. On the other hand, mixing between pile material and ambient mantle or subducted basalt can reduce the effective density during pile formation or deformation.

We find that the requirements for long-term pile stability are determined by the pile's deformation history. For example, long-term stability of LLSVP structures is likely if they survive their initial formation without critical mass loss. However, our results assume spatial stability of the piles. Since strong entrainment of pile material is confined to periods of intense deformation, pile survival following a change from degree-2 to degree-1 structure or vice versa should require higher viscosities or densities than compared to survival beneath an enduring degree-2 structure.

The Supporting Information can be found in Appendix A

References

Austermann, J., Kaye, B. T., Mitrovica, J. X., & Huybers, P. (2014, 01). A statistical analysis of the correlation between large igneous provinces and lower mantle seismic structure. *Geophysical Journal International*, *197*(1), 1–9. Retrieved from `https://doi.org/10.1093/gji/ggt500` doi: 10.1093/gji/ggt500

Ballmer, M. D., Lourenco, D. L., Hirose, K., Caracas, R., & Nomura, R. (2017). Reconciling magma-ocean crystallization models with the present-day structure of the earth's mantle. *Geochemistry, Geophysics, Geosystems*, *18*(7), 2785–2806. Retrieved from `https://agupubs.onlinelibrary.wiley.com/doi/abs/10.1002/2017GC006917` doi: 10.1002/2017GC006917

Ballmer, M. D., Schumacher, L., Lekic, V., Thomas, C., & Ito, G. (2016). Compositional layering within the large low shear-wave velocity provinces in the lower mantle. *Geochemistry, Geophysics, Geosystems*, *17*(12), 5056–5077. Retrieved from `https://agupubs.onlinelibrary.wiley.com/doi/abs/10.1002/2016GC006605` doi: 10.1002/2016GC006605

Bower, D. J., Gurnis, M., & Seton, M. (2013). Lower mantle structure from paleogeographically constrained dynamic earth models. *Geochemistry,*

Geophysics, Geosystems, *14*(1), 44–63. Retrieved from `https://agupubs
.onlinelibrary.wiley.com/doi/abs/10.1029/2012GC004267` doi:
10.1029/2012GC004267

Chauvel, C., Maury, R. C., Blais, S., Lewin, E., Guillou, H., Guille, G., . . .
Gutscher, M.-A. (2012). The size of plume heterogeneities constrained
by marquesas isotopic stripes. *Geochemistry, Geophysics, Geosystems*,
13(7). Retrieved from `https://agupubs.onlinelibrary.wiley.com/
doi/abs/10.1029/2012GC004123` doi: 10.1029/2012GC004123

Conrad, C. P., Steinberger, B., & Torsvik, T. H. (2013, June). Stability of active
mantle upwelling revealed by net characteristics of plate tectonics. *Nature*,
498, 479–482. Retrieved from `https://www.nature.com/articles/
nature12203#supplementary-information` doi: 10.1038/nature12203;
10.1038/nature12203

Cottaar, S., & Lekic, V. (2016, 08). Morphology of seismically slow lower-
mantle structures. *Geophysical Journal International*, *207*(2), 1122–
1136. Retrieved from `https://doi.org/10.1093/gji/ggw324` doi:
10.1093/gji/ggw324

Davaille, A., Girard, F., & Bars, M. L. (2002). How to anchor hotspots
in a convecting mantle? *Earth and Planetary Science Letters*, *203*(2),
621–634. Retrieved from `http://www.sciencedirect.com/science/
article/pii/S0012821X0200897X` doi: 10.1016/S0012-821X(02)00897-
X

Davies, D. R., Goes, S., Davies, J., Schuberth, B., Bunge, H.-P., &
Ritsema, J. (2012). Reconciling dynamic and seismic models of
earth's lower mantle: The dominant role of thermal heterogene-
ity. *Earth and Planetary Science Letters*, *353-354*, 253–269. Re-
trieved from `http://www.sciencedirect.com/science/article/pii/
S0012821X1200444X` doi: 10.1016/j.epsl.2012.08.016

Davies, D. R., Goes, S., & Sambridge, M. (2015). On the rela-
tionship between volcanic hotspot locations, the reconstructed erup-
tion sites of large igneous provinces and deep mantle seismic struc-
ture. *Earth and Planetary Science Letters*, *411*, 121–130. Re-
trieved from `http://www.sciencedirect.com/science/article/pii/
S0012821X14007523` doi: 10.1016/j.epsl.2014.11.052

Deschamps, F., Cobden, L., & Tackley, P. J. (2012). The primitive
nature of large low shear-wave velocity provinces. *Earth and Plan-
etary Science Letters*, *349-350*, 198–208. Retrieved from `http://
www.sciencedirect.com/science/article/pii/S0012821X12003718`
doi: 10.1016/j.epsl.2012.07.012

Dziewonski, A. M., Lekic, V., & Romanowicz, B. A. (2010).
Mantle anchor structure: An argument for bottom up tecton-
ics. *Earth and Planetary Science Letters*, *299*(1), 69–79. Re-
trieved from `http://www.sciencedirect.com/science/article/pii/
S0012821X10005236` doi: 10.1016/j.epsl.2010.08.013

Frost, D. J., Asahara, Y., Rubie, D. C., Miyajima, N., Dubrovinsky, L. S.,
Holzapfel, C., . . . Sakai, T. (2010). Partitioning of oxygen between the

earth's mantle and core. *Journal of Geophysical Research: Solid Earth*, *115*(B2). Retrieved from `https://agupubs.onlinelibrary.wiley` `.com/doi/abs/10.1029/2009JB006302` doi: 10.1029/2009JB006302

Garnero, E. J., & McNamara, A. K. (2008). Structure and dynamics of earth's lower mantle. *Science*, *320*(5876), 626–628. Retrieved from `https://science.sciencemag.org/content/320/5876/626` doi: 10.1126/science.1148028

Garnero, E. J., McNamara, A. K., & Shim, S.-H. (2016, June). Continent-sized anomalous zones with low seismic velocity at the base of earth's mantle. *Nature Geoscience*, *9*, 481–489. Retrieved from `https://www` `.nature.com/articles/ngeo2733#supplementary-information` doi: 10.1038/ngeo2733; 10.1038/ngeo2733

Hager, B. H., Clayton, R. W., Richards, M. A., Comer, R. P., & Dziewonski, A. M. (1985). Lower mantle heterogeneity, dynamic topography and the geoid. *Nature*, *313*(6003), 541–545. doi: 10.1038/313541a0; 10.1038/313541a0

Hirose, K., Morard, G., Sinmyo, R., Umemoto, K., Hernlund, J., Helffrich, G., & Labrosse, S. (2017, February). Crystallization of silicon dioxide and compositional evolution of the earth's core. *Nature*, *543*, 99–102. doi: 10.1038/nature21367; 10.1038/nature21367

Jellinek, A. M., & Manga, M. (2002). The influence of a chemical boundary layer on the fixity, spacing and lifetime of mantle plumes. *Nature*, *418*(6899), 760–763. doi: 10.1038/nature00979; 10.1038/nature00979

Koelemeijer, P. J., Deuss, A., & Ritsema, J. (2017, May). Density structure of earth's lowermost mantle from stoneley mode splitting observations. *Nature Communications*, *8*, 15241. Retrieved from `https://www.nature` `.com/articles/ncomms15241#supplementary-information` doi: 10.1038/ncomms15241; 10.1038/ncomms15241

Labrosse, S., Hernlund, J. W., & Coltice, N. (2007, December). A crystallizing dense magma ocean at the base of the earth's mantle. *Nature*, *450*, 866–869. Retrieved from `https://www.nature.com/articles/` `nature06355#supplementary-information` doi: 10.1038/nature06355; 10.1038/nature06355

Lau, H. C. P., Mitrovica, J. X., Davis, J. L., Tromp, J., Yang, H.-Y., & Al-Attar, D. (2017, November). Tidal tomography constrains earth's deep-mantle buoyancy. *Nature*, *551*, 321–326. doi: 10.1038/nature24452; 10.1038/nature24452

Lekic, V., Cottaar, S., Dziewonski, A., & Romanowicz, B. (2012). Cluster analysis of global lower mantle tomography: A new class of structure and implications for chemical heterogeneity. *Earth and Planetary Science Letters*, *357-358*, 68–77. Retrieved from `http://www.sciencedirect.com/science/` `article/pii/S0012821X12005109` doi: 10.1016/j.epsl.2012.09.014

Li, M., & McNamara, A. K. (2013). The difficulty for subducted oceanic crust to accumulate at the earth's core-mantle boundary. *Journal of Geophysical Research: Solid Earth*, *118*(4), 1807–1816. Retrieved from `https://agupubs.onlinelibrary.wiley.com/doi/abs/` `10.1002/jgrb.50156` doi: 10.1002/jgrb.50156

Li, M., McNamara, A. K., & Garnero, E. J. (2014, March). Chemical complexity of hotspots caused by cycling oceanic crust through mantle reservoirs. *Nature Geoscience*, *7*, 366–370. Retrieved from `https://www.nature.com/articles/ngeo2120#supplementary-information` doi: 10.1038/ngeo2120; 10.1038/ngeo2120

Li, Y., Deschamps, F., & Tackley, P. J. (2014, 09). The stability and structure of primordial reservoirs in the lower mantle: insights from models of thermochemical convection in three-dimensional spherical geometry. *Geophysical Journal International*, *199*(2), 914–930. Retrieved from `https://doi.org/10.1093/gji/ggu295` doi: 10.1093/gji/ggu295

Li, Y., Deschamps, F., & Tackley, P. J. (2015). Effects of the post-perovskite phase transition properties on the stability and structure of primordial reservoirs in the lower mantle of the earth. *Earth and Planetary Science Letters*, *432*, 1–12. Retrieved from `http://www.sciencedirect.com/science/article/pii/S0012821X15006159` doi: 10.1016/j.epsl.2015.09.040

Liu, X., & Zhong, S. (2015). The long-wavelength geoid from three-dimensional spherical models of thermal and thermochemical mantle convection. *Journal of Geophysical Research: Solid Earth*, *120*(6), 4572–4596. Retrieved from `https://agupubs.onlinelibrary.wiley.com/doi/abs/10.1002/2015JB012016` doi: 10.1002/2015JB012016

McNamara, A. K., & Zhong, S. (2004). Thermochemical structures within a spherical mantle: Superplumes or piles? *Journal of Geophysical Research: Solid Earth*, *109*(B7). Retrieved from `https://agupubs.onlinelibrary.wiley.com/doi/abs/10.1029/2003JB002847` doi: 10.1029/2003JB002847

McNamara, A. K., & Zhong, S. (2005). Thermochemical structures beneath africa and the pacific ocean. *Nature*, *437*(7062), 1136–1139. doi: 10.1038/nature04066; 10.1038/nature04066

Mulyukova, E., Steinberger, B., Dabrowski, M., & Sobolev, S. V. (2015). Survival of llsvps for billions of years in a vigorously convecting mantle: Replenishment and destruction of chemical anomaly. *Journal of Geophysical Research: Solid Earth*, *120*(5), 3824–3847. Retrieved from `https://agupubs.onlinelibrary.wiley.com/doi/abs/10.1002/2014JB011688` doi: 10.1002/2014JB011688

Nakagawa, T., & Tackley, P. J. (2011). Effects of low-viscosity post-perovskite on thermo-chemical mantle convection in a 3-d spherical shell. *Geophysical Research Letters*, *38*(4). Retrieved from `https://agupubs.onlinelibrary.wiley.com/doi/abs/10.1029/2010GL046494` doi: 10.1029/2010GL046494

Schuberth, B. S. A., Bunge, H.-P., & Ritsema, J. (2009). Tomographic filtering of high-resolution mantle circulation models: Can seismic heterogeneity be explained by temperature alone? *Geochemistry, Geophysics, Geosystems*, *10*(5). Retrieved from `https://agupubs.onlinelibrary.wiley.com/doi/abs/10.1029/2009GC002401` doi: 10.1029/2009GC002401

Schuberth, B. S. A., Bunge, H.-P., Steinle-Neumann, G., Moder, C., & Oeser, J. (2009). Thermal versus elastic heterogeneity in high-

resolution mantle circulation models with pyrolite composition: High plume excess temperatures in the lowermost mantle. *Geochemistry, Geophysics, Geosystems*, *10*(1). Retrieved from `https://agupubs .onlinelibrary.wiley.com/doi/abs/10.1029/2008GC002235` doi: 10.1029/2008GC002235

Schuberth, B. S. A., Zaroli, C., & Nolet, G. (2012, 03). Synthetic seismograms for a synthetic earth: long-period p- and s-wave traveltime variations can be explained by temperature alone. *Geophysical Journal International*, *188*(3), 1393–1412. Retrieved from `https://doi.org/10.1111/j.1365 -246X.2011.05333.x` doi: 10.1111/j.1365-246X.2011.05333.x

Simmons, N. A., Forte, A. M., & Grand, S. P. (2009, 06). Joint seismic, geodynamic and mineral physical constraints on three-dimensional mantle heterogeneity: Implications for the relative importance of thermal versus compositional heterogeneity. *Geophysical Journal International*, *177*(3), 1284–1304. Retrieved from `https://doi.org/10.1111/j.1365-246X .2009.04133.x` doi: 10.1111/j.1365-246X.2009.04133.x

Steinberger, B., & Torsvik, T. H. (2012). A geodynamic model of plumes from the margins of large low shear velocity provinces. *Geochemistry, Geophysics, Geosystems*, *13*(1). Retrieved from `https://agupubs .onlinelibrary.wiley.com/doi/abs/10.1029/2011GC003808` doi: 10.1029/2011GC003808

Tackley, P. J. (2012). Dynamics and evolution of the deep mantle resulting from thermal, chemical, phase and melting effects. *Earth-Science Reviews*, *110*(1), 1–25. Retrieved from `http:// www.sciencedirect.com/science/article/pii/S0012825211001486` doi: 10.1016/j.earscirev.2011.10.001

Tackley, P. J., & King, S. D. (2003). Testing the tracer ratio method for modeling active compositional fields in mantle convection simulations. *Geochemistry, Geophysics, Geosystems*, *4*(4). Retrieved from `https://agupubs .onlinelibrary.wiley.com/doi/abs/10.1029/2001GC000214` doi: 10.1029/2001GC000214

Tan, E., Choi, E., Thoutireddy, P., Gurnis, M., & Aivazis, M. (2006). Geoframework: Coupling multiple models of mantle convection within a computational framework. *Geochemistry, Geophysics, Geosystems*, *7*(6). Retrieved from `https://agupubs.onlinelibrary.wiley.com/ doi/abs/10.1029/2005GC001155` doi: 10.1029/2005GC001155

Torsvik, T. H., Burke, K., Steinberger, B., Webb, S. J., & Ashwal, L. D. (2010, July). Diamonds sampled by plumes from the core–mantle boundary. *Nature*, *466*, 352–355. Retrieved from `https://www.nature .com/articles/nature09216#supplementary-information` doi: 10.1038/nature09216; 10.1038/nature09216

Torsvik, T. H., Steinberger, B., Ashwal, L. D., Doubrovine, P. V., & Trønnes, R. G. (2016). Earth evolution and dynamics—a tribute to kevin burke. *Canadian Journal of Earth Sciences*, *53*(11), 1073–1087. Retrieved from `https://doi.org/10.1139/cjes-2015-0228` doi: 10.1139/cjes-2015-0228

Torsvik, T. H., van der Voo, R., Doubrovine, P. V., Burke, K., Steinberger, B., Ashwal, L. D., . . . Bull, A. L. (2014). Deep mantle structure as a reference frame for movements in and on the earth. *Proceedings of the National Academy of Sciences*, *111*(24), 8735–8740. Retrieved from `https://www.pnas.org/content/111/24/8735` doi: 10.1073/pnas.1318135111

Yang, T., & Gurnis, M. (2016, 09). Dynamic topography, gravity and the role of lateral viscosity variations from inversion of global mantle flow. *Geophysical Journal International*, *207*(2), 1186–1202. Retrieved from `https://doi.org/10.1093/gji/ggw335` doi: 10.1093/gji/ggw335

Zhong, S., Zuber, M. T., Moresi, L., & Gurnis, M. (2000). Role of temperature-dependent viscosity and surface plates in spherical shell models of mantle convection. *Journal of Geophysical Research: Solid Earth*, *105*(B5), 11063–11082. Retrieved from `https://agupubs.onlinelibrary.wiley.com/doi/abs/10.1029/2000JB900003` doi: 10.1029/2000JB900003

Paper II

How thermochemical piles periodically generate plumes at their egdes

Björn H. Heyn, Clinton P. Conrad, Reidar G. Trønnes

Under review in *Journal of Geopyhsical Research: Solid Earth*

Abstract

Deep-rooted mantle plumes are thought to originate from the margins of the Large Low Shear Velocity Provinces (LLSVPs) at the base of the mantle. Visible in seismic tomography, the LLSVPs are interpreted to be dense and viscous thermochemical piles in numerical models. Although the piles force lateral mantle flow upwards at their edges, the mechanism for localized plume formation is still not well understood. In this study, we develop numerical models that show plumes rising from the margin of a dense thermochemical pile, temporarily increasing its local thickness until material at the pile top cools and the pile starts to collapse back towards the core-mantle boundary (CMB). This causes the dense pile material to spread laterally along the CMB, locally thickening the lower thermal boundary layer on the CMB next to the pile, and initiating a new plume. The resulting plume cycle is reflected in both the thickness and lateral motion of the local pile margin within a few degrees of the pile edge, while the overall thickness of the pile is not affected. The period of plume generation is mainly controlled by the rate at which slab material is transported to the CMB, and thus depends on the plate velocity and the sinking rate of slabs in the lower mantle. This mechanism for plume initiation may explain the observed clustering of Large Igneous Provinces (LIPs) in the southeastern corner of the African LLSVP around 95-155 Ma.

II.1 Introduction

All seismic tomographic models throughout the last decades show a similar degree-2 pattern for the Earth's lowermost mantle (e.g., Hager et al., 1985; Dziewonski et al., 2010; Garnero et al., 2016), dominated by the presence of two so-called Large Low Shear Velocity Provinces (LLSVPs) (Garnero & McNamara, 2008; Dziewonski et al., 2010; Garnero et al., 2016) centered beneath Africa and the Pacific (Garnero & McNamara, 2008; Lekic et al., 2012; Cottaar &

Lekic, 2016). Although the various tomographic models suggest slightly different shapes and thicknesses of these structures, there is in general good agreement about the positions of their outlines (Cottaar & Lekic, 2016). Hotspots related to deep-roted plumes seem to be located at the LLSVP margins (French & Romanowicz, 2015; Torsvik et al., 2016). Although most studies indicate and favor a thermochemical origin of the LLSVP structures, in which they represent piles of hot and dense material (e.g., McNamara & Zhong, 2004, 2005; Nakagawa & Tackley, 2011; Tackley, 2012; Y. Li et al., 2014, 2015; Mulyukova et al., 2015), some studies suggest that they may be simple accumulations of thermal plumes swept together by mantle flow (e.g., Schuberth, Bunge, Steinle-Neumann, et al., 2009; Schuberth, Bunge, & Ritsema, 2009; Schuberth et al., 2012; Davies et al., 2012).

If the LLSVPs consist of dense material, they are likely composed of either recycled oceanic crust (mid-ocean ridge basalt, MORB) (Hirose et al., 2005; M. Li & McNamara, 2013; M. Li et al., 2014; Mulyukova et al., 2015) or primordial iron-rich cumulates (McNamara & Zhong, 2004, 2005; Nakagawa & Tackley, 2011; Y. Li et al., 2014, 2015) that crystallized at a late stage from the basal magma ocean (Labrosse et al., 2007). At lower mantle conditions, basalt is expected to have significantly lower chemical excess density than primordial material (Mulyukova et al., 2015; Ballmer et al., 2016), which presents difficulties in accumulating enough material to form stable thermochemical piles (M. Li & McNamara, 2013). Constraints on the total excess density of LLSVPs (including both thermal and chemical effects) have been obtained through the analysis of normal modes or Earth's solid tides, but the methods average over the lowermost few hundred to 1000 km (Lau et al., 2017) and results vary from slightly positively buoyant LLSVP areas to an excess density of about 0.5-1.0% (Koelemeijer et al., 2017; Lau et al., 2017). Although their excess densities are different, both basalt and primordial iron-rich cumulates are likely to have increased intrinsic viscosity due to their composition (Hirose et al., 2005; Ballmer et al., 2016; Trønnes et al., 2019). Opposed to this, weak post-bridgmanite (see Table 1 in Trønnes et al. (2019)) may reduce the viscosity of the slabs (e.g., Torsvik et al., 2016) or also parts of the LLSVPs (Koelemeijer et al., 2018; Trønnes et al., 2019) by three to four orders of magnitude (Ammann et al., 2010). As a consequence, and because we cannot measure it directly, the viscosity structures of the lowermost mantle and D" areas are hardly constrained.

One of the most debated aspects of LLSVPs, apart from their origin, is their stability with respect to space and time. It has been shown, both numerically and in laboratory experiments, that a certain excess density is required to avoid extensive entrainment of pile material within mantle plumes (e.g., Davaille et al., 2002; Tackley, 2012; Heyn et al., 2018). A high temperature-dependence of viscosity (Y. Li et al., 2014) or an increase in viscosity due to composition (Davaille et al., 2002; Heyn et al., 2018) can help to increase the amount of LLSVP material that survives ongoing convection. With respect to spatial stability, Conrad et al. (2013) show that the positions of net divergence in

plate motion are stably located above the current positions of the LLSVPs, and that these positions have remained stable for at least 250 Myr. Furthermore, reconstructed eruption sites of large Igneous Provinces (LIPs, Figure II.1) and kimberlites have been used to argue that the degree-2 structure of the lowermost mantle has been stable for at least the last 300 Myr, assuming that they are related to plumes rising almost vertically (French & Romanowicz, 2015) from the edges of the LLSVPs where they are generated (Torsvik et al., 2006, 2010; Steinberger & Torsvik, 2012; Torsvik et al., 2016). Although the correlation between projected pile margins and the locations of eruption locations has been questioned (Austermann et al., 2014; Davies et al., 2015), geodynamic models show both plumes rising at the edges and/or the centres of thermochemical piles (McNamara & Zhong, 2004, 2005; Steinberger & Torsvik, 2012; M. Li & Zhong, 2017; Dannberg & Gassmöller, 2018; Heyn et al., 2018).
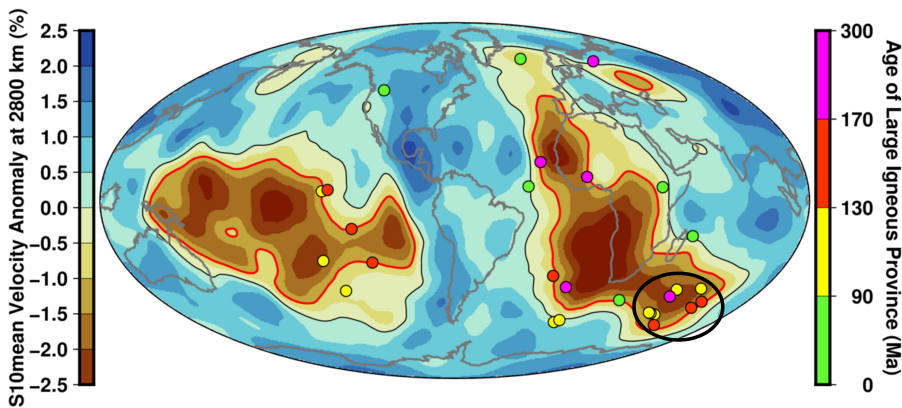

Figure II.1: Distribution of reconstructed eruption sites of LIPs (Torsvik, 2019) around the two Large Low Shear Wave Velocity Provinces (LLSVPs) indicated by velocity anomalies of the S10mean shear wave tomography model of Doubrovine et al. (2016). Contour lines are drawn for 0.0% (black) and -1.0% (red) velocity anomalies. Reconstructed eruption sites of LIPs are marked by circles, with color corresponding to age. There is a cluster of 9 LIPs around the southeastern corner of the African LLSVP (marked by black circle), of which 8 erupted between 155-95 Ma (red and yellow circles) and one at 285 Ma (purple circle).

So far, interactions between plumes and pile margins have mostly been investigated with respect to formation of zoned plumes and the behavior of rheologic and compositional heterogeneities within the plume conduit (Dannberg & Sobolev, 2015; Dannberg & Gassmöller, 2018; Farnetani et al., 2018). Yet, these models do not consider the long-term evolution of plume-pile interaction, nor do they investigate the mechanism for how plumes form at the edges of the piles. One idea is that the flow along the core-mantle boundary (CMB), induced by the slabs sinking between the LLSVPs, is forced upwards at the pile

edges and thereby results in plumes (Steinberger & Torsvik, 2012; Torsvik et al., 2016; M. Li & Zhong, 2017; Dannberg & Gassmöller, 2018). However, none of these studies explore in more detail how plumes are generated at the CMB, i.e. how the lower thermal boundary layer becomes thickened sufficently to become unstable and form a plume. M. Li and Zhong (2017) discuss the growth of the thermal boundary layer and conditions for forming instabilities, but do not specifically investigate the influence of a dense thermochemical pile in that process. However, they do show that either decreasing thermal expansivity or increasing conductivity with depth reduce the number of plumes forming from a thermal boundary layer outside dense piles.

Although the use of plate motion history has proven to play a role in focusing mantle upwellings is specific areas of the CMB (Davies et al., 2012; M. Li & Zhong, 2017), only a small fraction of randomly initated plumes from the lower thermal boundary layer end up in locations close to present day hotspots (French & Romanowicz, 2015). Thus, plate history alone cannot explain the uneven distribution of present-day hotspots around the LLSVP margins (French & Romanowicz, 2015). Going back in time, eruption sites of LIPs indicate the persistence of an uneven plume distribution for the last 300 Myr, even though the record of LIPs is most likely incomplete due to subducted oceanic LIPs (Torsvik et al., 2016; Torsvik, 2019). Nevertheless, a concentration of 8 LIPs erupted between 95-155 Ma in the southeastern corner of the African LLSVP (Figure II.1) presents an example of plume initiation in close proximity both with respect to space and time (Torsvik et al., 2016; Torsvik, 2019). This proximity is difficult to explain by random plume initiation.

Consequently, we require a mechanism that locally increases the thickness of the lower thermal boundary layer enough to become unstable at certain areas of the pile edges, while most of the LLSVP margins remain passive at the same time. A first step was done by M. Li et al. (2018), who showed that pile motion in response to rising plumes can affect the generation of new thermal instabilities, resulting in an almost periodic behavior. Yet, in their models, plumes rise from the centre of tent-shaped piles that move up and down. In this study, we present an alternative mechanism and show that plumes can be periodically generated at pile margins by a local collapse of the pile edge. Furthermore, we investigate controls on the periodicity of this process, and discuss how we may use plume observations to develop new constraints on the viscosity structure of the lower mantle and the LLSVPs.

II.2 Model setup

II.2.1 Model parameters and initial condition

Our numerical models are run in 2-D spherical geometry using the finite element code ASPECT (Kronbichler et al., 2012; Heister et al., 2017; He et al., 2017; Bangerth et al., 2018, 2019). Conservation equations for mass, energy and

momentum are solved using the Boussinesq approximation. Our setup is similar to Heyn et al. (2018), and we choose parameters so that the reference Rayleigh number for the mantle, which describes the vigor of convection and is defined as

$$Ra = \frac{\alpha \rho g \Delta T d^3}{\kappa \eta}, \tag{II.1}$$

is set to 10^7. Parameters are the thermal expansivity α, the density ρ, the temperature drop across the mantle ΔT, the gravitational acceleration g, the mantle thickness d, the reference viscosity η and the thermal diffusivity κ. We use a quarter of an annulus along the equator as a domain, with a grid that is adaptively refined every 10 time steps based on compositon and viscosity gradients. The effective resolution (lateral x radial) thus varies between about 7×11 km and 80×90 km. All parameters characterizing the general setup are given in Table II.1.

Following Heyn et al. (2018), we impose a constant uniform velocity boundary condition of 1.48 cm/year on the surface to force a single-plate degree-2 flow structure (Figure II.2), while all other boundaries are free-slip. However, in order to test the influence of the velocity boundary condition on our results, we also perform tests in which we vary the velocity between 0.74 and 2.96 cm/yr or apply a time-varying periodic plate velocity. For the latter, the velocity is given as

$$v_{\text{Plate}} = v_0 \left(1.2 + \cos \left(\frac{2\pi}{\mathcal{T}_{\text{Plate}}} \cdot (t - t_0) \right) \right), \tag{II.2}$$

where the reference velocity is $v_0 = 1.25$ cm/year, t is time in years, the start time of the model is $t_0 = 6.5 \cdot 10^9$ years, and the plate velocity period is $\mathcal{T}_{\text{Plate}}$, which is varied between 125 and 1000 Myr. The effective velocity always oscillates between 0.296 and 3.256 cm/yr. This setup ensures that the degree-2 structure is never destroyed and that subduction never ceases completely.

Heat is introduced into the system by basal and internal heating (Table II.1). Dense piles are represented by a compositional field that is advected using the discontinuous Galerkin method (He et al., 2017). The density contrast between enriched and regular mantle is defined via the buoyancy ratio

$$B = \frac{\Delta \rho_C}{\alpha \rho \Delta T}, \tag{II.3}$$

where $\Delta \rho_C$ is the density difference due to composition.

As in Heyn et al. (2018), viscosity depends on temperature, depth and composition, given by

$$\begin{aligned} \eta(z, T, C) &= \eta_0(z) \eta_{\Delta T}(z, T) \exp \left[C \ln \eta_C \right] \\ &= \eta_0(z) \exp \left[\frac{E_\eta(z)}{T^* + T_\eta(z)} - \frac{E_\eta(z)}{1 + T_\eta(z)} + C \ln \eta_C \right] \end{aligned} \tag{II.4}$$

where the non-dimensionalised temperature T^* is restricted to values between 0 and 1. Non-dimensionalisation is achieved using the surface and the CMB temperatures as references for $T^* = 0$ and $T^* = 1$, respectively. The depth-dependence is implemented as stepwise adjustments of the viscosity prefactor η_0, the non-dimensional activation energy E_η and the non-dimensional temperature offset T_η (see Table II.2). C is the composition value between 0 and 1, and η_C is the intrinsic viscosity contrast assigned to a composition value of $C = 1$. The thermal viscosity contrast $\eta_{\Delta T}$ describes the maximum potential viscosity variations due to temperature in the lower mantle and is varied in the range 2.3 to 55000, while we vary η_C between 1 and 100.

Table II.1: Characteristic parameters for thermochemical calculations. For the conversion of excess densities into B (Equation (II.3)), we assume a temperature drop across the mantle of 3300 K, which includes both the 2300 K superadiabatic temperature drop that we have in our models with Boussinesq approximation, and an adiabatic temperature increase of 1000 K. Furthermore, although our model has a constant value of $\alpha = 3.0 \cdot 10^{-5}$ for the whole mantle, we use a thermal expansivity of $\alpha = 1.0 \cdot 10^{-5}$ at the CMB for conversion to B since it is more realistic for CMB conditions (Tackley, 2012). This results in a buoyancy number comparable to previous studies (e.g., McNamara & Zhong, 2004; Mulyukova et al., 2015; Heyn et al., 2018). Ra is also calculated using the full temperature drop of 3300 K to make it comparable to previus studies and has a value of 10^7 from the parameters below. ASPECT uses thermal conductivity k and specific heat capacity c_P instead of thermal diffusvity κ, but the latter can be calculated via $\kappa = \frac{k}{\rho c_P}$ and equals $1.0 \cdot 10^{-6}$ [m^2/s].

Parameter	Symbol	Value [Unit]
Gravitational acceleration	g	9.81 [m/s^2]
Mantle thickness	d	2890 [km]
Reference density	ρ	3340 [kg/m^3]
Reference viscosity	η	$7.83 \cdot 10^{21}$ [Pa·s]
Thermal conductivity	k	4.01 [W/K·m]
Specific heat	c_P	1200 [kg·m^2/(K·s^2)]
Thermal expansivity	α	$3.0 \cdot 10^{-5}$ [1/K]
Chemical excess density	$\Delta\rho_C$	$198.396 - 330.66$ [kg/m^3]
Buoyancy ratio (eq. (II.3))	B	$0.6 - 1.0$ [ ]
Rayleigh number	Ra	10^7 [ ]
Internal heating rate	H	$9.46 \cdot 10^{-13}$ [W/kg]
Imposed surface velocity	v_{surf}	0.74-2.96 [cm/yr]
Compositional viscosity contrast	η_C	$1 - 20$ [ ]
Thermal viscosity contrast	$\eta_{\Delta T}$	$2.3 - 55000$ [ ]
Temperature drop across mantle	ΔT	2300 [K]

Table II.2: Parameters defining the viscosity profiles according to the thermal viscosity contrast $\eta_{\Delta T}$. Steps for the activation energy E_η, the temperature offset T_η and the viscosity prefactor η_0 are set at depths of 299 km (lithosphere-asthenosphere boundary), 410 km (upper mantle - transition zone) and 660 km (transition zone - lower mantle). Values are sorted by increasing depth.

$\eta_{\Delta T}$	η_0				E_η				T_η			
2.3	5 /	0.5 /	2.5 /	5	1 /	1 /	1 /	1	0.02 /	0.4 /	0.6 /	0.7
65	5 /	0.5 /	2.5 /	5	1 /	1 /	1 /	1	0.02 /	0.2 /	0.2 /	0.2
330	5 /	0.5 /	2.5 /	5	1 /	1 /	1 /	1	0.02 /	0.15 /	0.15 /	0.15
1700	5 /	0.5 /	2.5 /	5	1 /	1 /	1 /	1	0.02 /	0.12 /	0.12 /	0.12
7500	5 /	0.5 /	2.5 /	5	1.2 /	1.2 /	1.2 /	1.2	0.02 /	0.12 /	0.12 /	0.12
55000	5 /	0.5 /	2.5 /	5	1.2 /	1.2 /	1.2 /	1.2	0.02 /	0.1 /	0.1 /	0.1

All models are initiated from the same reference state of a fully-developed system with an existing degree-2 structure (see Figures II.2a and II.2b). This is obtained by running a model with the reference values of $B = 0.8$, $\eta_{\Delta T} = 330$ and $\eta_C = 10$ for 6.5 Gyr (corresponding to t_0 in Equation (II.2)) starting at $t = 0$ with a 125 km thick dense basal layer (as described in Heyn et al. (2018)). This setup results in a pile with a volume equal to about 1.75 % of the mantle at $t = t_0$. Approximately 77% of the original material remains in the pile of the reference state. Although such a setup means that models can take some time to adjust to changes in parameters (especially a change in the velocity boundary condition as shown below), it enables us to directly compare results and analyse dependences on various parameters without having to worry about variations in pile mass retained after 4.5 Gyr of convection (see Heyn et al. (2018) for more details about how much mass changes with $\eta_{\Delta T}$ and η_C). Moreover, it allows us to estimate the time that the system takes to adjust to new conditions, such as changes in plate velocity during a supercontinent cycle (e.g., Matthews et al., 2016). To overcome the limitation of adjustment time and to get better constraints on plume properties, we run the models for 2.5 Gyr in order to examine several plumes rising from the same location.

II.2.2 Detection of plumes

We detect plumes by calculating profiles of temperature and radial velocity versus longitude at a specific radius and tracking their maxima. An example of such a profile for temperature is shown in Figure II.2c. The innermost white circle segment across the temperature field (Figure II.2b) indicates the profile radius of 4000 km (519 km above the CMB), along which the temperature shown in Figure II.2c is projected. As can be seen in Figure II.2a, a radius of 4000 km is just above the top of the thermochemical pile for this set of parameters. A profile closer to the CMB would partly cut through the pile, which makes the detection and interpretation of plumes significantly less reliable. However, actual pile thickness varies with parameters, especially the density contrast (e.g., McNamara & Zhong, 2004; Heyn et al., 2018). Consequently, we choose radii of

4000 km, 4200 km or 4500 km (correspodning to 519 km, 719 km and 1019 km above the CMB, respectively) for our analysis, depending on the thickness of the pile. The horizontal black line in Figure II.2c indicates the cross-sectional length of CMB that is covered by the thermochemical pile at the given time step, while the maxima marked by arrows identify plumes. The excess temperature (or radial velocity) for each time step is then obtained by calculating the difference
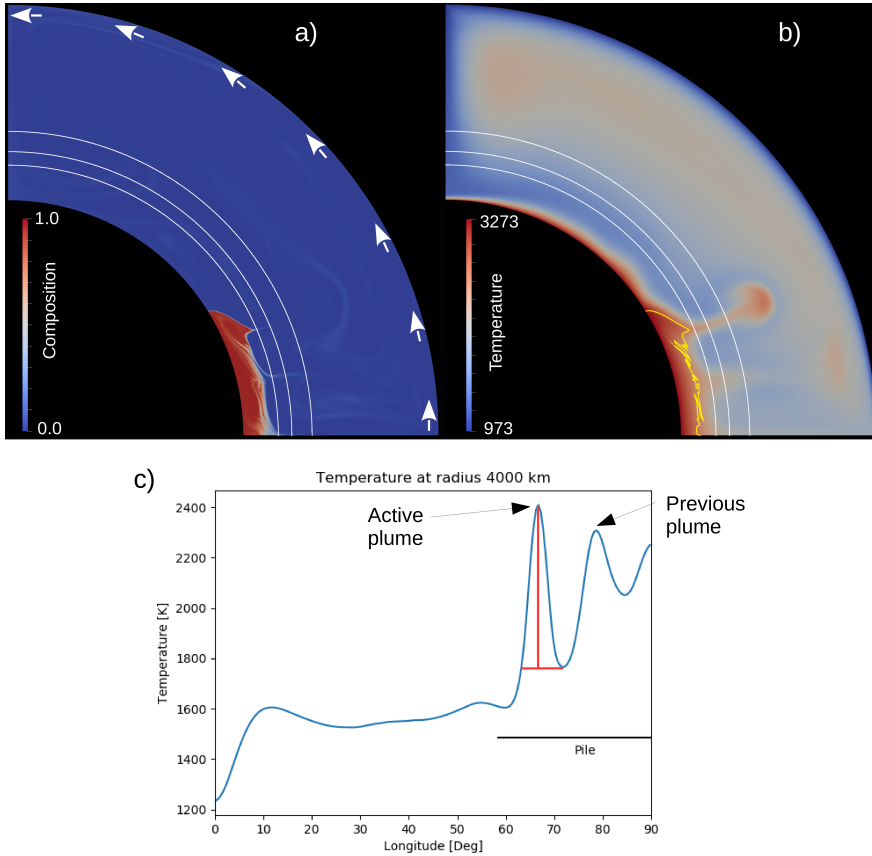

Figure II.2: Initial condition for (a) composition field and (b) temperature field, with radii of 4000 km, 4200 km and 4500 km marked as white lines. Profiles along these radii are used to identify and investigate plumes. White arrows in (a) indicate the imposed plate velocity, while the yellow line in (b) marks the outline of the dense pile for a countour line of composition at $C = 0.8$. (c) An example of a temperature profile along the radius of 4000 km for the initial condition shown in (b). Identified plumes are marked with black arrows. The width and the excess temperature we obtain are marked with red lines for one of the plumes. The black horizontal line indicates the part of the CMB that is covered by the pile.

between the maximum and the highest minimum next to this maximum (as indicated by the vertical red line in Figure II.2c). The width of the plume is defined as the width of the peak taken at the value of the minimum used to obtain the amplitude (see red horizontal line in Figure II.2c).

We are mostly interested in plumes around the pile edges, and in fact all plumes in our models are either generated there or on the CMB outside the piles and then pushed towards the pile edge. Thus, in this study, we only track the maxima of temperature and radial velocity within a range of 10 degrees from the edge outside of the pile and 15 degrees from the edge towards the pile centre. This choice usually avoids complexities in plume detection associated with the general upwelling above the pile centre. The maxima are tracked over time from their appearance (either marked by the beginning of the thermal instability or by the motion of the pile into the respective lateral range around the pile edge) until they disappear (plume fades or moves out of range towards the pile centre). For each plume, we calculate the maximum excess temperature and excess velocity, which usually marks the passing of the plume head through the respective radius. When appropriate, we calculate averages of plume properties to even out natural variations that are not related to changes in parameters.

II.3   Mechanism of plume generation

As pointed out by M. Li et al. (2018), a thermochemical pile can respond to a rising plume by being uplifted. However, their models feature plumes rising from the centre of tent-shaped piles, while our models predict plumes rising from pile margins with localized interaction between plume and pile. Figure II.3 shows the temporal evolution of this interplay as a zoom-in on the pile edge. As can be seen in the temperature field, the plume that is visible in the first stage (Figure II.3a) is slowly pushed further towards the centre of the pile by the general flow along the CMB (Figure II.3b). During this process, hot pile material is lifted up by the plume, which increases the local pile thickness and reduces the CMB area that is covered by the pile (indicated by pile outlines), resulting in a steepening of the pile margin. When the plume moves further towards the pile centre (Figure II.3c), the position of the maximum thickness moves along with the upward pull of the plume. When the plume is pushed onto the top of the pile and loses its connection to the lower thermal boundary layer, it weakens, thereby reducing the plume pull. Moreover, the plume heat extracted from the pile causes the top of the pile to cool down and increase its density. As a consequence, the pile top becomes gravitationally unstable, eventually resulting in a collapse of the thickened pile edge (Figure II.3d). Subsequently, the pile material spreads along the CMB, pushing the hot thermal boundary layer next to it against the dominant flow direction resulting from subduction (Figure II.3e). The subsequent local thickening of the hot thermal boundary layer outside the thermochemical pile marks the beginning of a new plume (Figure II.3f), which then repeats the process.
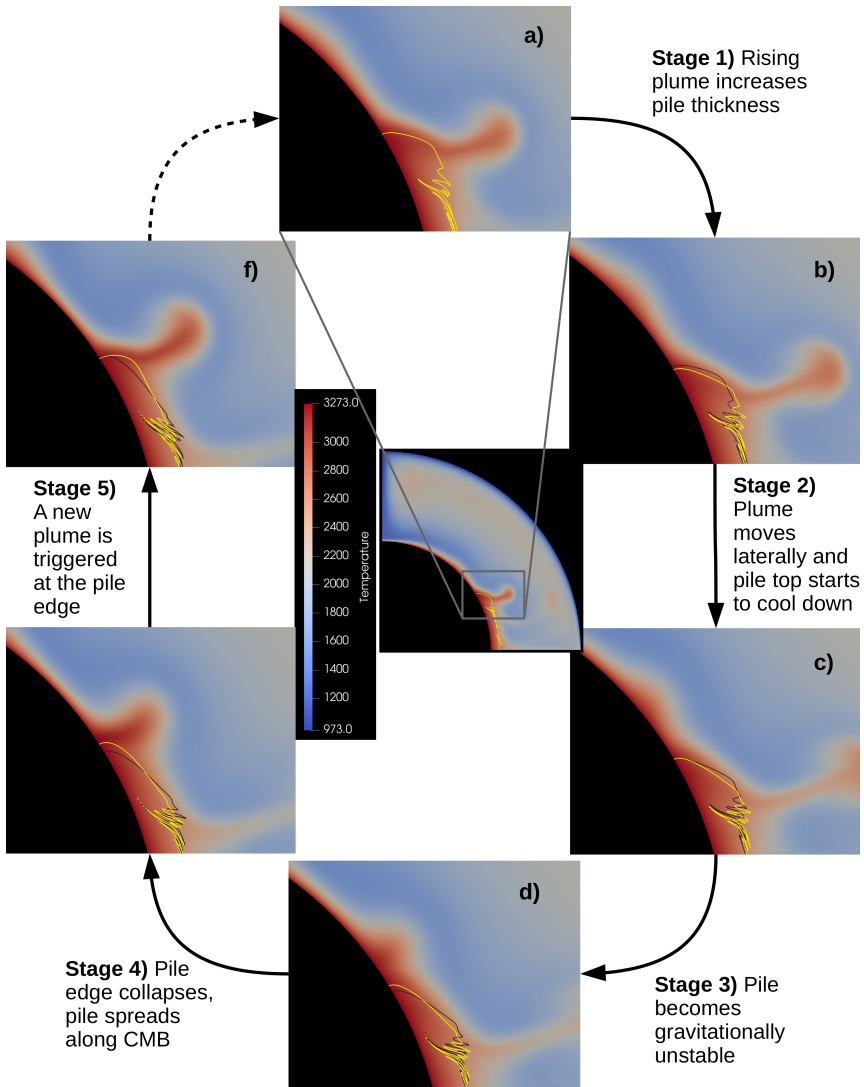
Figure II.3: Snapshots of the temperature field around the pile edge during the plume cycle for our reference model ($B = 0.8$, $\eta_C = 10$ and $\eta_{\Delta T} = 330$). Yellow lines show the outline of the dense material ($C = 0.8$) at the current time step, while grey lines indicate the shape of the pile in the previous snapshot for comparison. As can be seen, the plume increases local pile thickness and drives a pile-ward a motion of the pile edge (stages 1 and 2) until the plume can no longer support the thicker pile, which starts to collapse back towards the CMB, where it spreads against the push of the slab (stages 3 and 4). This results in a local thickening of the thermal boundary layer outside the pile, which triggers the next plume (stage 5).

The motion of the pile edge and thus the cyclicity of the plume generation can be seen in more detail in Figure II.4. Figure II.4a shows the thickness of the pile at certain distances from its edge, between 5 and 15 degrees inwards. The thickness at 5 degrees into the pile shows a periodicity of about 350-400 Myr, reflecting the plumes recorded at 719 km above the CMB about 70-120 Myr later (Figure II.4c). The same periodicity, delayed by approximately 30-40 Myr, is also visible in the lateral motion of the pile edge (Figure II.4b). This delay shows that the pile collapse starts within the pile and not is not initiated by a motion of the pile edge itself. Notice that the amplitudes of pile motion and thickness variations are not constant, but reflect amongst other aspects the strength of the individual plumes. Further into the pile, the variations in thickness become less representative of the plume cycle, with the correlation almost lost by 15 degrees away from the edge. The thickness close to the pile centre (Figure II.4d) does not resemble the plume cycle, indicating that pile thickening and collapse during the plume cycle are only localized within about 5-10 degrees from the pile edge. The rapid changes in pile thickness observed for positions close to the pile centre or more than about 10 degrees from the pile edge are related to the fact that the pile top is ususaly rather jagged (see Figure II.2a).

The results shown in this section are obtained for the reference parameters $B = 0.8$, $\eta_{\Delta T} = 330$ and $\eta_C = 10$, but we find no major change in behavior when altering any of the three parameters B, $\eta_{\Delta T}$ or η_C (Figure II.4e-g). Decreasing or increasing the bouyancy ratio B affects the temporal stability of the pile (e.g., Heyn et al., 2018) and can add complexities in case the low density results in unstable piles. Moreover, increased density results in flatter piles, and thus also reduces pile edge motion and thickness variations (see Figure II.4g). Increasing the compositional viscosity contrast η_C also reduces pile motion (Figure II.4e), with both lateral motions of the pile edge and thickness variations diminished. In contrast, increasing $\eta_{\Delta T}$ has little effect and only slightly increases pile motion (Figure II.4f). However, the mechanism for plume-pile interaction and the correlation between the plume cycle and pile motion are not affected by the choice of these parameters.

II.4   Plume periodicty

The plume period observed in the models above evolves naturally from the given set of parameters. Yet, the actual period with which plumes form at the pile edge varies significantly for different choices of parameters. Moreover, some models show no plumes forming away from the pile edge, while others have many plumes that form without responding to pile edge motion. In the following section, we will explore the controls on the "natural" period of plume formation, and how it can be overprinted by the influence of mantle convection.
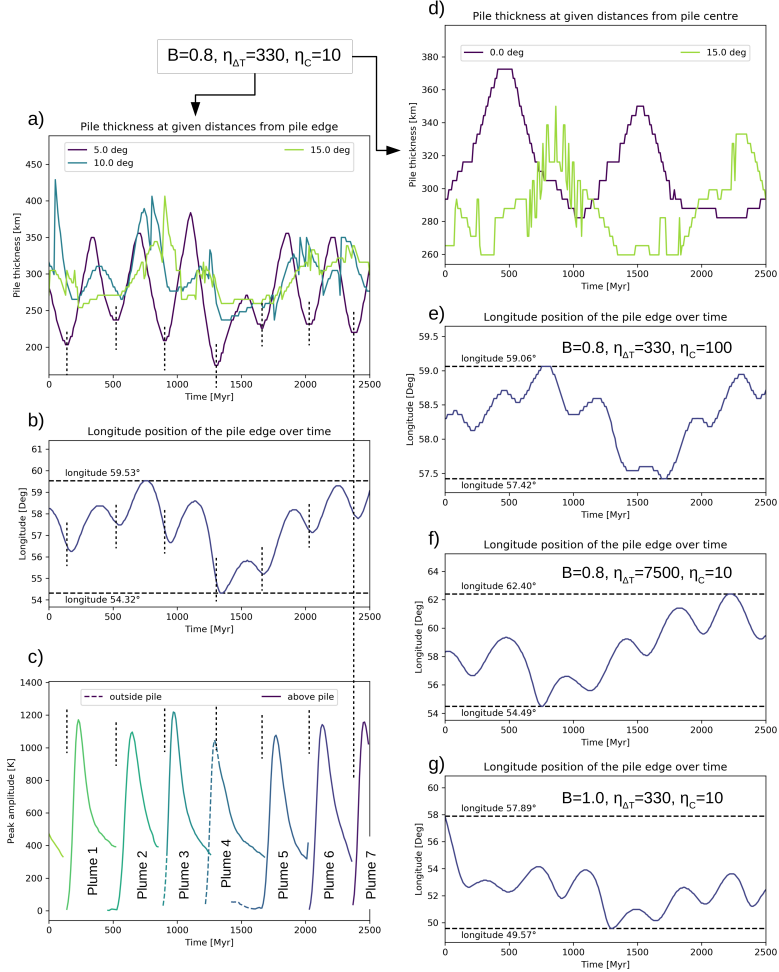
Figure II.4: The plume cycle for our reference model with $B = 0.8$, $\eta_C = 10$ and $\eta_{\Delta T} = 330$ and a constant plate velocity of $1.48\,\mathrm{cm/year}$ can be identified in variations of pile thickness inwards from the pile edge, especially at 5 degrees inwards (a), the lateral motion of the pile edge (b) and the excess temperature of upwellings at a radius of $4200\,\mathrm{km}$ (c). As can be seen by the black dotted lines, every minimum in pile thickness and edge longitude corresponds to a plume in (c), although there is a small time difference between the three graphs that represents a delay in reaction between pile and plume. In contrast, the plume cycle is not represented in pile thickness close to the pile centre (d). Sharp changes in pile thickness (especially observed for the pile centre) are related to the ragged top of the pile (see Figure II.2). (e)-(g) show the motions of the pile edge for models with increased compositional viscosity contrast (e), increased thermal viscosity contrast (f) and increased density (g), but otherwise the same parameters as the reference model. Note the change in the longitude range of lateral pile edge motion associated with the changed parameters.

II.4.1 The two "natural" plume periods

II.4.1.1 Thermal boundary layer period $\mathcal{T}_{\mathrm{TBL}}$

Plumes in a basally-heated convection model without a dense component form as thermal instabilities of the lower thermal boundary layer (TBL). When the TBL grows in thickness due to heat conduction, it can reach a thickness for which the local Rayleigh number Ra_l is above a critical value, and an instability forms (Deschamps & Tackley, 2008; M. Li & Zhong, 2017). How often such instabilities form, i.e. the "natural" plume period of the lower TBL ($\mathcal{T}_{\mathrm{TBL}}$), is determined by the parameters that affect Ra_l, mainly the thermal expansivity α, the thermal diffusivity κ and the viscosity η (M. Li & Zhong, 2017), of which the viscosity is the most poorly constrained (Tackley, 2012). A lower value of Ra_l, for example due to higher viscosity or thermal diffusivity or a lower thermal expansivity, reduces the number of plumes forming in time (M. Li & Zhong, 2017). Thus, $\mathcal{T}_{\mathrm{TBL}}$ is fundamental to Ra_l and independent of the pile properties.

The plume initiation process outlined above is restricted to the TBL outside the thermochemcial pile areas. Since the TBL grows everywhere, with additional thickening caused by lateral flow along the CMB, plume generation is not necessarily limited to the pile margins. Thus, depending on the parameters, we might expect to see a certain percentage of plumes forming (far) away from the pile (M. Li & Zhong, 2017). In fact, some of our models, especially those with reduced plate velocity and therefore reduced lateral TBL flow, show plumes forming away from the pile edge as discussed below. M. Li and Zhong (2017) have shown that a reduction of the local Rayleigh number Ra_l reduces the number of plumes forming (far) away from the pile, yet neither thermal expansivity α nor diffusivity κ are changed within our models, and our viscosity law (Section II.2.1) does not change the viscosity of the hot lower TBL significantly with $\eta_{\Delta T}$. Viscosity above the TBL is affected by $\eta_{\Delta T}$, but does not impact plume initiation. Consqeuently, variations in Ra_l alone can only explain minor variations in the number of initiated plumes and should not cause a periodic signal at the pile edges.

II.4.1.2 Slab-pile period $\mathcal{T}_{\mathrm{Pile}}$

As pointed out above, plumes at the pile margin are initiated by a periodic pile collapse with period $\mathcal{T}_{\mathrm{Pile}}$, which provides the necessary local thickening of the lower TBL. This process is to first order independent of Ra_l, since it responds to how fast plumes lose their ability to support a thicker pile. However, it depends on plate velocity (see next section) and plume strength, the latter reflecting how often and how effectively plumes reduce the TBL thickness (see also section Section II.5). Figure II.5a shows the period of plumes versus the compositional viscosity contrast η_C for all tested values of the temperature-dependence of viscosity $\eta_{\Delta T}$. As can be seen, each value of $\eta_{\Delta T}$ has its own characteristic

period with considerably larger differences than we would expect from variations in the local Rayleigh number, while intrinsic pile viscosity contrast η_C (Figure II.5a) or the excess density of the pile (B) play minor roles (Figure II.5b).
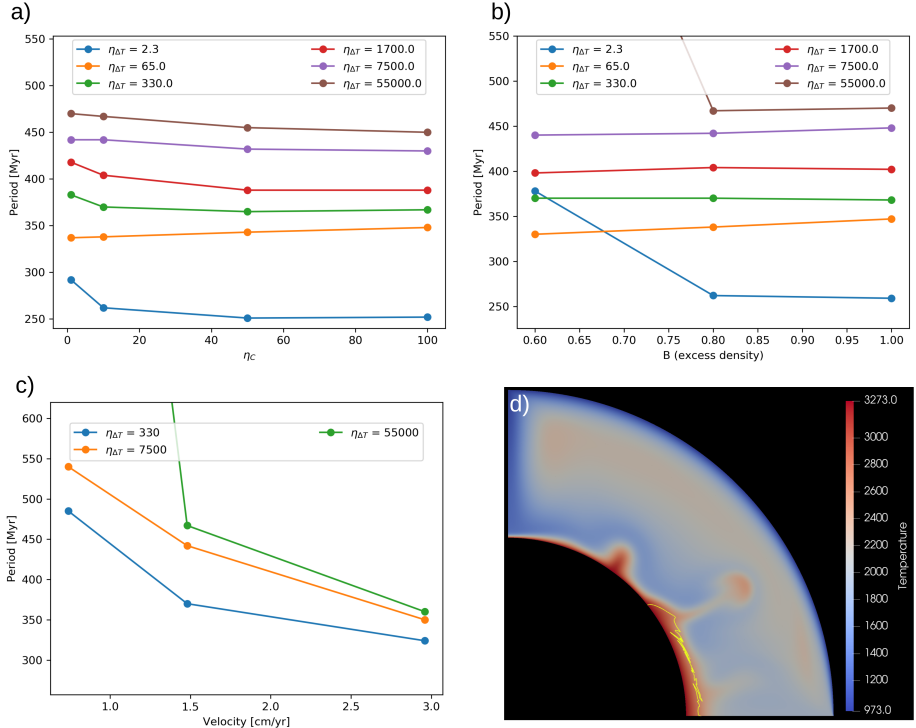

Figure II.5: The period of the plume cycle for a plate velocity of $v_{\mathrm{surf}} = 1.48\,\mathrm{cm/year}$ as a function of (a) the compositional viscosity contrast η_C for $B = 0.8$, (b) the density contrast B for $\eta_C = 10$ and (c) the plate velocity for $B = 0.8$ and $\eta_C = 10$. Models with different thermal viscosity contrasts $\eta_{\Delta T}$ are marked by the color of the line. Outliers in (b) and (c) for $\eta_{\Delta T} = 55000$ and the lowest density or velocity, respectively, fall outside the plotted area. As can be seen, neither η_C nor B have a strong effect on the period, while models with different $\eta_{\Delta T}$ are clearly separated from each other. The period of plumes increases significantly with increasing $\eta_{\Delta T}$. In additon, the period is strongly affected by the plate velocity. Especially for low velocities, plumes may also form independently of the the pile collapse, for example as in (d) with $B = 0.8$, $\eta_C = 10$, $\eta_{\Delta T} = 55000$ and a velocity of $0.74\,\mathrm{cm/year}$. In this case, plumes initiated away from the pile tend to merge with those starting at the pile, making it difficult to determine plume characteristics such as the period shown in (c).

The reason that none of the actual pile properties (B or η_C) affect the plume period relates to the connection between the plume and the TBL. As long as growing plumes are located directly above the pile margin and are fed by a continuous supply of hot TBL material, their lower parts are able to maintain high temperatures, while the plume buoyancy provides upward pull on the pile margin. When the lateral flow (mantle wind) pushes the plume roots towards the pile centre, the supply of hot TBL material declines and plumes begin to weaken at their base since the pile material itself is too dense to provide sufficient influx. As a consequence, and due to the fact that the plume continues to move above the pile, the thickened pile edge contacts directly with the colder ambient mantle and cools down more efficiently by conduction. Pile collapse is then triggered by the combination of pile cooling, reduced plume pull and the lateral motion of the plume. Therefore, the strength of the mantle wind close to the CMB, which is the same as the velocity of the slab material spreading along the CMB (v_{CMB}), controls the period of pile collapse. This spreading velocity is related to the rate at which cold material is supplied to the lowermost mantle and thus to the sinking velocity of slabs in the lower mantle. Since increasing $\eta_{\Delta T}$ increases the effective viscosity of the slab, both sinking and CMB spreading velocity are reduced and plumes are generated less frequently. The plate velocity has an even stronger effect on slab sinking velocity, as will be discussed in the next section, but the results shown in Figure II.5a and Figure II.5b are obtained for the same plate velocity. Thus, v_{CMB} determines the plume period of the slab-pile system $\mathcal{T}_{\mathrm{Pile}}$.

II.4.1.3 Observed period

The effective period of plume initiation at the CMB is a combination of the two processes. If the "natural" plume period of the lower TBL is longer than the period given by the slab-pile system, i.e. $\mathcal{T}_{\mathrm{TBL}} > \mathcal{T}_{\mathrm{Pile}}$, plumes will be predominantely initiated near an outwards extending pile edge associated with pile collapse. Otherwise ($\mathcal{T}_{\mathrm{TBL}} < \mathcal{T}_{\mathrm{Pile}}$), most of the plumes will be generated away from the pile (see Figure II.5d), and subsequently pushed towards the pile where it may interact and merge with other plumes.

Independent of plume initiation away from the pile, the pile collapse caused by the fading of the previous plume creates a thermal instability, which starts to rise at the pile margin. In most cases, however, plumes forming outside the pile and at the pile margin will simultaneously coexist only for a short while before they merge. A similar process of plume merging can be observed if the temporal spacing between plumes gets small, e.g. for large plate velocities. In these cases, our plume detection algorithm may identify them as a single plume with pulsating flux, making the determination of plume properties (e.g. period, lifetime) more difficult (see e.g., outliers for $B = 0.6$ in Figure II.5b and the lowest velocity in Figure II.5c).

II.4.2   The effect of plate velocity on plume period

II.4.2.1   Constant plate velocity

The observed plume period is furthermore altered by the plate velocity (Figure II.5c), which affects the slab sinking rate in the lower mantle and the lateral TBL flow (mantle wind). A higher plate velocity therefore results in more slab material at the CMB and more frequent plume generation at the pile margin. A reduced plate velocity has the opposite effect, creating less frequent plumes, most of which initiate away from the pile (Figure II.5d). In both cases, the lower mantle reacts rapidly (within a few tens of Myr) to the modified plate velocity, although the change in plume excess temperature and plume period gets more pronounced after aproximately 50-100 Myr. Changes in plate velocity have a stronger effect on slab sinking velocity, and thus plume period, than changes in the thermal viscosity contrast $\eta_{\Delta T}$. The excess temperature of plumes in models with a high plate velocity is significantly smaller since the lower TBL has less time to heat up and grow between plumes.

II.4.2.2   Periodic plate velocity

More interesting than the effect of a constant velocity is the impact of time-variable plate motion. To test this, we have prescribed velocity v_{Plate} as cosine function in time (Equation (II.2)) with different periods, ranging from 125 Myr to 1 Gyr. This simulates changes in plate velocities during a supercontinent cycle (Matthews et al., 2016). As can be seen in Figure II.6, the plume cycle can adjust to the velocity period within a certain resonance range around $\mathcal{T}_{\mathrm{Pile}}$. While an imposed plate velocity with a period of 250 Myr for our model with $B = 0.8$, $\eta_{\Delta T} = 330$ and $\eta_C = 10$ forces the plume cycle to follow a similar period after an adjustment time of about 1 Gyr (Figure II.6a-d), a higher plate velocity period of 125 Myr cannot be enforced for the plume cycle (Figure II.6e-h). The reason for this can be seen from the motion of the pile edges (Figure II.6c and Figure II.6g) and the variation of pile thickness at 5 degrees from the pile edge (Figure II.6d and Figure II.6h). While the pile edge motion in both cases reflects the plate velocity cycle and thus the strength of lateral TBL flow (Figure II.6c and Figure II.6g), the thickness of the pile as the driving mechanism for plume generation only reflects the plume cycle (compare Figure II.6b and Figure II.6f with Figure II.6d and Figure II.6h). In fact, for plate velocity periods below the lower limit of a certain resonance range, in this case between 250 Myr and 125 Myr, plume motion and the pile react as if the velocity were constant (compare Figure II.6h and Figure II.4a). In these cases, the lateral motion of the pile edge is the superposition of the motion caused by the variable plate velocity and pile collapse (Figure II.6g).
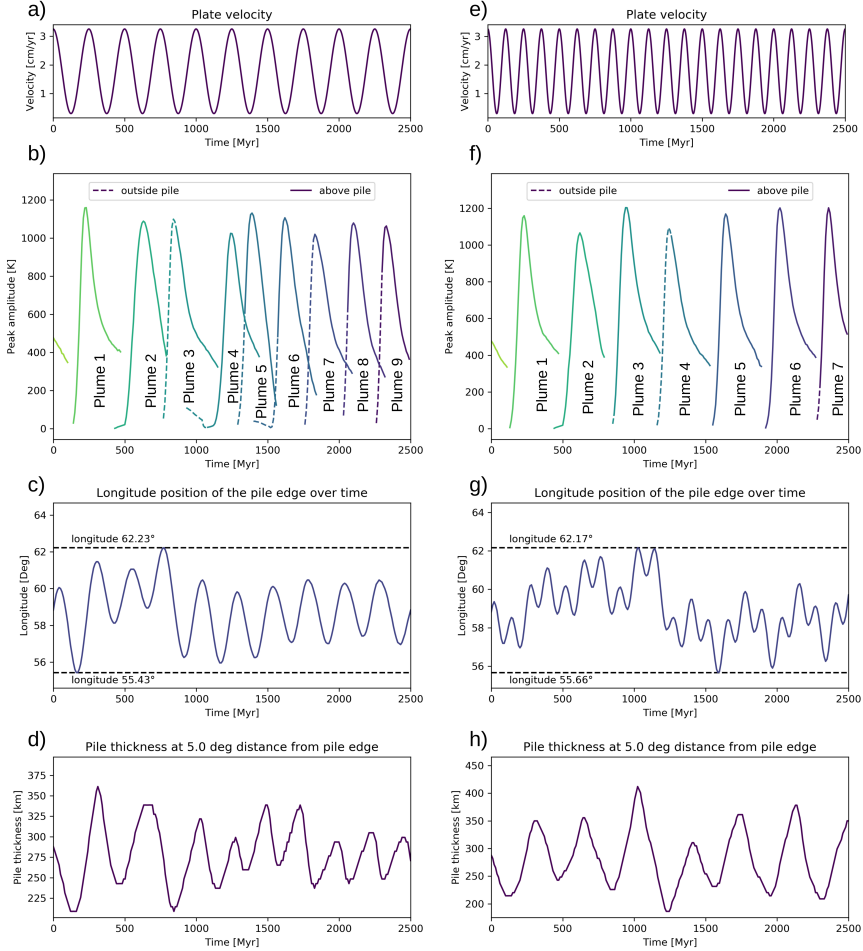
Figure II.6: Representative characteristics of the plume cycle for models with $B = 0.8$, $\eta_C = 10$ and $\eta_{\Delta T} = 330$ and a periodic velocity boundary condition of $\mathcal{T}_{\text{Plate}} = 250 \, \text{Myr}$ (left) and $\mathcal{T}_{\text{Plate}} = 125 \, \text{Myr}$ (right). The top panels (a) and (e) indicate the plate velocity as reference, while panels (b) and (f) in the second row show the excess temperature of identified plumes at $4200 \, \text{km}$ radius. The third row with panels (c) and (g) and the lower panels (d) and (h) illustrate the motion of the pile edge and the variation in pile thickness at a distance of 5 degrees inwards from the pile edge, respectively. As can be seen, both lateral pile edge motion and pile thickness reflect the plume cycle for $\mathcal{T}_{\text{Plate}} = 250 \, \text{Myr}$ plate velocity period after an adjustment time of about $1 \, \text{Gyr}$, while the plume period cannot adjust to a period of $\mathcal{T}_{\text{Plate}} = 125 \, \text{Myr}$. Neither the plumes in (f) nor the pile thickness in (h) follow a $125 \, \text{Myr}$ cycle, which is represented in the short-wavelength variations of the pile edge postion (g). In contrast, the plume cycle has about the same period of $370 \, \text{Myr}$ as for a constant velocity of $1.48 \, \text{cm/year}$ (Figure II.4b).

A similar observation can be made for very long cycles of $1\,\mathrm{Gyr}$ (not shown), although more plumes start away from the pile during times of low plate velocity and the plume cycle becomes aperiodic to a certain extent. Thus, plate velocity cycles are only reflected in plume periods if they are within the resonance range of the slab-pile system, which depends on $\mathcal{T}_{\mathrm{Pile}}$. Within that range, the system adjusts such that every plate cycle corresponds to a plume ($\mathcal{T}_{\mathrm{Pile}} = \mathcal{T}_{\mathrm{Plate}}$). For shorter plate velocity periods, the observed plume period $\mathcal{T}_{\mathrm{Pile}}$ reflects the constant average of velocity. For longer plate periods, the observed plume period becomes more chaotic due to plumes forming far away from the pile. Yet, the push from lateral TBL flow on the pile margin still reflects plate velocity cycles, even for high or low periods. As a consequence, the lateral motion of the pile edge in these cases reflects both the plate velocity period and the plume cycle as a superposition of the two periods, while the pile thickness only captures the plume cycle. In case of our reference model, the reference period of the slab-pile system $\mathcal{T}_{\mathrm{Pile}}$ is about $370\,\mathrm{Myr}$, and the lower and upper limits of the resonance range are somewhere between 125 and $250\,\mathrm{Myr}$ and between 500 and $1000\,\mathrm{Myr}$, respectively, since neither $125\,\mathrm{Myr}$ nor $1\,\mathrm{Gyr}$ periods can be stimulated while plume periods at 250 and $500\,\mathrm{Myr}$ can be. A higher value of $\eta_{\Delta T}$, or a lower average velocity, should move the resonance range towards longer plume periods (Figure II.5).

II.5 Plume buoyancy flux and lifetime

A change in plume period is reflected in other properties of the plumes, for example their excess temperature. While a system with $\mathcal{T}_{\mathrm{TBL}} < \mathcal{T}_{\mathrm{Pile}}$ is characterised by a large number of plumes forming independently of pile collapse, we expect the case $\mathcal{T}_{\mathrm{TBL}} > \mathcal{T}_{\mathrm{Pile}}$ to be reflected in weaker plume strength as the TBL has insufficient time to grow thick enough to form instabilities naturally. Figure II.7a shows the excess temperature of detected plumes for a model with the same parameters as our reference model, except that the velocity has been increased to $2.96\,\mathrm{cm/year}$. While the radius at which these temperatures is taken is lower (at $519\,\mathrm{km}$ above the CMB instead of $719\,\mathrm{km}$ as weaker plumes are more difficult to detect and fade away more easily), which precludes a direct comparison to Figure II.4c, the first plume in Figure II.7a has not been affected significantly by the increased velocity because it falls within the adjustment time of the model after modifying the velocity. As a consequence, it can be used as a reference to which later plumes can be compared.

In order to compare plumes between the different models, we calculate the averages of buoyancy flux (Figure II.7b and Figure II.7d) and lifetime (Figure II.7c) for all plumes detected during the simulation time. Our definition of lifetime reflects the time that each plume stays within the given lateral distance range around the pile edge. The buoyancy flux, neglecting small amounts of dense material entrained in the plume, is calculated according to the formula $B = \int v_{\mathrm{r}} \rho \alpha \Delta T_{\mathrm{P}} dS$ with the plume excess temperature ΔT_{P} and radial

velocity v_r (e.g., Dannberg & Sobolev, 2015; Farnetani et al., 2018), assuming a rotational symmetry around the central plume axis to obtain 3-D buoyancy fluxes. Buoyancy flux is a good measure of plume strength since it combines both excess temperature and radial velocity and integrates over the width of the plume (Dannberg & Sobolev, 2015; Farnetani et al., 2018). However, determinations of lifetime and buoyancy flux get more complicated for plumes that merge together.
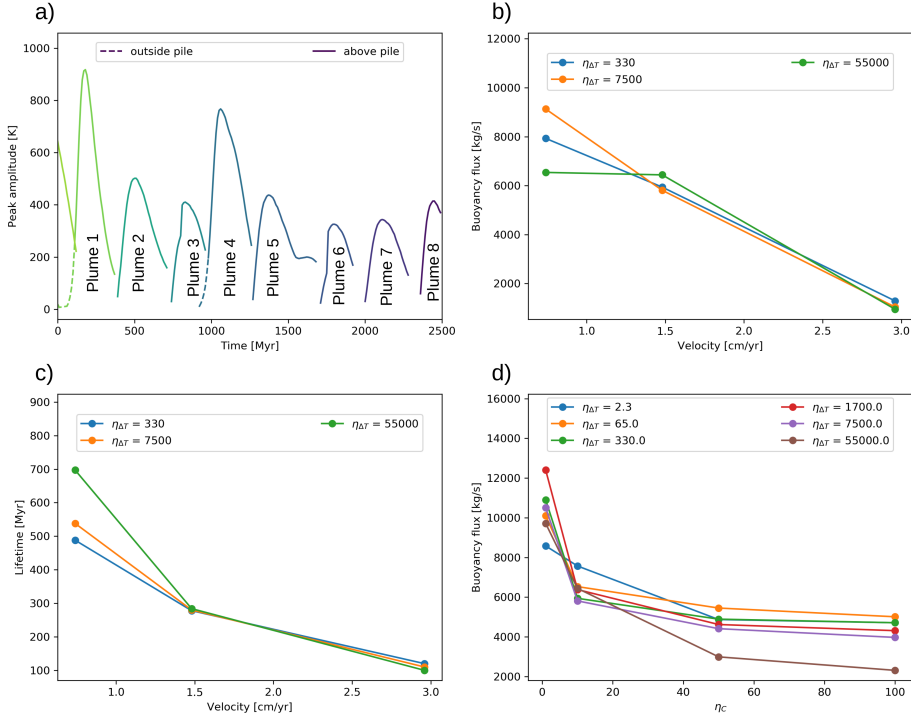

Figure II.7: (a) Excess temperature of identified plumes at radius 4000 km for a model with $B = 0.8$, $\eta_C = 10$ and $\eta_{\Delta T} = 330$ and a constant plate velocity of 2.96 cm/year (increased compared to our reference model). Increased velocity not only reduces the excess temperature of plumes (compare (a) and Figure II.4c), but also reduces plume lifetime (c) and buoyancy flux (b). Since the thermal boundary layer has less time to grow for a stronger TBL flow, plumes are weaker. This effect is independent of other parameters such as the temperature dependence $\eta_{\Delta T}$. (d) shows the buoyancy flux as a function of compositional viscosity contrast η_C for different values of thermal viscosity contrasts $\eta_{\Delta T}$. While there is no consistent variation of buoyancy flux with $\eta_{\Delta T}$, entrained dense material with higher η_C reduces the buoyancy flux by increasing the average plume viscosity. A similar reduction in buoyancy flux can also be observed for increased pile density B (not shown here).

II.5.1 Effect of velocity

As can be expected, the lifetime of plumes decreases with increasing plate velocity (see Figure II.7c). The reason is that plumes are more easily pushed out of the range around the pile margin (and thus out of the area where we track them), but they also lose their connection to the hot TBL and therefore fade away more quickly. Moreover, plumes created under high plate velocities are weaker (low buoyancy flux at their onset, Figure II.7b), because the thermal boundary layer has less time to grow and plumes contain less material. Thus forcing plumes to adopt to a shorter period than the "natural" period results in overall weaker plumes that are less enduring.

A similar observation can also be made for periodic plate velocities. The shortest plate velocity period $\mathcal{T}_{\text{Plate}}$ within the resonance range forces the highest number of plumes, and thus the weakest plumes (compare Figure II.6 second row panels), although the difference in plume excess temperature is only about $200\,\text{K}$. Shorter or longer plate velocity periods result in less frequent, but stronger plumes since the TBL has more time to grow. Plume lifetimes are more complicated to interpret, since the mantle wind v_{CMB} changes significantly with time. Within the resonance range, lifetimes increase with longer $\mathcal{T}_{\text{Plate}}$ as maxima in v_{CMB} are less frequent. Outside the resonance range, lifetimes either adjust to the constant average velocity ($\mathcal{T}_{\text{Plate}} <$ resonance range), or become more chaotic and less reliable due to plume formation away from the pile ($\mathcal{T}_{\text{Plate}} >$ resonance range).

II.5.2 Effect of viscosity and pile density

In contrast to changing the plate velocity, a change in the temperature dependence $\eta_{\Delta T}$ alters the plume period (Figure II.5a), but the effect on plume lifetime or buoyancy flux is negligible (see different colors in Figures II.7b-d). A higher value of $\eta_{\Delta T}$ slightly reduces the lateral CMB flow v_{CMB}, which decreases lateral plume motion and TBL thickening due to TBL flow. Yet, the system stays relatively close to the natural plume period of the lower TBL ($\mathcal{T}_{\text{TBL}} \approx \mathcal{T}_{\text{Pile}}$), causing only minor variations in plume strength. Since plumes stay longer around the pile margin, they can increase pile edge thickness more, which also increases the lateral mobility of the pile edge during plume cycles (compare Figures II.4b and II.4f). Thus, during a pile collapse, the pile margin moves faster and further, locally increasing the TBL thickness within a short time. Consequently, plumes, triggered either by the pile collapse or initiated away from the pile, abruptly enter or leave the range around the pile margin, reducing their detected lifetimes around the pile margin.

Increasing the density or the compositional viscosity contrast tends to decrease plume buoyancy flux (compare Figure II.7d), since a higher density or viscosity of the entrained material slows plume ascent. Yet, in contrast to the effect of plate velocity, a reduction in plume flux is not represented in the excess

temperature of plumes because the lower thermal boundary layer has enough time to grow. As the entrained material increases the average plume density or viscosity relative to the ambient mantle, this effect is more or less independent of the temperature-dependence of the viscosity.

In summary, both bouyancy flux and lifetime (or residence time around the pile edge) of plumes are mostly affected by plate velocity, while other parameters play minor roles. In particular, if plate velocity forces plumes at considerably shorter period than $\mathcal{T}_{\mathrm{TBL}}$ (the natural period of the lower thermal boundary layer), this is reflected in significant reduction in buoyancy flux and lifetime. Consequently, buoyancy flux and the number of plumes away from the pile give indications how close the system is to $\mathcal{T}_{\mathrm{TBL}}$. A large number of plumes forming (far) away from the pile edges indicate $\mathcal{T}_{\mathrm{TBL}} < \mathcal{T}_{\mathrm{Pile}}$, while a low buoyancy flux means $\mathcal{T}_{\mathrm{TBL}} > \mathcal{T}_{\mathrm{Pile}}$.

II.6 Discussion

II.6.1 Model limitations

As shown above, plumes are initiated at the CMB when the thickness of the lower thermal boundary layer reaches a critical value, which is defined by the local Rayleigh number Ra_l (Deschamps & Tackley, 2008; M. Li & Zhong, 2017). The boundary layer grows conductively over time, with additional thickening due slab-induced lateral flow along the CMB, causing spontaneous thermal instabilities. This plume generation mechanism is independent of the presence or properties of a thermochemical pile and does not predict where the plume will be initiated. Plume generation is generally suppressed by a decrease in thermal expansivity or an increase in conductivity towards the CMB, which are expected for Earth (Tackley, 2012) and would reduce Ra_l (M. Li & Zhong, 2017). A decrease in viscosity, e.g. due to the presence of weak post-bridgmanite (Ammann et al., 2010; Koelemeijer et al., 2018) as discussed below, may offset this effect. Yet, a pile may trigger "early" plume formation by providing a localized thickening of the TBL due to an expanding pile margin associated with a pile collapse, with "early" being relative to the time frame set by conductive growth of the TBL, $\mathcal{T}_{\mathrm{TBL}}$. This "early" plume initiation always results in plumes forming at the pile margin and, depending on parameters such as viscosity or plate velocity, may be the dominant mechanism.

In our 2-D models, both types of plumes may eventually end up rising at the same location of the pile margin, giving a periodic behavior of plume generation. In 3-D, however, this does not necessarily hold true any longer. We cannot expect plumes to rise at exactly the same location since a collapsing pile edge would increase the thickness of the lower TBL in an area around it, and plumes would draw in material from within a certain radius. These 3-D effects should

tend to make plume initiation less periodic in global models as plumes may rise from several different locations around the piles.

Apart from being 2-D, our models are simplified with respect to subduction processes. As we have no weakening due to yield stress, plates and subduction zones are not forming self-consistently, but are forced by an imposed velocity boundary condition. Furthermore, our models feature neither phase transitions in the mantle transition zone (although we do impose a viscosity jump at 410 km and 660 km) potentially causing slab stagnation, nor subduction zone retreat or advance. As a consequence, we obtain a stable degree-2 convection pattern and a coherent slab penetrating into the lowermost mantle. While these simplifications allow us to have more direct control over the lateral velocities within the lower TBL, we do not expect them to have a significant impact on plume initiation dynamics as this process is localized in the lowermost mantle and is not affected by the details of subduction dynamics in the upper mantle. The only way that slabs play a significant role for plume-pile dynamics is via their impact on the lateral TBL flow along the CMB (v_{CMB}), which may be strongly dependent on 3-D effects. The effect of changes in subduction velocity are simulated by modifying the imposed velocity boundary condition, while changes in TBL flow direction would require a 3-D geometry.

The viscosity structure of the lowermost mantle might be further modified by the presence of weak post-bridgmanite (or post-perovskite) (Ammann et al., 2010), although it is not clear whether this phase is present only in cold slabs (Torsvik et al., 2016) or also in hotter areas of the CMB as indicated by Koelemeijer et al. (2018). In the first case, the reduced viscosity of the slab decreases the viscosity contrast between cold material and ambient mantle. This results in a similar viscosity structure as we obtain for small values of $\eta_{\Delta T}$, where piles can be even more viscous than slabs. As a consequence, we would expect a comparable behavior of the plume cycle, i.e. a decrease in plume period and more plumes starting at a distance from the pile edge, in agreement with an increased local Rayleigh number Ra_l (M. Li & Zhong, 2017). In contrast, if weak post-bridgmanite is present (almost) everywhere, except for the hottest part of the lower TBL, both slab and pile viscosity would be reduced. Since the viscosity contrast between pile and slab would be maintained and the TBL's local Rayleigh number is not altered, we would expect a similar behavior as in our models, although potentially with a slightly shorter plume period due to a general decrease in viscosity. However, further work would be required to understand the detailed impact of weak post-bridgmanite on plume generation.

II.6.2 Comparison to other geodynamic models

As mentioned before, M. Li et al. (2018) also show a vertical motion of piles as response to plume initiation. Their models also show a quasi-periodic behavior of plume initiation and related pulses in CMB heat flux. However, piles in their models are tent-shaped, with plumes rising at the centre, and the whole pile

moves up and down. In contrast, our models feature plumes rising only at the pile edges, independent of where they are initiated, while plumes fade quickly as soon as they are pushed on top the thermochemical piles. This difference in behavior may be explained by the geometry (cartesian in M. Li et al. (2018) and spherial in this study), and the difference in lowermost-mantle structure. While we model a degree-2 structure, M. Li et al. (2018) have approximately a degree-5 pattern. Their models thus have much stronger TBL flow, comparable to our cases with increased velocity, and therefore more compressed piles. In this case, small thermal instabilities may form at the pile margins, but are rapidly pushed towards the pile centre (M. Li et al., 2018). This could also explains why M. Li et al. (2018) report a vertical motion of the whole pile structure, while this plume-related motion is locally confined to the edges in our models.

Apart from the collapse of the pile edge, the presence of a physical barrier, i.e. the steep pile margin, may play a role in initiation of plumes. As has been previously suggested, lateral flow of hot TBL material along the core-mantle boundary is forced upwards along a (stationary) pile margin, potentially resulting in plumes (Steinberger & Torsvik, 2012; Torsvik et al., 2016; Dannberg & Gassmöller, 2018). Although we cannot rule out the effects of such a barrier on our flow field, it does not provide an explanation for the dynamic behavior of our models: (1) As TBL flow for a time-invariant plate velocity is constant, supply of plume material at the pile margin is uniform and we would not expect plume initiation at a stable physical barrier to be periodic; (2) As can be seen in Figure II.4, each plume initiation starts with a pile collapse and subsequent lateral motion of the pile edge, which provides additional thickening of the lower TBL and can explain the periodicity. As a consequence, our results indicate the predominant impact of local pile edge collapse on plume initiation.

Finally, our observation that plume period increases with thermal viscosity contrast $\eta_{\Delta T}$ (Figure II.5a) explains why a stronger temperature-dependence increases the temporal stability of dense thermochemcial piles (e.g., McNamara & Zhong, 2004; Y. Li et al., 2014; Heyn et al., 2018). While plumes become less frequent with increasing $\eta_{\Delta T}$, their buoyancy flux, and thus their potential to entrain dense pile material, remains almost constant (Figures II.7b and II.7d). In this case, the effective amount of pile material per plume is controlled by the pile density B and the compositional viscosity contrast η_C (Davaille et al., 2002; McNamara & Zhong, 2004; Y. Li et al., 2014; Heyn et al., 2018). Thus, for constant pile properties, longer plume periods, a consqeuence of increased temperature-dependence of viscosity, result in less entrainment over time.

II.6.3 Implications for Earth

Values of pile densities and compositional viscosity contrasts (Table II.1) used in our models are within the range typically applied for primordial material in geodynamic studies (e.g., McNamara & Zhong, 2004; Y. Li et al., 2014; Heyn et al., 2018). Geochmical data supports both increased density and viscosity

for piles, indicating that the viscosity increase may even be greater than set in this work (Trønnes et al., 2019). Basaltic material is expected to have slightly smaller excess density, but may have a similar high viscosity as primordial material (Hirose et al., 2005; Ballmer et al., 2016; Trønnes et al., 2019). Yet, the mechanism of plume initation by pile collapse is not directly dependent on pile properties, and thus would not be altered by the incorporation of recycled oceanic crust as an (upper) part of the pile (Ballmer et al., 2016; Torsvik et al., 2016; Trønnes et al., 2019).

Although our models cannot investigate spatial stability of thermochemical piles, we have shown that pile edges can move within a certain range as response to interactions between pile and plumes. This motion is determined by the viscosity of the pile itself (or more precisely the viscosity contrast between pile and ambient mantle) and the lateral TBL flow, which is controlled by the subduction velocity and the temperature-dependence of viscosity. Since the overall pile thickness is in balance with the average strength of TBL flow and no impact of the plume cycle is visible more than about 5 degrees into the pile, the pile margin motions can be considered local and not reflected in the position of the pile in general. Thus, as long as the distribution of lateral TBL flow around the pile does not change significantly, we do not expect the pile to move. Consequently, the plume cyle and its associated pile edge motion can explain a scattering of (reconstructed) plume positions within a few degrees around the margin observed today (e.g., Torsvik et al., 2016; Torsvik, 2019) without contradicting the stability of a degree-2 structure. Moreover, the mechanism of plume initiation by a local pile edge collapse would predict that the different margins of the LLSVPs may be at very different stages of the plume cycle, thus giving an explanation for the uneven distributions of plumes (French & Romanowicz, 2015).

Even though our models predict a periodic generation of plumes, no such cyclicity for plumes has yet been observed in Earth. This may partially be explained by the limited observations of plumes and LIPs that are available for the last 300 Myr (Figure II.1), with an unknown number of LIPs lost due subduction of oceanic crust (e.g., Torsvik et al., 2016; Torsvik, 2019), and the poor accuracy of plate reconstructions going back more than a few hundred million years (see e.g., Matthews et al., 2016; Torsvik, 2019). Although several LIPs erupted sequentially during the 155-95 Ma period around the southeastern corner of the African LLSVP (Torsvik et al., 2016; Torsvik, 2019), their lateral spread and close proximity in time do not provide constraints on plume periodicity in Earth. Based on available data, it is difficult to infer potential plume periodicity of 300-500 Myr as observed in our 2-D models. A further explanation for the absence of a clear plume periodicty might be given by the subduction velocity and the configuration of plates, which are both very simplified in our models. As we showed with periodic plate velocities or increased/ decreased plate speeds, subduction velocities have a significant effect on the initiation of plumes. For Earth, they are likely to change considerably and consistently, both in time and space (Matthews et al., 2016). Consequently, neither coherent slabs

nor a constant lateral TBL flow (magnitude and direction) are likely to occur in Earth over long periods of time. Thus, we can expect the Earth's lower mantle to be in a kind of adjustment time stage for most of Earth's history, making it difficult to reach a state of periodic plume generation that we observed for well-defined constant or periodic plate velocities.

Yet, the mechanism of plume initiation due to pile collapse may play an important role for the initiation of individual plumes. As mentioned above, there is a clustering of LIPs in the southeastern corner of the African LLSPV (Figure II.1), where at least 8 plumes erupted within about 60 Myr (Torsvik et al., 2016; Torsvik, 2019). Such a sequence might be explained by a larger-scale collapse of that part of the pile, which could initiate plumes in several locations around the collapsing edge at approximately the same time, although small time delays and differences in rise time are very likely to occur. The collapse could be related to a significant reduction in the CMB flow, e.g. a reduction in plate velocity or change in TBL flow direction due to a modified configuration for the respective subduction zone(s) at the surface. If a subduction zone above an area of persistent downwelling changes its configuration (geomerty, subduction velocity), this may cause a change in sinking velocity of the whole column and thus modify lateral TBL flow on shorter time scales than it takes slabs to sink through the whole mantle. In fact, plate reconstructions show a subduction zone closing in around the southern margin of Gondwana during the breakup of Pangaea between 250 Ma and 200 Ma, which then retreats between 200 Ma and 100 Ma (Matthews et al., 2016). The first stage would potentially result in increased TBL flow and pile thickness, while the retreating subduction zones would reduce TBL flow and may trigger a graviational collapse of the southeastern LLSVP egde. The delay between retreating subduction zones and the emplacement of LIPs at the surface (about 50-100 Myr together) can be explained by the reaction time of the deep mantle and the rise time of plumes.

II.7 Conclusions

In this study, we have shown that plumes at the core-mantle boundary can be triggered by two ways of increasing the thickness of the lower TBL. One is the conductive growth of the boundary layer, resulting in plumes appearing at random locations once the local Rayleigh number has exceeded a critical value (Deschamps & Tackley, 2008; M. Li & Zhong, 2017). This sets a minimum "natural" period $\mathcal{T}_{TBL}$ at which plumes are generated from the CMB, but does not necessarily represent the observed period in the presence of a thermochemical pile.

The other mechanism is a periodic gravitational collapse of the edge of a thermochemical pile on the CMB. This collapse occurs as plumes locally thicken the pile when they interact with the pile margin, and resembles the vertical motion of tent-shaped piles observed by M. Li and Zhong (2017). When the increased pile thickness is no longer supported due to cooling of the pile top

and reduced dynamic uplift from the rising plume, the pile margin collapses back towards the CMB and spreads laterally. This process pushes TBL material against the dominant flow direction and causes local thickening of the TBL just outside the thermochemical pile, triggering a new "early" plume.

The period of this pile collapse, $\mathcal{T}_{\mathrm{Pile}}$, depends on the mantle wind along the CMB, which is controlled by the temperature-dependence of viscosity (whic affects the sinking velocity of slabs) and velocity with which plates are subducted. The latter can modify the observed plume period, but shorter periods resulting from faster plate velocities reduce plume strength. For periodic plate velocities, plume periods can adjust to imposed plate cycles within a certain resonance range around characteristic period $\mathcal{T}_{\mathrm{Pile}}$. For $\mathcal{T}_{\mathrm{TBL}} > \mathcal{T}_{\mathrm{Pile}}$, plumes are predominantly initated at the pile margin and the effectively observed period is $\mathcal{T}_{\mathrm{Pile}}$, with potentially weak plumes for $\mathcal{T}_{\mathrm{TBL}} \gg \mathcal{T}_{\mathrm{Pile}}$. In contrast $\mathcal{T}_{\mathrm{TBL}} < \mathcal{T}_{\mathrm{Pile}}$ causes plume initiation both atthe pile margins and away from them, resulting in a more aperiodic behavior.

Although there is currently insufficient data from LIPs or hotspots to infer a cyclicity in plume initiation within Earth's mantle, we would estimate the Earth to be in the regime of $\mathcal{T}_{\mathrm{TBL}} \gtrsim \mathcal{T}_{\mathrm{Pile}}$ since most LIPs/ hotspots are clustered around the LLSVP margins. Yet, plumes have to be strong enough to reach the surface, presumably excluding "very early" plume initiation ($\mathcal{T}_{\mathrm{TBL}} \gg \mathcal{T}_{\mathrm{Pile}}$). Finally, the mechanism for plume generation at the edges of thermochemical piles may explain the observed clustering of LIPs between 95 Ma and 155 Ma at the southeastern corner of the African LLSVP.

References

Ammann, M. W., Brodholt, J. P., Wookey, J., & Dobson, D. P. (2010, May). First-principles constraints on diffusion in lower-mantle minerals and a

weak d layer. *Nature*, *465*, 462–465. Retrieved from `https://www.nature.com/articles/nature09052#supplementary-information` doi: 10.1038/nature09052; 10.1038/nature09052

Austermann, J., Kaye, B. T., Mitrovica, J. X., & Huybers, P. (2014, 01). A statistical analysis of the correlation between large igneous provinces and lower mantle seismic structure. *Geophysical Journal International*, *197*(1), 1–9. Retrieved from `https://doi.org/10.1093/gji/ggt500` doi: 10.1093/gji/ggt500

Ballmer, M. D., Schumacher, L., Lekic, V., Thomas, C., & Ito, G. (2016). Compositional layering within the large low shear-wave velocity provinces in the lower mantle. *Geochemistry, Geophysics, Geosystems*, *17*(12), 5056–5077. Retrieved from `https://agupubs.onlinelibrary.wiley.com/doi/abs/10.1002/2016GC006605` doi: 10.1002/2016GC006605

Bangerth, W., Dannberg, J., Gassmoeller, R., Heister, T., et al. (2018, June). *ASPECT v2.0.1 [software].* Davis, CA. Retrieved from `https://doi.org/10.5281/zenodo.1297145` doi: 10.5281/zenodo.1297145

Bangerth, W., Dannberg, J., Gassmöller, R., Heister, T., et al. (2019, April). ASPECT: Advanced solver for problems in earth's convection, user manual. Retrieved from `https://doi.org/10.6084/m9.figshare.4865333` (doi:10.6084/m9.figshare.4865333) doi: 10.6084/m9.figshare.4865333

Conrad, C. P., Steinberger, B., & Torsvik, T. H. (2013, June). Stability of active mantle upwelling revealed by net characteristics of plate tectonics. *Nature*, *498*, 479–482. Retrieved from `https://www.nature.com/articles/nature12203#supplementary-information` doi: 10.1038/nature12203; 10.1038/nature12203

Cottaar, S., & Lekic, V. (2016, 08). Morphology of seismically slow lower-mantle structures. *Geophysical Journal International*, *207*(2), 1122–1136. Retrieved from `https://doi.org/10.1093/gji/ggw324` doi: 10.1093/gji/ggw324

Dannberg, J., & Gassmöller, R. (2018). Chemical trends in ocean islands explained by plume–slab interaction. *Proceedings of the National Academy of Sciences*, *115*(17), 4351–4356. Retrieved from `https://www.pnas.org/content/115/17/4351` doi: 10.1073/pnas.1714125115

Dannberg, J., & Sobolev, S. V. (2015, April). Low-buoyancy thermochemical plumes resolve controversy of classical mantle plume concept. *Nature Communications*, *6*, 6960. Retrieved from `https://www.nature.com/articles/ncomms7960#supplementary-information` doi: 10.1038/ncomms7960; 10.1038/ncomms7960

Davaille, A., Girard, F., & Bars, M. L. (2002). How to anchor hotspots in a convecting mantle? *Earth and Planetary Science Letters*, *203*(2), 621–634. Retrieved from `http://www.sciencedirect.com/science/article/pii/S0012821X0200897X` doi: 10.1016/S0012-821X(02)00897-X

Davies, D. R., Goes, S., Davies, J., Schuberth, B., Bunge, H.-P., & Ritsema, J. (2012). Reconciling dynamic and seismic models of earth's lower mantle: The dominant role of thermal heterogene-

ity. *Earth and Planetary Science Letters*, *353-354*, 253–269. Retrieved from http://www.sciencedirect.com/science/article/pii/S0012821X1200444X doi: 10.1016/j.epsl.2012.08.016

Davies, D. R., Goes, S., & Sambridge, M. (2015). On the relationship between volcanic hotspot locations, the reconstructed eruption sites of large igneous provinces and deep mantle seismic structure. *Earth and Planetary Science Letters*, *411*, 121–130. Retrieved from http://www.sciencedirect.com/science/article/pii/S0012821X14007523 doi: 10.1016/j.epsl.2014.11.052

Deschamps, F., & Tackley, P. J. (2008). Searching for models of thermochemical convection that explain probabilistic tomography: I. principles and influence of rheological parameters. *Physics of the Earth and Planetary Interiors*, *171*(1), 357–373. Retrieved from http://www.sciencedirect.com/science/article/pii/S0031920108000824 (Recent Advances in Computational Geodynamics: Theory, Numerics and Applications) doi: 10.1016/j.pepi.2008.04.016

Doubrovine, P. V., Steinberger, B., & Torsvik, T. H. (2016). A failure to reject: Testing the correlation between large igneous provinces and deep mantle structures with edf statistics. *Geochemistry, Geophysics, Geosystems*, *17*(3), 1130–1163. Retrieved from https://agupubs.onlinelibrary.wiley.com/doi/abs/10.1002/2015GC006044 doi: 10.1002/2015GC006044

Dziewonski, A. M., Lekic, V., & Romanowicz, B. A. (2010). Mantle anchor structure: An argument for bottom up tectonics. *Earth and Planetary Science Letters*, *299*(1), 69–79. Retrieved from http://www.sciencedirect.com/science/article/pii/S0012821X10005236 doi: 10.1016/j.epsl.2010.08.013

Farnetani, C. G., Hofmann, A. W., Duvernay, T., & Limare, A. (2018). Dynamics of rheological heterogeneities in mantle plumes. *Earth and Planetary Science Letters*, *499*, 74–82. Retrieved from http://www.sciencedirect.com/science/article/pii/S0012821X1830428X doi: 10.1016/j.epsl.2018.07.022

French, S. W., & Romanowicz, B. (2015, September). Broad plumes rooted at the base of the earth's mantle beneath major hotspots. *Nature*, *525*, 95. Retrieved from https://www.nature.com/articles/nature14876#supplementary-information doi: 10.1038/nature14876; 10.1038/nature14876

Garnero, E. J., & McNamara, A. K. (2008). Structure and dynamics of earth's lower mantle. *Science*, *320*(5876), 626–628. Retrieved from https://science.sciencemag.org/content/320/5876/626 doi: 10.1126/science.1148028

Garnero, E. J., McNamara, A. K., & Shim, S.-H. (2016, June). Continent-sized anomalous zones with low seismic velocity at the base of earth's mantle. *Nature Geoscience*, *9*, 481–489. Retrieved from https://www.nature.com/articles/ngeo2733#supplementary-information doi: 10.1038/ngeo2733; 10.1038/ngeo2733

Hager, B. H., Clayton, R. W., Richards, M. A., Comer, R. P., & Dziewonski, A. M.

(1985). Lower mantle heterogeneity, dynamic topography and the geoid. *Nature*, *313*(6003), 541–545. doi: 10.1038/313541a0; 10.1038/313541a0

He, Y., Puckett, E. G., & Billen, M. I. (2017). A discontinuous Galerkin method with a bound preserving limiter for the advection of non-diffusive fields in solid earth geodynamics. *Physics of the Earth and Planetary Interiors*, *263*, 23–37. Retrieved from `https://doi.org/10.1016/j.pepi.2016.12.001` doi: 10.1016/j.pepi.2016.12.001

Heister, T., Dannberg, J., Gassmöller, R., & Bangerth, W. (2017). High accuracy mantle convection simulation through modern numerical methods. II: Realistic models and problems. *Geophysical Journal International*, *210*(2), 833–851. Retrieved from `https://doi.org/10.1093/gji/ggx195` doi: 10.1093/gji/ggx195

Heyn, B. H., Conrad, C. P., & Trønnes, R. G. (2018). Stabilizing effect of compositional viscosity contrasts on thermochemical piles. *Geophysical Research Letters*, *45*(15), 7523–7532. Retrieved from `https://agupubs.onlinelibrary.wiley.com/doi/abs/10.1029/2018GL078799` doi: 10.1029/2018GL078799

Hirose, K., Takafuji, N., Sata, N., & Ohishi, Y. (2005). Phase transition and density of subducted morb crust in the lower mantle. *Earth and Planetary Science Letters*, *237*(1), 239–251. Retrieved from `http://www.sciencedirect.com/science/article/pii/S0012821X0500419X` doi: 10.1016/j.epsl.2005.06.035

Koelemeijer, P. J., Deuss, A., & Ritsema, J. (2017, May). Density structure of earth's lowermost mantle from stoneley mode splitting observations. *Nature Communications*, *8*, 15241. Retrieved from `https://www.nature.com/articles/ncomms15241#supplementary-information` doi: 10.1038/ncomms15241; 10.1038/ncomms15241

Koelemeijer, P. J., Schuberth, B., Davies, D., Deuss, A., & Ritsema, J. (2018). Constraints on the presence of post-perovskite in earth's lowermost mantle from tomographic-geodynamic model comparisons. *Earth and Planetary Science Letters*, *494*, 226–238. Retrieved from `http://www.sciencedirect.com/science/article/pii/S0012821X18302656` doi: 10.1016/j.epsl.2018.04.056

Kronbichler, M., Heister, T., & Bangerth, W. (2012). High accuracy mantle convection simulation through modern numerical methods. *Geophysical Journal International*, *191*, 12–29. Retrieved from `http://dx.doi.org/10.1111/j.1365-246X.2012.05609.x` doi: 10.1111/j.1365-246X.2012.05609.x

Labrosse, S., Hernlund, J. W., & Coltice, N. (2007, December). A crystallizing dense magma ocean at the base of the earth's mantle. *Nature*, *450*, 866–869. Retrieved from `https://www.nature.com/articles/nature06355#supplementary-information` doi: 10.1038/nature06355; 10.1038/nature06355

Lau, H. C. P., Mitrovica, J. X., Davis, J. L., Tromp, J., Yang, H.-Y., & Al-Attar, D. (2017, November). Tidal tomography constrains earth's deep-mantle buoyancy. *Nature*, *551*, 321–326. doi: 10.1038/nature24452;

10.1038/nature24452

Lekic, V., Cottaar, S., Dziewonski, A., & Romanowicz, B. (2012). Cluster analysis of global lower mantle tomography: A new class of structure and implications for chemical heterogeneity. *Earth and Planetary Science Letters*, *357-358*, 68–77. Retrieved from `http://www.sciencedirect.com/science/article/pii/S0012821X12005109` doi: 10.1016/j.epsl.2012.09.014

Li, M., & McNamara, A. K. (2013). The difficulty for subducted oceanic crust to accumulate at the earth's core-mantle boundary. *Journal of Geophysical Research: Solid Earth*, *118*(4), 1807–1816. Retrieved from `https://agupubs.onlinelibrary.wiley.com/doi/abs/10.1002/jgrb.50156` doi: 10.1002/jgrb.50156

Li, M., McNamara, A. K., & Garnero, E. J. (2014, March). Chemical complexity of hotspots caused by cycling oceanic crust through mantle reservoirs. *Nature Geoscience*, *7*, 366–370. Retrieved from `https://www.nature.com/articles/ngeo2120#supplementary-information` doi: 10.1038/ngeo2120; 10.1038/ngeo2120

Li, M., & Zhong, S. (2017). The source location of mantle plumes from 3d spherical models of mantle convection. *Earth and Planetary Science Letters*, *478*, 47–57. Retrieved from `http://www.sciencedirect.com/science/article/pii/S0012821X17304806` doi: 10.1016/j.epsl.2017.08.033

Li, M., Zhong, S., & Olson, P. (2018). Linking lowermost mantle structure, core-mantle boundary heat flux and mantle plume formation. *Physics of the Earth and Planetary Interiors*, *277*, 10–29. Retrieved from `http://www.sciencedirect.com/science/article/pii/S0031920117302625` doi: 10.1016/j.pepi.2018.01.010

Li, Y., Deschamps, F., & Tackley, P. J. (2014, 09). The stability and structure of primordial reservoirs in the lower mantle: insights from models of thermochemical convection in three-dimensional spherical geometry. *Geophysical Journal International*, *199*(2), 914–930. Retrieved from `https://doi.org/10.1093/gji/ggu295` doi: 10.1093/gji/ggu295

Li, Y., Deschamps, F., & Tackley, P. J. (2015). Effects of the post-perovskite phase transition properties on the stability and structure of primordial reservoirs in the lower mantle of the earth. *Earth and Planetary Science Letters*, *432*, 1–12. Retrieved from `http://www.sciencedirect.com/science/article/pii/S0012821X15006159` doi: 10.1016/j.epsl.2015.09.040

Matthews, K. J., Maloney, K. T., Zahirovic, S., Williams, S. E., Seton, M., & Müller, R. D. (2016). Global plate boundary evolution and kinematics since the late paleozoic. *Global and Planetary Change*, *146*, 226–250. Retrieved from `http://www.sciencedirect.com/science/article/pii/S0921818116302417` doi: 10.1016/j.gloplacha.2016.10.002

McNamara, A. K., & Zhong, S. (2004). Thermochemical structures within a spherical mantle: Superplumes or piles? *Journal of Geophysical Research: Solid Earth*, *109*(B7). Retrieved from `https://agupubs.onlinelibrary.wiley.com/doi/abs/10.1029/2003JB002847` doi: 10.1029/2003JB002847

McNamara, A. K., & Zhong, S. (2005). Thermochemical structures beneath

africa and the pacific ocean. *Nature*, *437*(7062), 1136–1139. doi: 10.1038/nature04066; 10.1038/nature04066

Mulyukova, E., Steinberger, B., Dabrowski, M., & Sobolev, S. V. (2015). Survival of llsvps for billions of years in a vigorously convecting mantle: Replenishment and destruction of chemical anomaly. *Journal of Geophysical Research: Solid Earth*, *120*(5), 3824–3847. Retrieved from `https://agupubs.onlinelibrary.wiley.com/doi/abs/10.1002/2014JB011688` doi: 10.1002/2014JB011688

Nakagawa, T., & Tackley, P. J. (2011). Effects of low-viscosity post-perovskite on thermo-chemical mantle convection in a 3-d spherical shell. *Geophysical Research Letters*, *38*(4). Retrieved from `https://agupubs.onlinelibrary.wiley.com/doi/abs/10.1029/2010GL046494` doi: 10.1029/2010GL046494

Schuberth, B. S. A., Bunge, H.-P., & Ritsema, J. (2009). Tomographic filtering of high-resolution mantle circulation models: Can seismic heterogeneity be explained by temperature alone? *Geochemistry, Geophysics, Geosystems*, *10*(5). Retrieved from `https://agupubs.onlinelibrary.wiley.com/doi/abs/10.1029/2009GC002401` doi: 10.1029/2009GC002401

Schuberth, B. S. A., Bunge, H.-P., Steinle-Neumann, G., Moder, C., & Oeser, J. (2009). Thermal versus elastic heterogeneity in high-resolution mantle circulation models with pyrolite composition: High plume excess temperatures in the lowermost mantle. *Geochemistry, Geophysics, Geosystems*, *10*(1). Retrieved from `https://agupubs.onlinelibrary.wiley.com/doi/abs/10.1029/2008GC002235` doi: 10.1029/2008GC002235

Schuberth, B. S. A., Zaroli, C., & Nolet, G. (2012, 03). Synthetic seismograms for a synthetic earth: long-period p- and s-wave traveltime variations can be explained by temperature alone. *Geophysical Journal International*, *188*(3), 1393–1412. Retrieved from `https://doi.org/10.1111/j.1365-246X.2011.05333.x` doi: 10.1111/j.1365-246X.2011.05333.x

Steinberger, B., & Torsvik, T. H. (2012). A geodynamic model of plumes from the margins of large low shear velocity provinces. *Geochemistry, Geophysics, Geosystems*, *13*(1). Retrieved from `https://agupubs.onlinelibrary.wiley.com/doi/abs/10.1029/2011GC003808` doi: 10.1029/2011GC003808

Tackley, P. J. (2012). Dynamics and evolution of the deep mantle resulting from thermal, chemical, phase and melting effects. *Earth-Science Reviews*, *110*(1), 1–25. Retrieved from `http://www.sciencedirect.com/science/article/pii/S0012825211001486` doi: 10.1016/j.earscirev.2011.10.001

Torsvik, T. H. (2019). Earth history: A journey in time and space from base to top. *Tectonophysics*, *760*, 297–313. Retrieved from `http://www.sciencedirect.com/science/article/pii/S0040195118303147` (Linking Plate Tectonics and Volcanism to Deep Earth Dynamics – a tribute to Trond H. Torsvik) doi: 10.1016/j.tecto.2018.09.009

Torsvik, T. H., Burke, K., Steinberger, B., Webb, S. J., & Ashwal, L. D. (2010, July). Diamonds sampled by plumes from the core–mantle boundary. *Nature*, *466*, 352–355. Retrieved from `https://www.nature.com/articles/nature09216#supplementary-information` doi: 10.1038/nature09216; 10.1038/nature09216

Torsvik, T. H., Smethurst, M. A., Burke, K., & Steinberger, B. (2006). Large igneous provinces generated from the margins of the large low-velocity provinces in the deep mantle. *Geophysical Journal International*, *167*(3), 1447–1460. Retrieved from `https://onlinelibrary.wiley.com/doi/abs/10.1111/j.1365-246X.2006.03158.x` doi: 10.1111/j.1365-246X.2006.03158.x

Torsvik, T. H., Steinberger, B., Ashwal, L. D., Doubrovine, P. V., & Trønnes, R. G. (2016). Earth evolution and dynamics—a tribute to kevin burke. *Canadian Journal of Earth Sciences*, *53*(11), 1073–1087. Retrieved from `https://doi.org/10.1139/cjes-2015-0228` doi: 10.1139/cjes-2015-0228

Trønnes, R. G., Baron, M., Eigenmann, K., Guren, M., Heyn, B., Løken, A., & Mohn, C. (2019). Core formation, mantle differentiation and core-mantle interaction within earth and the terrestrial planets. *Tectonophysics*, *760*, 165–198. Retrieved from `http://www.sciencedirect.com/science/article/pii/S0040195118303494` (Linking Plate Tectonics and Volcanism to Deep Earth Dynamics – a tribute to Trond H. Torsvik) doi: 10.1016/j.tecto.2018.10.021

Paper III

Core-mantle boundary topography and its relation to the viscosity structure of the lowermost mantle

Björn H. Heyn, Clinton P. Conrad, Reidar G. Trønnes

Under review in *Earth and Planetary Science Letters*

Abstract

Two large areas of anomalously low seismic velocities are visible in all tomographic models of the lowermost mantle. If these Large Low Shear Velocity Provinces (LLSVPs) represent piles of hot but chemically dense material, the core-mantle boundary (CMB) should deform due to isostatic and dynamic topography, the latter being sensitive to the viscosity structure of the lowermost mantle. Heterogeneities in the viscosity structure, although difficult to constrain, might be especially important if the thermochemical piles have elevated intrinsic viscosity as suggested by geochemistry. Based on numerical models, we identify a short-wavelength (about 80-120 km wide, up to a few km deep) topographic depression that forms around the pile edges if the pile is more viscous than the surrounding mantle. The depression forms as a wedge of thermal boundary layer material becomes compressed against the viscous pile, and is enhanced by relative uplift of the CMB beneath the pile by plumes rising above it. Depth and asymmetry of the depression constrain the magnitude of the viscosity contrast between pile and mantle. Furthermore, (periodic) plume initiation and pile collapse at the pile margin systematically modify the characteristic depression, with a maximum in asymmetry and depth at the time of plume initiation. Core-reflected waves or scattered energy may be used to detect this topographic structure of stiff thermochemical piles at the base of the mantle.

III.1 Introduction

Although the presence of a dominant degree-2 structure in seismic velocities of the lowermost mantle is well established (e.g., Dziewonski et al., 2010; Cottaar & Lekic, 2016), the origins, and therefore the properties, of the Large Low Shear Velocity Provinces (LLSVPs) are still under debate (e.g., McNamara & Zhong, 2004; Davies et al., 2012; Y. Li et al., 2014; Mulyukova et al., 2015; Trønnes

et al., 2019). Some studies suggest a thermal origin of the velocity anomaly (e.g., Schuberth et al., 2012; Davies et al., 2012), while most geodynamic models prefer thermochemical piles of dense material (e.g., McNamara & Zhong, 2004; Y. Li et al., 2014; Mulyukova et al., 2015). Seismic observations, such as sharp and steep boundaries, are often used to support the hypothesis of a chemical origin of LLSVPs (see review by McNamara, 2019, and references therein), yet they can possibly also be explained by strong temperature gradients (Schuberth et al., 2012; Davies et al., 2012).

One way to discriminate between thermal and thermochemical structures is via their density anomaly relative to the ambient mantle, which is negative for thermal upwellings and neutral to positive in the case of thermochemical piles. Estimated densities of LLSVPs from normal mode data and Earth's solid tides range from neutral or even slightly reduced density (Koelemeijer et al., 2017) to about 0.5-1% excess density (Lau et al., 2017), but these estimates include both the effect of thermal expansion and a potential compositional density increase. Moreover, there are two possible candidate materials for thermochemical piles with different properties: dense and presumably viscous primordial iron-rich bridgmanite (Williams et al., 2015; Heyn et al., 2018; Trønnes et al., 2019), or recycled oceanic crust (M. Li & McNamara, 2013; Mulyukova et al., 2015) with reduced excess density and increased bulk modulus relative to the ambient peridotite (Ballmer et al., 2016; Trønnes et al., 2019), which potentially increases the viscosity of the basaltic material. Consequently, as compositionally distinct pile material can exhibit a range of different excess densities, discrimination between thermal and thermochemical LLSVPs based only on density is not straightforward. Yet, since basaltic material may and bridgmanitic rocks are expected to have a higher intrinsic viscosity (e.g., Torsvik et al., 2016; Trønnes et al., 2019), details about the viscosity structure in the lowermost mantle would, together with density estimates, provide important insight into the thermal vs. thermochemical nature of the LLSVPs. Unfortunately, we have no direct way of measuring viscosity in the lowermost mantle.

The presence of a thermochemical pile at the base of the mantle is expected to affect flow patterns in the deep Earth. Conrad et al. (2013) have shown that there has been persistent upwelling above the LLSVP regions for at least 250 Myr. Moreover, reconstructed eruption sites of Large Igneous Provinces (LIPs) and kimberlites, both related to deep-rooted mantle plumes, cluster around the margins of the LLSVPs (Torsvik et al., 2016; Doubrovine et al., 2016), although the correlation has been questioned (e.g., Austermann et al., 2014). This proximity of plumes to the LLSVP margins may be a result of D" flow, which is forced upwards at the edges of dense piles, triggering plumes (Steinberger & Torsvik, 2012; Torsvik et al., 2016; Heyn et al., 2018). These density and flow heterogeneities impact the CMB: Both the isostatic load due to mass (e.g. dense piles) and the dynamic pressure associated with sinking or rising flow exert radial stresses on the boundary between the mantle and the liquid outer core.

The amplitude of the resulting deflection depends on the density and viscosity of the material, as well as its velocity. As for the Earth's surface, these stresses are expressed as dynamic topography, with positive topography being associated with light material and rising flow (Figure III.1c), while dense sinking material causes depressions (Lassak et al., 2007; Steinberger & Holme, 2008; Yoshida, 2008; Deschamps et al., 2017). Consequently, core-mantle boundary topography can be used as a proxy to investigate flow in the lowermost mantle as well as certain material properties such as the viscosity and density structures of a (potentially) thermochemical pile (Lassak et al., 2007, 2010; Deschamps et al., 2017).

Core-mantle boundary topography may also impact core flow and the Earth's dynamo. It has been suggested that topography of the CMB may cause a torque in core flow and thus result in exchange of angular momentum between the mantle and the core (Le Mouël et al., 2006; Roberts & Aurnou, 2012; Ding & Chao, 2018; Glane & Buffett, 2018; Burmann & Noir, 2018). This exchange, potentially strengthened by the presence of stable stratification of the outer core (Glane & Buffett, 2018), has been invoked to explain periodic changes in length-of-day (Roberts & Aurnou, 2012; Ding & Chao, 2018; Glane & Buffett, 2018). Profiles of seismic velocities and geochemical data both indicate that a light stagnant layer (often called the E'-layer) may indeed be present within Earth's outer core (e.g. review by Trønnes et al., 2019, and references therein), potentially making CMB topography even more important. Furthermore, it has been suggested that CMB topography affects convective flow in the outer core, thereby causing secular variations in Earth's magnetic field (Roberts & Aurnou, 2012).

There are several estimates of CMB topography derived from seismology (e.g., Tanaka, 2010; Koelemeijer et al., 2012; Schlaphorst et al., 2015; Colombi et al., 2014) and various geodynamic studies (Lassak et al., 2007; Steinberger & Holme, 2008; Yoshida, 2008; Lassak et al., 2010; Soldati et al., 2012; Deschamps et al., 2017; Deschamps & Li, 2019). Global maps of CMB topography up to spherical harmonic degree 4 can be obtained with normal modes (Koelemeijer et al., 2012) or body wave data (e.g., Tanaka, 2010), but both topography amplitudes and patterns vary significantly between different studies due to trade-offs between CMB topography and the mantle's density and velocity structure (see e.g. Tanaka, 2010, and references therein). Geodynamic studies have shown that low spherical harmonic degrees cannot distinguish between positive topography predicted for either thermal or light thermochemical LLSVPs, while piles with excess density higher than 1.8-2% cause a depression of the CMB (Lassak et al., 2007; Steinberger & Holme, 2008; Yoshida, 2008; Lassak et al., 2010; Deschamps et al., 2017; Deschamps & Li, 2019). In addition, there are a few regional studies studies using core-reflected waves for structures with wavelengths around 100 km (e.g., Restivo & Helffrich, 2006; Wu et al., 2014; Gassner et al., 2015; Schlaphorst et al., 2015; Mancinelli & Shearer, 2016; Shen et al., 2016). More recently, Mancinelli and Shearer (2016) obtained topography

of even shorter length scales of approximately 7 km by analysing scattered energy.
Yet, since observations of short-wavelength CMB topography are sparse, no
systematic pattern of structures smaller than about 300 km has been detected yet.

In this study, we present numerical models to predict short-wavelength
topography, showing that topographic length scales of about 100 km are sensitive
to a potential viscosity contrast between thermochemical piles and the ambient
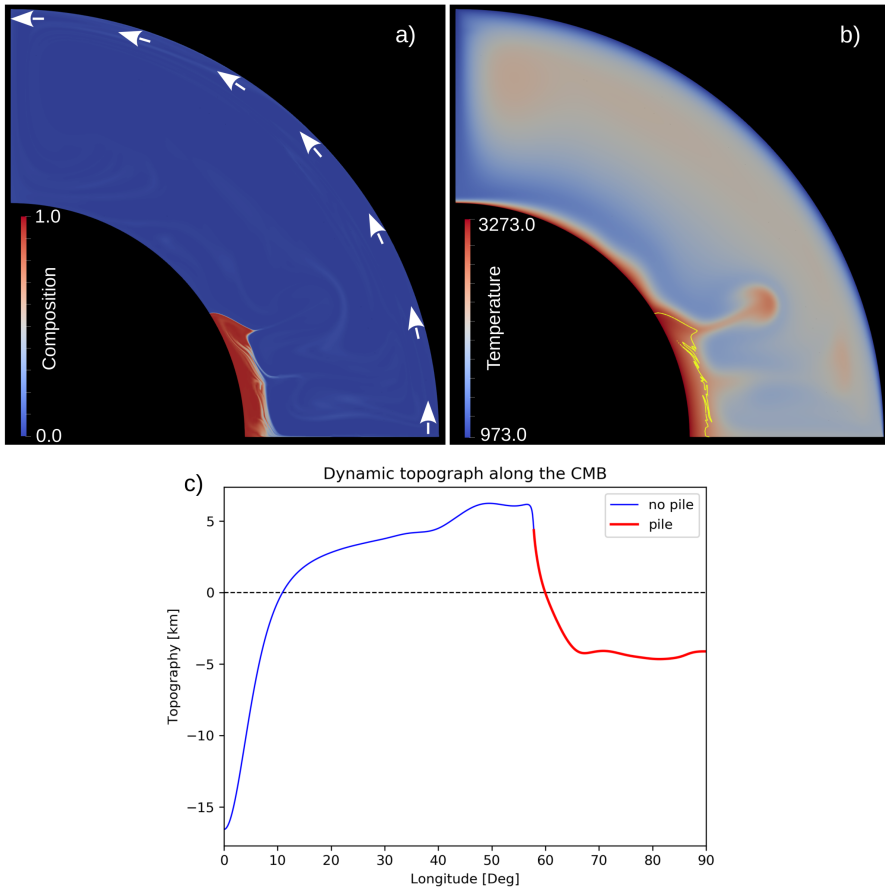

Figure III.1: Initial condition of (a) the compositional field and (b) the
temperature field. White arrows in (a) indicate the velocity boundary condition,
while the yellow line in (b) marks the outline of the pile for a composition value
of $C = 0.8$. The general pattern of core-mantle boundary topography obtained
for this type of model is shown in (c), with the line color indicating the area
underneath the pile (red) and outside the pile (blue). Depressions are observed
beneath the slab at longitude 0 deg due to the sinking flow, and the dense pile.
The area around the pile margin is uplifted due to rising flow.

mantle. Thus, measurements of short-scale topography at the CMB may constrain the thermal or thermochemical nature of LLSVPs. Moreover, it may allow for the identification of plumes at early stages.

III.2 Model setup

Our numerical models are run with the finite element code ASPECT (Kronbichler et al., 2012; Heister et al., 2017; He et al., 2017; Bangerth et al., 2018, 2019) in a 2-D spherical geometry. Equations describing the conservation of mass, energy and momentum are solved under the Boussinesq approximation. In general, the setup is similar to Heyn et al. (2018), and parameters are chosen so that the reference Rayleigh number, describing the vigor of convection via the definition

$$Ra = \frac{\alpha \rho g \Delta T d^3}{\kappa \eta},$$
(III.1)

equals to 10^7. Parameters in Equation (III.1) are thermal expansivity α, density ρ, temperature drop across the mantle ΔT, gravitational acceleration g, mantle thickness d, reference viscosity η and thermal diffusivity κ.

Our domain is chosen as a quarter of an annulus along the equator with a grid that is adaptively refined based on the compositon and viscosity gradients after every 10 time steps of the calculation. Moreover, we performed runs for which cells are additionally refined in the lowermost mantle close to the core-mantle boundary such that the CMB is equally sampled everywhere. The effective resolution in regular models varies between about $7 \times 11 \, \text{km}$ and $80 \times 90 \, \text{km}$ (lateral x radial), while our resolution tests have smallest cells of about $1.4 \, \text{km}$ at the CMB (see discussion further down). A constant uniform velocity boundary condition of $1.48 \, \text{cm/year}$ is imposed on the surface to force a single-plate degree-2 flow structure (Figure III.1a), while all other boundaries are free-slip. All parameters characterizing the general setup are given in Table III.1.

Core-mantle boundary topography is derived from radial stresses calculated along the interface between mantle and core via the relation

$$h = \frac{\sigma_{rr}}{g \Delta \rho_{CMB}},$$
(III.2)

with h being the CMB topography, σ_{rr} the radial component of the stress, and $\Delta \rho_{CMB}$ the density difference between core and ambient mantle, which is set to $4400 \, \frac{\text{kg}}{\text{m}^3}$ based on PREM (Dziewonski & Anderson, 1981). To ensure that our imposed plate velocity does not affect the core-mantle boundary topography, we also performed tests in which we replaced the surface velocity boundary condition by a free slip condition after a while. Since we have no slab weaking mechanism, subduction in these models slowed down and finally stopped completely, thereby changing the mode of convection. However, during the transition phase, the observed dynamic topography does not change significantly until subduction

stops, and the lateral thermal boundary layer (TBL) flow towards the pile ceases. Thus, we conclude that our choice of imposed surface velocity boundary condition does not affect the predicted CMB topography.

Our system is heated from below and from within by uniform internal heating (Table III.1). Piles of dense material are represented by a compositional field that is advected with the discontinuous Galerkin method (He et al., 2017). A density contrast between thermochemical piles and regular mantle is prescribed via the buoyancy ratio

$$B = \frac{\Delta \rho_C}{\alpha \rho \Delta T}, \tag{III.3}$$

with $\Delta \rho_C$ being the density difference due to composition.

Table III.1: Characteristic parameters used in our thermochemical calculations. We convert excess densities into B (Equation (II.3)) by assuming a 3300 K temperature drop across the mantle, which includes both the 2300 K superadiabatic temperature drop that we have in our models with Boussinesq approximation, and an adiabatic temperature increase of 1000 K. Furthermore, although we assume a constant value of $\alpha = 3.0 \cdot 10^{-5}$ for the whole mantle within the models, we use a more realistic CMB thermal expansivity of $\alpha = 1.0 \cdot 10^{-5}$ at the CMB for conversion to B (Tackley, 2012). Based on that, we obtain buoyancy numbers comparable to previous studies (e.g., McNamara & Zhong, 2004; Mulyukova et al., 2015; Heyn et al., 2018). We also use the full temperature drop of 3300 K to calculate Ra, which is set to 10^7. Within ASPECT, we use thermal conductivity k and specific heat capacity c_P instead of the thermal diffusivity κ, but they can be converted via $\kappa = \frac{k}{\rho c_P}$. In our models, we set κ equal to $1.0 \cdot 10^{-6}$ [m^2/s].

Parameter	Symbol	Value [Unit]
Gravitational acceleration	g	9.81 [m/s^2]
Mantle thickness	d	2890 [km]
Reference density (upper mantle)	ρ	3340 [kg/m^3]
Reference viscosity	η	$7.83 \cdot 10^{21}$ [Pa·s]
Thermal conductivity	k	4.01 [W/K·m]
Specific heat	c_P	1200 [kg·m^2/(K·s^2)]
Thermal expansivity	α	$3.0 \cdot 10^{-5}$ [1/K]
Chemical excess density	$\Delta \rho_C$	$198.396 - 330.66$ [kg/m^3]
Buoyancy ratio (Equation (II.3))	B	$0.6 - 1.0$ [ ]
Rayleigh number	Ra	10^7 [ ]
Internal heating rate	H	$9.46 \cdot 10^{-13}$ [W/kg]
Imposed surface velocity	v_{surf}	1.48 [cm/yr]
Compositional viscosity contrast	η_C	$1 - 20$ [ ]
Thermal viscosity contrast	$\eta_{\Delta T}$	$2.3 - 7500$ [ ]
Temperature drop across mantle	ΔT	2300 [K]
Density difference core-to-mantle	$\Delta \rho_{CM}$	4400 [kg/m^3]

Similar to Heyn et al. (2018), our viscosity depends on temperature, depth and composition, given by

$$
\begin{aligned}
\eta(z, T, C) &= \eta_0(z)\eta_{\Delta T}(z, T)\exp\left[C\ln\eta_C\right] \\
&= \eta_0(z)\exp\left[\frac{E_\eta(z)}{T^* + T_\eta(z)} - \frac{E_\eta(z)}{1 + T_\eta(z)} + C\ln\eta_C\right] \quad \text{(III.4)}
\end{aligned}
$$

with the non-dimensionalised temperature T^*, that is cut off between values of 0 and 1. Non-dimensionalisation is done using the reference values of $T^* = 0$ and $T^* = 1$ for the surface and the CMB temperature, respectively. The dependence on depth is implemented as steps of the viscosity prefactor η_0, the non-dimensional activation energy E_η and the non-dimensional temperature offset T_η (see Table III.2). η_C is the viscosity contrast between pile and ambient mantle due to composition, varying between 1 and 100, while C is the composition value between 0 and 1. $\eta_{\Delta T}$ is the thermal viscosity contrast and describes the maximum potential viscosity variations due to temperature in the lower mantle, which we vary in the range 2.3 to 7500.

To achieve a better comparison between parameters, all models are started from the same reference case of a fully-developed system with degree-2 structure (see Figure III.1a and Figure III.1b). We obtain this initial condition by running a model with the reference values of $B = 0.8$, $\eta_{\Delta T} = 330$ and $\eta_C = 10$ for 6.5 Gyr, starting with a 125 km thick dense basal layer (as described in Heyn et al. (2018)). This results in a pile with a volume of about 1.75 % of the mantle (approximately 77% of the original layer mass, Figure III.1b), and eliminates the topographic variations due to different pile masses. Although such a setup means that models require some time to adjust to the changed parameters, the uniform mass and volume of the initial condition enables us to expand our investigation of the effects of density and viscsoity towards pile configurations that would be unstable otherwise. To overcome the limitation of adjustment time and to get better constraints on how topography changes when plumes interact with the pile, we run our models for 2.5 Gyr.

Table III.2: Parameters defining the viscosity profiles for different thermal viscosity contrasts $\eta_{\Delta T}$. We use steps at depths of 299 km, 410 km and 660 km, for the activation energy E_η, the temperature offset T_η, and the viscosity prefactor η_0. In the table, values are sorted by increasing depth.

$\eta_{\Delta T}$	η_0				E_η				T_η			
2.3	5 /	0.5 /	2.5 /	5	1 /	1 /	1 /	1	0.02 /	0.4 /	0.6 /	0.7
65	5 /	0.5 /	2.5 /	5	1 /	1 /	1 /	1	0.02 /	0.2 /	0.2 /	0.2
330	5 /	0.5 /	2.5 /	5	1 /	1 /	1 /	1	0.02 /	0.15 /	0.15 /	0.15
1700	5 /	0.5 /	2.5 /	5	1 /	1 /	1 /	1	0.02 /	0.12 /	0.12 /	0.12
7500	5 /	0.5 /	2.5 /	5	1.2 /	1.2 /	1.2 /	1.2	0.02 /	0.12 /	0.12 /	0.12

III.3 Characteristic topography for higher intrinsic pile viscosity

For models without an elevated intrinsic pile viscosity, the CMB topography shows depressions beneath the subducting slab and beneath the dense pile, while the CMB at the pile margin is uplifted and shows strong positive topography (Figure III.1c). This reflects the general flow pattern of sinking flow beneath the slab and rising hot flow at the pile margin, with isostatic adjustment for the dense pile itself. Relative (and also absolute) topography amplitudes depend on the thermal viscosity contrast $\eta_{\Delta T}$, since increasing the temperature-dependence of viscosity makes slabs stronger and thus increases the coupling between mantle flow and the CMB. As a consequence, the depression beneath the slab gets more pronounced with increasing $\eta_{\Delta T}$, while the pile depression gets smaller. The latter is, however, more likely related to pile thickness and density than it is to viscosity (as discussed later in more detail). Increasing the pile excess density (B) or the pile viscosity (η_C) increases the pile depression, while topography beneath the slab is not affected. These observations are in good agreement with previous studies (Lassak et al., 2007, 2010; Deschamps et al., 2017) and also fit the pattern of long-wavelength CMB topography detected by body waves or normal modes (Tanaka, 2010; Soldati et al., 2012) reasonably well.

Although the long-wavelength topography is not significantly affected by the presence of a compositonal viscosity contrast (in good agreement with Deschamps et al. (2017)), we observe strong differences at shorter length scales. Figure III.2 compares the topography for a model with $B = 0.8$, $\eta_{\Delta T} = 330$ and $\eta_C = 1$ (left panels) with $\eta_C = 10$ (right panels), the former being the same parameters as for the representative long-wavelength topography in Figure III.1c. Yet, as can be seen in the topographic profile in Figure III.2 (right), the core-mantle boundary shows a clear depression next to the pile edge that is approximately 80-120 km wide (measured from the top of the plateau outside of the pile to the maximum beneath the pile edge) and a peak that marks the edge itself. We observe these features only if the pile has a higher intrinsic viscosity than the surrounding mantle (i.e. the hot thermal boundary layer), otherwise the topography near the pile margin is smooth. The amplitude of the depression (about 2-3 km) is smaller than that of the long-wavelength elevation associated with rising flow at the pile margin. Consequently, the overall topography remains positive and the depression is not visible at low spherical harmonic degrees. Neither long-wavelength nor short-scale topography are changed significantly within our resolution tests (see Figure III.2g and Figure III.2h), only the amplitudes of the small-scale topographic feature and its symmetry are slightly modified as we capture their slopes more accurately.
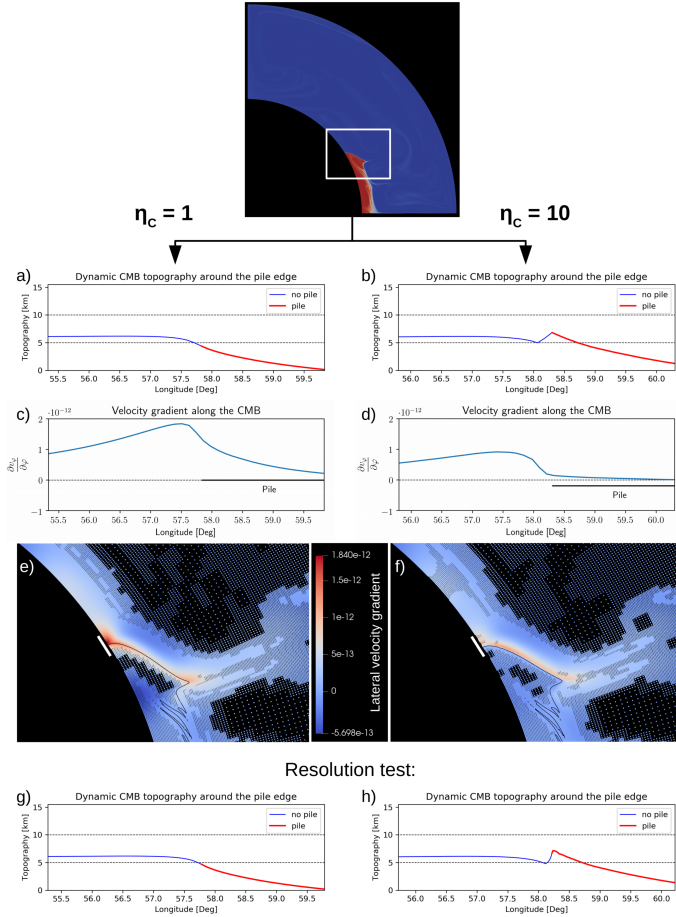
Figure III.2: CMB topography near the pile edge (panels (a),(b)) and its associated lateral velocity gradient (panels (c)-(f)) for models with $B = 0.8$, $\eta_{\Delta T} = 330$ and $\eta_C = 1$ (left) or $\eta_C = 10$ (right). The position and length of the profiles are indicated by white lines in (e) and (f). As can be seen in (b), there is a characteristic short-wavelength topography related to an increased pile viscosity. This topographic pattern is observed for all values of $\eta_C > 1$, although depth of the depression and the peak at the pile margin increase with pile viscosity. The depression is caused both by a relative uplift of the pile-edge maximum (compared to the plume-side plateau, see definitions in Figure III.3), and a wedge of TBL material that gets compressed against the pile. The latter results from the lateral gradients of the velocity component parallel to the CMB ($\frac{\partial v_\varphi}{\partial \varphi}$) shown in (c) and (d) along the CMB, and in (e) and (f) as points at cell centres. While the gradient in the left panel (case $\eta_C = 1$) spreads into the pile, a stiffer pile exhibits almost no velocity gradient. The lowermost row shows the topography obtained for the same set of parameters, but using a resolution of up to $1.4\,\mathrm{km}$ to verify that the observed topography is not an artifact of resolution. Apart from details of the slopes, there is no change in topography for our resolution test.

A reduced density of hot TBL material and uplift due to rising flow explain the long-wavelength topographic high near the pile, and thus also the local peaks of the short-scale topography. For more viscous (stiffer) piles, the uplift of the CMB is asymmetric and more pronounced beneath the pile margin due to increased coupling between the mantle and the CMB. However, the origin of the small-scale depression outside the pile margin can only be partially explained by the relative uplift of the pile margin, and is not related to density differences in the lower mantle since the material from which plumes are sourced is hot and therefore light. Yet, the distribution of lateral gradients for the velocity component parallel to the CMB ($\frac{\partial v_\varphi}{\partial \varphi}$) changes significantly in the presence of a stiff pile with $\eta_C > 1$ (compare Figure III.2c-f). While the gradient is distributed over a broad area with its maximum about 0.3 degree from the pile edge in the case of $\eta_C = 1$ (Figure III.2c), a higher pile viscosity $\eta_C = 10$ focuses the stress in a localized area just outside the pile margin, with hardly any velocity gradient within the pile itself (Figure III.2d). Consequently, compression associated with velocity gradients in lateral TBL flow becomes concentrated in a narrow area outside a high-viscosity pile, causing radial stress towards the CMB expressed as a depression.

III.4   How small-scale topography relates to the plume cycle

Since the small-scale CMB topography is caused by relative uplift of the pile margin in combination with a compressed TBL wedge, the shape and amplitude of the depression are time-dependent and react to changes in the configuration of the flow and the location of the pile edge. Figure III.3 shows the evolution of several topographic characteristics (Figure III.3 top panels) for the models discussed above (left: $B = 0.8$, $\eta_{\Delta T} = 330$ and $\eta_C = 1$, right: $B = 0.8$, $\eta_{\Delta T} = 330$ and $\eta_C = 10$) over time: (1) the maximum slab depression (dark blue line), (2) the average pile depression (excluding all elevated parts of the CMB that lie beneath the pile; light blue line), (3) the highest point outside the pile (the "plume-side plateau" (PSP); black line), (4) the lowest point next to the pile ("circum-pile depression" (CPD); green line) and (5) the highest point inside the pile ("pile-edge maximum" (PEM); red line). In case of $\eta_{C=1}$, points (4) and (5) occur at adjacent nodes of the mesh, thus the topographic difference between the two is mesh-dependent. As can be seen, the maximum slab depression does not change much with time, while the three points defining the short-wavelength depression show a quasi-periodic behavior, although slightly shifted in time for piles with increased intrinsic viscosity. This reflects the periodic generation of plumes at the pile margin, which is caused by a local collapse of the thicknened pile edge associated with a reduction of plume pull for fading or laterally moving plumes (Figure III.4). This pile collapse is also reflected in the periodicity of the average pile depression, which shows a minimum aproximately every time the pile collapses, although the amplitudes are rather small compared to variations at the pile margin (see Figure III.3 lower panels).
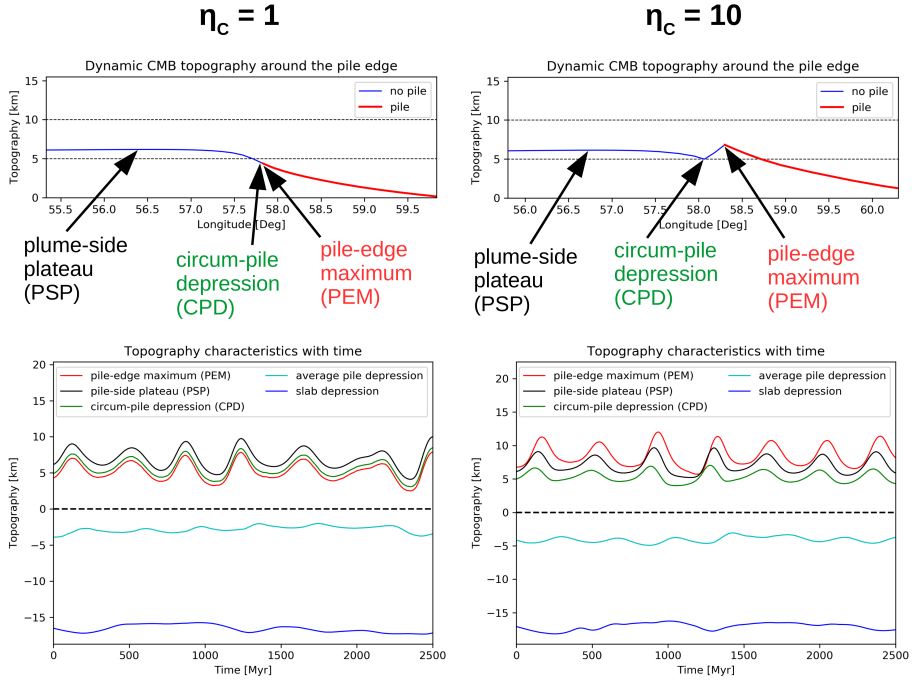
Figure III.3: CMB topography characteristics and their evolution over time for the models discussed in Figure III.2: $B = 0.8$, $\eta_{\Delta T} = 330$, $\eta_C = 1$ (left), and $B = 0.8$, $\eta_{\Delta T} = 330$, $\eta_C = 10$ (right). Note that in the case of $\eta_C = 1$ (left), there is no depression or pile-edge maximum, thus these points mark the lowest topography just outside the pile and the maximum topography inside the pile, which are adjacent gridpoints. Slab depression is the maximum depression beneath the subducted slab (usually at longitude 0) and the average pile depression describes the average of the negative CMB topography beneath the pile. The periodic behavior of the topography characteristics near the pile eedge is caused by the initiation of plumes and their interaction with the pile.

An example of how the topography around the pile margin and its associated velocity gradient evolve during a plume cycle is shown in Figure III.4. For each step, the figure is divided into the topography around the pile edge and the lateral gradient of v_ϕ (the velocity component along the CMB). Velocity gradients are calculated at the cell centres of the respective mesh and are represented as points, thus also indicating the actual mesh resolution. As mesh resolution is refined based on gradients in composition and viscosity, it allows us to identify the pile outlines and the plumes. For orientation, the outline of the pile is also indicated as black line in the velocity gradient field. When comparing the velocity gradients over time, we can clearly see that their magnitude varies significantly, while the sign is preserved throughout the whole cycle.
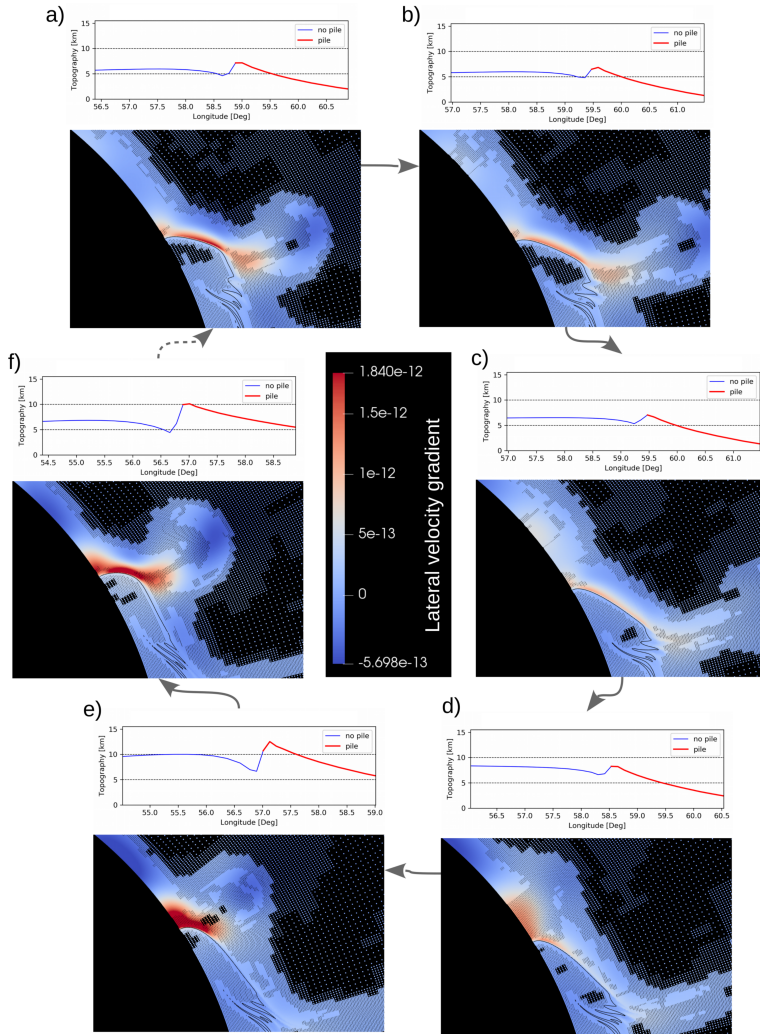
Figure III.4: CMB topography and lateral velocity gradients of v_φ during a cycle of plume initiation and growth. A plume being pushed towards the pile interior increases the local pile edge thickness, while pulling the pile margin along the TBL in flow direction, thereby reducing the lateral velocity gradient and the topographic depression (panels (a)-(c)). As soon as the upward plume pull decreases and no longer supports the thickened pile, the pile edge starts to collapse and spread along the CMB in a direction opposite to the TBL flow (panels (c) to (e)). This increases compression in the TBL wedge significantly, which amplifies CMB topography. It also thickens the the lower thermal boundary layer, triggering a new plume (e). When the plume starts to rise, the lateral pile edge motion stops, the velocity gradients and CMB topography start to decrease (f) and the cycle starts anew.

When a plume rises at the pile margin (Figure III.4a), it drags material towards the pile while compressing the pile laterally and locally increasing the pile thickness. Yet, since the stiffer pile moves much slower than the hot ambient mantle, we get a velocity gradient and thus compression at the pile edge. Part of this compressed ambient mantle material can escape upwards in the plume, but we are left with a wedge of hot mantle that is trapped against the steep pile edge. When the plume moves on towards the top of the pile (Figure III.4b-c), it excerts less drag on the hot thermal boundary layer, while the pile edge moves along the CMB in the same direction as the lateral TBL flow, and pile area is reduced. This reduces the velocity gradient and the topographic depression becomes less pronounced. The gradient then has a minimum at the time when the pile edge reaches its maximum thickness and the lateral motion of the pile margin ceases (Figure III.4c). At this time, the plume has lost its connection to the thermal boundary layer and velocity towards the pile within the TBL decreases. The smaller velocity gradient is also reflected in the topographic depression of the CMB next to the pile, which reaches a minimum in amplitude and the adjacent topographic maxima becomes more symmetric.

As the pile collapses and expands along the CMB (Figure III.4d-e), it pushes the hot TBL material against the prevailing flow along the CMB towards the pile, induced by the sinking slab, and considerably increases the velocity gradient just outside the stiff pile (Figure III.4d). As long as the plume is not fully developed (Figure III.4e), only a small portion of the compressed material can escape upwards, and a large and asymmetric depression develops outside the pile. As soon as the plume starts to rise (Figure III.4f), the lateral pile edge motion comes to a halt and the compression becomes weaker. The cycle repeats itself for every plume, and since both the symmetry and amplitude of the circum-pile depression vary along this cycle, they might be used as indicators for the current stage of the plume cycle.

III.5 The effect of varying density and viscosity contrasts

For long wavelengths, our predicted dynamic CMB topography, and its principal dependence on the viscosity structure of the lower mantle and the density of the pile, agree well with previous studies (e.g., Lassak et al., 2007, 2010; Deschamps et al., 2017). Yet, since a higher value of $\eta_{\Delta T}$ in our models does not reduce the TBL viscosity (Section III.2), the elevation of the CMB associated with rising flow is not reduced either. Implications of this are further discussed later.

In the following section, we focus on the characteristic short-wavelength topography at pile margins. Since this characteristic CMB topography is superimposed on the long-wavelength component, we use relative topography between the three characteristic points (Figure III.3) to characterize our observations as a function of pile and TBL properties. Apart from determining whether there is a valley-shaped circum-pile depression or not, the lowermost mantle viscosity structure and pile density are expected to have different effects

on the depth and symmetry of the characteristic topography, since they influence different parts of the topographic pattern. Thus, observations of this topography (e.g., from seismology) could place useful constraints on these viscosity variations.

III.5.1 Time-averaged topography

The compositional viscosity contrast η_C has a strong impact on relative topography, both in terms of the depth of the depression and the asymmetry of the peaks. The latter (Figure III.5e-f) can be explained by increased coupling between the stiff pile and the CMB for larger values of η_C, which is reflected in larger topography beneath the pile (Lassak et al., 2007, 2010; Deschamps et al., 2017). Increased uplift of the pile margin also (partially) explains the increasing depth of the depression relative to the pile-edge maximum (Figure III.5a-b), but cannot account for its increased depth relative to the plume-side plateau (Figure III.5c-d). A stiffer pile focuses more of the lateral velocity gradient in the compressed TBL wedge, increasing the stresses there. This clearly shows that the depression is indeed affected by compression of the TBL wedge next to the pile margin. Relative topography values close to zero in Figure III.5a-b or negative values in Figure III.5e-f show the absence of the characteristic topography for piles that are not more viscous than their surroundings. By contrast, the plume-side plateau is always more elevated than the "depression" (compare Figure III.3 left panels).

The effect of thermal viscosity contrasts is a bit more ambiguous than that of η_C. As can be seen in Figure III.5 (left), increased temperature-dependence $\eta_{\Delta T}$ (indicated by line color) reduces the depth of the depression (Figure III.5a and Figure III.5c), and makes the structure more symmetric by reducing the elevation difference between the two topographic maxima (Figure III.5e). Yet, changes are minor compared to the influence of the pile viscosity (η_C, x-axis). The observed decrease in relative topography between the characteristic points of the short-scale topography can be attributed to an increase in plume strength caused by fewer plumes forming in a given time period for increasing $\eta_{\Delta T}$. The less frequently that plumes are inititated, the more time the lower thermal boundary layer has to grow between plumes, and the stronger the resulting plumes are. This effect is strongest outside the pile (plume-side plateau and depression), since stronger plumes also increase the pile edge thickness more, which partly compensates the increased pull upwards (via isostatic compensation).

Increasing the pile density generally reduces the elevation of the CMB beneath the pile. This is expressed in the reduced relative topography between pile-edge maximum and plume-side plateau (Figure III.5f), making these topographic features more symmetric. Yet, the difference between the pile-edge maximum and the depression (Figure III.5b) is hardly affected, indicating that the depression must become deeper (which it does relative to the plume-side plateau, see Figure III.5d). Thus, a denser pile focuses stresses in a wedge of TBL material next to the pile margin. This is similar to the behavior of a stiffer pile, although smaller in amplitude.
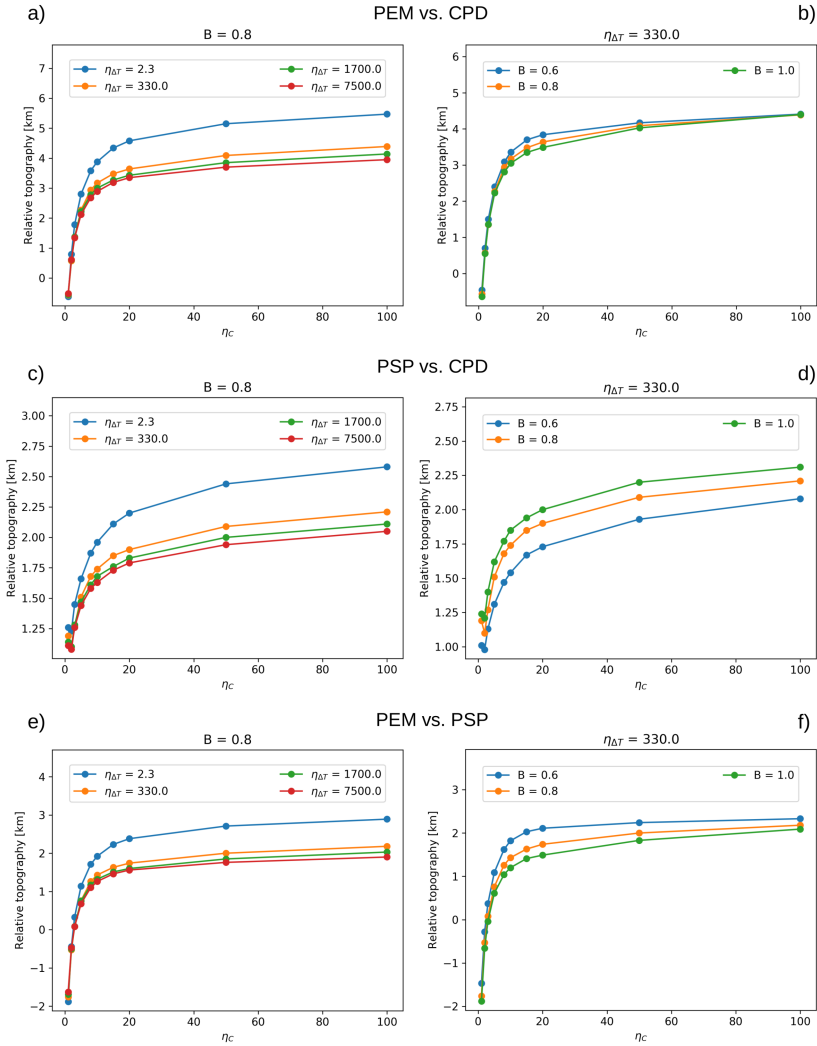
Figure III.5: Time-averaged relative topography between different points defining the characteristic topography at the pile margin as a function of η_C and $\eta_{\Delta T}$ for $B = 0.8$ (left) or B for $\eta_{\Delta T} = 330$ (right). Relative topographies between the pile-edge maximum (PEM) and the circum-pile depression (CPD) (a)-(b) and the two maxima (PEM and PSP) (e)-(f) increase with increasing η_C, while both $\eta_{\Delta T}$ and B play minor roles. Negative topography values indicate the absence of the depression (compare Figure III.3, left panels). The increase in relative topography between the plume-side plateau (PSP) and the circum-pile depression with increasing η_C (second row, panels (c)-(d)) reflects a stronger focusing of stresses into the compressed TBL wedge. Due to the definition of these characteristic points (Figure III.3), the relative topography never reaches zero.

109

III.5.2   Topography variations during the plume cycle

As shown in Figure III.4, the symmetry and depth of the characteristic depression vary significantly during the plume cycle. Similar to the time-average topography discussed above, amplitudes of this periodic change associated with plume initiation, i.e. respective minima and maxima of differential topography between the three characteristic points, depends on B, η_C and $\eta_{\Delta T}$ (Figure III.6). In order to quantify these variations within the plume cycle, we calculate the minima and maxima of relative topography within each cycle of initiation and fading of plumes, and average the obtained values by the number of observed plume cycles. Yet, note that the topographic maxima and minima between different points do not necessarily occur at the same time within the plume cycle, but may be slightly delayed relative to each other (compare Figure III.3).
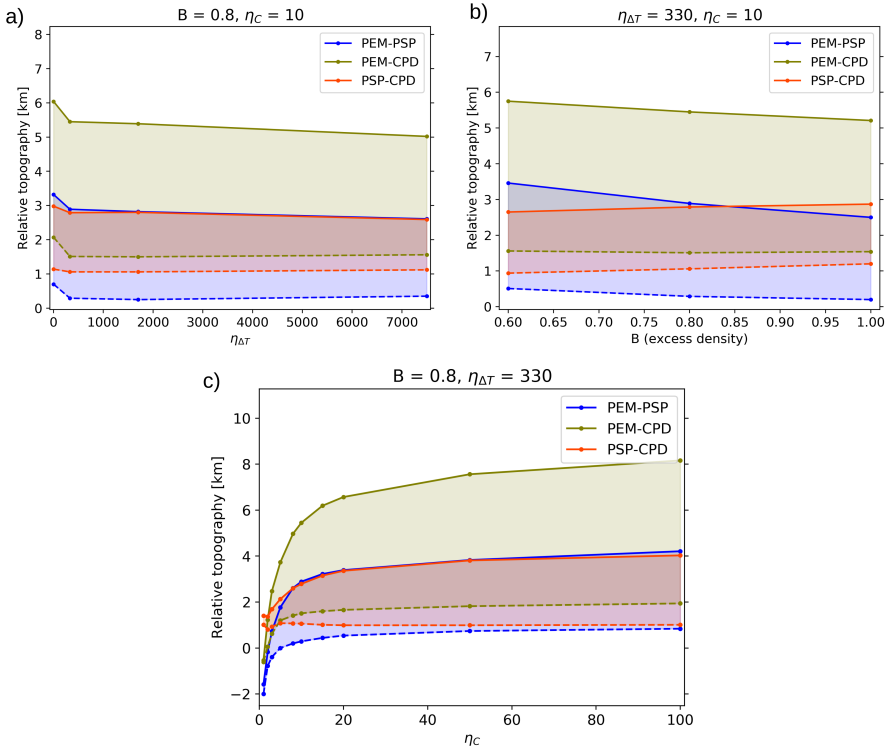

Figure III.6: Average variations of relative topography during the plume cycle as a function of the thermal viscosity contrast $\eta_{\Delta T}$ (a), the pile density B (b) and the compositional viscosity contrast η_C (c), while the other parameters are fixed as indicated. Abbreviations are: PSP = plume-side plateau, PEM = pile-edge maximum, and CPD = circum-pile depression. Colored dashed and solid lines indicate the average minima and maxima (respectively) of relative topography between the respective characteristic points during the plume cycle (see text for more details).

As we found for the average topography, neither the thermal viscosity contrast (Figure III.6a) nor the pile density (Figure III.6b) have any significant impact on the minima and maxima of relative topography during the plume cycle. Both an increase in B or $\eta_{\Delta T}$ tend to reduce the maximum relative topography, and thus the overall range of variations, while minima are less affected. For $\eta_{\Delta T}$, this reflects the effect of increased plume strength, which is more pronounced outside the dense pile, while an increased pile density B damps the motion of the pile-edge maximum. Since the plume-side plateau and the circum-pile depression are in both cases affected in the same way, the range of differential topography between these points is almost constant.

In contrast, η_C significantly increases the variations of all three relative topographies, with the strongest increase observed for the relative topography between pile-edge maximum and the circum-pile depression (Figure III.6c, olive lines (PEM-CPD)). This combines the effect of larger stress variations in the TBL wedge for stiffer piles due to increased focusing of stresses (plume-side plateau vs depression, Figure III.6c orange lines (PSP-CPD)), with a higher mobility of the pile-edge maximum caused by a stronger coupling between mantle flow and the CMB beneath the pile (pile-edge maximum vs plume-side plateau, Figure III.6c blue lines (PEM-PSP)). As a consequence, a stronger compositional viscosity contrast considerably increases the variations in depth and asymmetry of the characteristic short-scale topography, while pile density and thermal viscosity contrasts are negligible.

III.6 Discussion

III.6.1 Observations of CMB topography

Up to now, there have been few seismic observations of short-scale core-mantle boundary topography, but the number has been increasing in recent years due to improvements in equipment and methodology (Restivo & Helffrich, 2006; Wu et al., 2014; Gassner et al., 2015; Schlaphorst et al., 2015; Mancinelli & Shearer, 2016; Shen et al., 2016). Schlaphorst et al. (2015) give an overview of studies using body waves to investigate CMB topography, most of which investigate length scales of about 100-1000 km, and their resulting topography magnitudes. The shortage of observations of small-scale topography and the large variability in patterns and magnitudes of current CMB topography maps are caused by several factors: (1) the resolution of body waves and especially normal mode data limits most methods to topography length scales of > 100 km (Koelemeijer et al., 2012; Soldati et al., 2013; Schlaphorst et al., 2015), although there are a few studies that infer smaller wavelengths based on PKP and PKKP precursors (see e.g., Schlaphorst et al., 2015; Mancinelli & Shearer, 2016, and references therein); (2) there is a trade-off in normal mode or traveltime data between topography and other parameters such as density above and below the CMB or the seismic velocity structure, which makes interpretation of data non-unique (Steinberger & Holme, 2008; Koelemeijer et al., 2012); (3) for

core-reflected waves (e.g. PcP and ScP), which have a maximum resolution of about 100 km, both data processing, data quality and available source-receiver combinations limit the applications (Colombi et al., 2014; Wu et al., 2014; Shen et al., 2016). With the current methods, core diffracted waves, such as P_{diff} can be even more problematic and may not be useful to investigate CMB topography of short- to intermediate length scales (Colombi et al., 2014). As a consequence, we currently have only limited long-wavelength data (Tanaka, 2010; Soldati et al., 2012) and a few regional studies (Wu et al., 2014; Gassner et al., 2015; Schlaphorst et al., 2015; Shen et al., 2016). Although there is no systematic study of CMB topography around or beneath the LLSVP structures to which we could compare our predictions, advances in seismic data coverage may provide the basis for a more detailed CMB topography in the future.

The length scale of approximately 80-120 km for our predicted topography is comparable to the maximum lateral resolution of about 100 km obtained for core-reflected waves, such as ScP and PcP (Wu et al., 2014; Schlaphorst et al., 2015; Shen et al., 2016). Yet, focusing/ defocusing effects of CMB depressions/ elevations on core-reflected waves may enable us to detect topography on even slightly smaller topographic length scales of about 60 km (Wu et al., 2014; Shen et al., 2016). Applying this method to Earth, Wu et al. (2014) and Shen et al. (2016) have detected topography with length scales between 140 and 350 km and amplitudes up to 6 km beneath Alaska and Japan. Moreover, Mancinelli and Shearer (2016) recently used scattered energy to infer globally random core-mantle boundary topography of about 400 m amplitude and lateral scales down to about 7 km, which would be sufficient to investigate structures of the length scales predicted by our models. However, data processing of this type of signal is still in its early stages, making a direct comparison to observations currently unfeasible (Mancinelli & Shearer, 2016), but potentially possible in the future.

III.6.2 Model limitations

Taking into account differences in our viscosity law, our results for long-wavelenth topography agree well with previous studies (Lassak et al., 2007, 2010; Deschamps et al., 2017; Deschamps & Li, 2019) with respect to the dependence of long-wavelength CMB topography on viscosity contrasts and density. However, because our viscosity law does not modify the lowest viscosity for increasing temperature dependence, we can indentify additional effects of plume strength on topography, which are otherwise masked by the dominant effect of viscosity reduction. In our models, the change in thermal viscosity contrast is implemented as a strong increase in viscosity for cold material, which affects topographic amplitudes at long wavelengths compared to Deschamps et al. (2017). Thus, we may over- or underestimate some amplitudes, while the background topographic pattern at long-wavelengths, and the structure and time-dependence of the short-scale topography, should be robust.

It has been shown that the presence of post-bridgmanite with a viscosity 3-4 orders of magnitude below that of bridgmanite (Ammann et al., 2010) can reduce the depression induced by the sinking slab considerably (Yoshida, 2008; Deschamps & Li, 2019). This effect may be necessary to make geodynamic predictions consistent with the CMB topography amplitudes inferred from seismology (Yoshida, 2008; Soldati et al., 2013), which vary between a few hundered meters to a few kilometers (e.g., Tanaka, 2010; Soldati et al., 2012; Wu et al., 2014; Schlaphorst et al., 2015). For the short-wavelength topography, the effect of weak post-bridgmanite should depend on its distribution. If post-bridgmanite is stable only in cold areas, i.e. subducted slabs (Torsvik et al., 2016), our observed topographic pattern may become more asymmetric due to a viscosity decrease outside the pile and a stronger focusing of stresses into the TBL wedge. Such a scenario would correspond to an increase in the compositional viscosity contrast in our models. In case post-bridgmanite is also present in hotter parts of the deep mantle, including the tops of the thermochemical piles (Koelemeijer et al., 2018), we do not expect any significant effect on the symmetry or relative amplitudes of the characteristic topographic feature since the viscosity reduction would affect both the pile interior and the ambient mantle.

Our use of a uniform starting model with a fully-developed pile for all different combinations of parameters B, $\eta_{\Delta T}$ and η_C has several implications. As pointed out above, models need about 50-200 Myr to adjust to the modified condition, including changes in pile morphology (thickness and CMB area coverage) and the plume cycle. As a consequence, relative topography amplitudes adjust as well, while the general topographic pattern does not change during the adjustment time. Since we take averages over 2.5 Gyr, including several plume cycles with natural variations in themselves, this adjustment time does not significantly influence our conclusions. However, this kind of setup enables us to ignore the potential effect of a variable and rather unconstrained pile density and viscosity that we would get as an initial condition after pile formation with different parameters. Different stages of mixing between the dense pile and the ambient mantle, as observed for various stable to metastable piles (see Heyn et al. (2018)), can have a significant impact on actual pile properties and therefore topgraphy. Although the general topographic pattern is not expected to change, uncertainties in pile density and viscosity due to heterogeneities (especially along the pile boundary) may make observations more difficult to interpret.

III.6.3 Manifestation on Earth

Since our models are 2-D, they do not account for 3-D effects, for example an uneven distribution of plumes and non-uniform lateral TBL flow around the pile margins. Both factors will affect the symmetry and the amplitude of the topographic features along the LLSVP margin, similar to the variations observed during the plume cycle. A weak lateral flow and/or the absence of a plume will result in a small and more symmetric depression at the respective parts of the pile margins, while the feature will be more pronounced at the base of initiating

plumes. Yet, as long as there is lateral TBL flow towards the piles, a pile with higher intrinsic viscosity should focus stresses into a compressed TBL wedge and thus be surrounded by a topographic depression.

Accumulation of stresses at sharp rheological boundaries, as we observe for thermochemical piles with high intrinsic viscosity, may also play a role at the Earth's surface. Rolf and Tackley (2011) studied the influence of continents, or more specifically stiff and stable cratons, on subduction and plate behavior. Their results show that the presence of sharp viscosity gradients at craton margins focuses stresses and facilitates plate yielding and thus subduction initiation. Although Rolf and Tackley (2011) did not convert these stresses to topography, the underlying process is the same, showing its importance for convective dynamics in different parts of the mantle system. In both cases, the overall topography is likely dominated by flow-related longer-wavelength processes, which may render it difficult to detect features related to compositional viscosity differences. While geological complexities such as subduction and crust complicate any topographic expression of circum-cratonic stress, the overall structure of the lowermost mantle should be simpler, despite the presence of ultra-low velocity zones (ULVZs, McNamara, 2019). Thus, we would expect to observe a valley with variable depth around the periphery of the LLSVPs if they are indeed thermochemical piles with elevated viscosity.

Patches of ultra-low velocity zones (ULVZs) have been detected seismically, and seem to be associated with LLSVPs, potentially clustering predominantly at pile margins and plume roots (see e.g., review by McNamara, 2019). As for LLSVPs, neither the origin nor the properties (density, viscosity) of these ULVZ patches are known. Consequently, it is difficult to estimate their effect on our predicted short-scale topography. ULVZs may deepen the circum-pile depression, or prevent its formation, depending on their viscosity and density structure. Furthermore, the depression may help to focus and localize the ULVZ material into distinct patches, keeping most of the material trapped along the margins of the LLSVPs. Yet, independent of the influence of ULVZs on the short-scale CMB topography, we may be able to detect the circum-pile depression in areas where no ULVZ has been observed.

III.7   Conclusions

Our high resolution thermochemical convection models predict a characteristic short-wavelength topographic depression of about 80-120 km width surrounding the LLSVPs. The depth of this depression depends on the compositional viscosity contrast between the ambient mantle and the pile. Rising plume flow pulls the CMB around the pile margin upwards, and this effect is more pronounced beneath a high-viscosity pile ($\eta_C > 1$) due to increased coupling between mantle flow and the boundary. This causes relative uplift of the pile-edge maximum compared to the plume-side plateau. Moreover, a wedge of TBL material

becomes compressed against a stiff pile and pushes the CMB downwards around the pile edge.

Since the relative amplitude of the depression is small (about 2-4 km in amplitude and 80-120 km wide), this feature is invisible in long-wavelength topography of the CMB and requires high-resolution seismic data to be detected. Yet, if it can be observed, the valley would strongly indicate the presence of a compositonal viscosity contrast between the LLSVPs and the ambient mantle. The size and symmetry of this topographic structure impose further constraints on the magnitude of compositonal viscosity increase, and, to a smaller extent, also on the thermal viscosity contrasts and pile density. The larger the viscosity contrast between pile and mantle, the more pronounced and asymmetric this topography becomes, while increased density or a higher thermal viscosity contrast have the opposite (although considerably smaller) effect. However, the amplitude of relative topography also responds to the (periodic) generation of plumes at the pile edge, with the most prominent (and asymmetric) depression being observed at the time of plume initiation. Consequently, short-scale dynamic topography may help to identify regions of active plume generation.

References

Ammann, M. W., Brodholt, J. P., Wookey, J., & Dobson, D. P. (2010, May). First-principles constraints on diffusion in lower-mantle minerals and a weak d layer. *Nature*, *465*, 462–465. Retrieved from `https://www.nature.com/articles/nature09052#supplementary-information` doi: 10.1038/nature09052; 10.1038/nature09052

Austermann, J., Kaye, B. T., Mitrovica, J. X., & Huybers, P. (2014, 01). A statistical analysis of the correlation between large igneous provinces and lower mantle seismic structure. *Geophysical Journal International*,

197(1), 1–9. Retrieved from `https://doi.org/10.1093/gji/ggt500` doi: 10.1093/gji/ggt500

Ballmer, M. D., Schumacher, L., Lekic, V., Thomas, C., & Ito, G. (2016). Compositional layering within the large low shear-wave velocity provinces in the lower mantle. *Geochemistry, Geophysics, Geosystems*, *17*(12), 5056–5077. Retrieved from `https://agupubs.onlinelibrary.wiley.com/doi/abs/10.1002/2016GC006605` doi: 10.1002/2016GC006605

Bangerth, W., Dannberg, J., Gassmoeller, R., Heister, T., et al. (2018, June). *ASPECT v2.0.1 [software].* Davis, CA. Retrieved from `https://doi.org/10.5281/zenodo.1297145` doi: 10.5281/zenodo.1297145

Bangerth, W., Dannberg, J., Gassmöller, R., Heister, T., et al. (2019, April). ASPECT: Advanced solver for problems in earth's convection, user manual. Retrieved from `https://doi.org/10.6084/m9.figshare.4865333` (doi:10.6084/m9.figshare.4865333) doi: 10.6084/m9.figshare.4865333

Burmann, F., & Noir, J. (2018). Effects of bottom topography on the spin-up in a cylinder. *Physics of Fluids*, *30*(10), 106601. Retrieved from `https://doi.org/10.1063/1.5051111` doi: 10.1063/1.5051111

Colombi, A., Nissen-Meyer, T., Boschi, L., & Giardini, D. (2014, 04). Seismic waveform inversion for core–mantle boundary topography. *Geophysical Journal International*, *198*(1), 55–71. Retrieved from `https://doi.org/10.1093/gji/ggu112` doi: 10.1093/gji/ggu112

Conrad, C. P., Steinberger, B., & Torsvik, T. H. (2013, June). Stability of active mantle upwelling revealed by net characteristics of plate tectonics. *Nature*, *498*, 479–482. Retrieved from `https://www.nature.com/articles/nature12203#supplementary-information` doi: 10.1038/nature12203; 10.1038/nature12203

Cottaar, S., & Lekic, V. (2016, 08). Morphology of seismically slow lower-mantle structures. *Geophysical Journal International*, *207*(2), 1122–1136. Retrieved from `https://doi.org/10.1093/gji/ggw324` doi: 10.1093/gji/ggw324

Davies, D. R., Goes, S., Davies, J., Schuberth, B., Bunge, H.-P., & Ritsema, J. (2012). Reconciling dynamic and seismic models of earth's lower mantle: The dominant role of thermal heterogeneity. *Earth and Planetary Science Letters*, *353-354*, 253–269. Retrieved from `http://www.sciencedirect.com/science/article/pii/S0012821X1200444X` doi: 10.1016/j.epsl.2012.08.016

Deschamps, F., & Li, Y. (2019). Core-mantle boundary dynamic topography: Influence of postperovskite viscosity. *Journal of Geophysical Research: Solid Earth*, *124*(8), 9247–9264. Retrieved from `https://agupubs.onlinelibrary.wiley.com/doi/abs/10.1029/2019JB017859` doi: 10.1029/2019JB017859

Deschamps, F., Rogister, Y., & Tackley, P. J. (2017, 09). Constraints on core–mantle boundary topography from models of thermal and thermochemical convection. *Geophysical Journal International*, *212*(1), 164–188. Retrieved from `https://doi.org/10.1093/gji/ggx402` doi: 10.1093/gji/ggx402

Ding, H., & Chao, B. F. (2018). A 6-year westward rotary motion in the earth: Detection and possible micg coupling mechanism. *Earth and Planetary Science Letters*, *495*, 50–55. Retrieved from `http://www.sciencedirect.com/science/article/pii/S0012821X18302802` doi: 10.1016/j.epsl.2018.05.009

Doubrovine, P. V., Steinberger, B., & Torsvik, T. H. (2016). A failure to reject: Testing the correlation between large igneous provinces and deep mantle structures with edf statistics. *Geochemistry, Geophysics, Geosystems*, *17*(3), 1130–1163. Retrieved from `https://agupubs.onlinelibrary.wiley.com/doi/abs/10.1002/2015GC006044` doi: 10.1002/2015GC006044

Dziewonski, A. M., & Anderson, D. L. (1981). Preliminary reference earth model. *Physics of the Earth and Planetary Interiors*, *25*(4), 297–356. Retrieved from `http://www.sciencedirect.com/science/article/pii/0031920181900467` doi: 10.1016/0031-9201(81)90046-7

Dziewonski, A. M., Lekic, V., & Romanowicz, B. A. (2010). Mantle anchor structure: An argument for bottom up tectonics. *Earth and Planetary Science Letters*, *299*(1), 69–79. Retrieved from `http://www.sciencedirect.com/science/article/pii/S0012821X10005236` doi: 10.1016/j.epsl.2010.08.013

Gassner, A., Thomas, C., Krüger, F., & Weber, M. (2015). Probing the core–mantle boundary beneath europe and western eurasia: A detailed study using pcp. *Physics of the Earth and Planetary Interiors*, *246*, 9–24. Retrieved from `http://www.sciencedirect.com/science/article/pii/S0031920115000965` doi: 10.1016/j.pepi.2015.06.007

Glane, S., & Buffett, B. (2018). Enhanced core-mantle coupling due to stratification at the top of the core. *Frontiers in Earth Science*, *6*, 171. Retrieved from `https://www.frontiersin.org/article/10.3389/feart.2018.00171` doi: 10.3389/feart.2018.00171

He, Y., Puckett, E. G., & Billen, M. I. (2017). A discontinuous Galerkin method with a bound preserving limiter for the advection of non-diffusive fields in solid earth geodynamics. *Physics of the Earth and Planetary Interiors*, *263*, 23–37. Retrieved from `https://doi.org/10.1016/j.pepi.2016.12.001` doi: 10.1016/j.pepi.2016.12.001

Heister, T., Dannberg, J., Gassmöller, R., & Bangerth, W. (2017). High accuracy mantle convection simulation through modern numerical methods. II: Realistic models and problems. *Geophysical Journal International*, *210*(2), 833–851. Retrieved from `https://doi.org/10.1093/gji/ggx195` doi: 10.1093/gji/ggx195

Heyn, B. H., Conrad, C. P., & Trønnes, R. G. (2018). Stabilizing effect of compositional viscosity contrasts on thermochemical piles. *Geophysical Research Letters*, *45*(15), 7523–7532. Retrieved from `https://agupubs.onlinelibrary.wiley.com/doi/abs/10.1029/2018GL078799` doi: 10.1029/2018GL078799

Koelemeijer, P. J., Deuss, A., & Ritsema, J. (2017, May). Density structure of earth's lowermost mantle from stoneley mode splitting observations. *Nature Communications*, *8*, 15241. Retrieved from `https://www.nature`

.com/articles/ncomms15241#supplementary-information   doi: 10.1038/ncomms15241; 10.1038/ncomms15241

Koelemeijer, P. J., Deuss, A., & Trampert, J. (2012, 07). Normal mode sensitivity to earth's d layer and topography on the core-mantle boundary: what we can and cannot see. *Geophysical Journal International*, *190*(1), 553–568. Retrieved from https://doi.org/10.1111/j.1365-246X.2012.05499 .x doi: 10.1111/j.1365-246X.2012.05499.x

Koelemeijer, P. J., Schuberth, B., Davies, D., Deuss, A., & Ritsema, J. (2018). Constraints on the presence of post-perovskite in earth's lowermost mantle from tomographic-geodynamic model comparisons. *Earth and Planetary Science Letters*, *494*, 226–238. Retrieved from http://www.sciencedirect.com/science/article/pii/ S0012821X18302656 doi: 10.1016/j.epsl.2018.04.056

Kronbichler, M., Heister, T., & Bangerth, W. (2012). High accuracy mantle convection simulation through modern numerical methods. *Geophysical Journal International*, *191*, 12–29. Retrieved from http://dx.doi .org/10.1111/j.1365-246X.2012.05609.x doi: 10.1111/j.1365-246X.2012.05609.x

Lassak, T. M., McNamara, A. K., Garnero, E. J., & Zhong, S. (2010). Core–mantle boundary topography as a possible constraint on lower mantle chemistry and dynamics. *Earth and Planetary Science Letters*, *289*(1), 232–241. Retrieved from http://www.sciencedirect.com/science/ article/pii/S0012821X09006591 doi: 10.1016/j.epsl.2009.11.012

Lassak, T. M., McNamara, A. K., & Zhong, S. (2007). Influence of thermochemical piles on topography at earth's core–mantle boundary. *Earth and Planetary Science Letters*, *261*(3), 443–455. Retrieved from http://www.sciencedirect.com/science/article/pii/ S0012821X07004499 doi: 10.1016/j.epsl.2007.07.015

Lau, H. C. P., Mitrovica, J. X., Davis, J. L., Tromp, J., Yang, H.-Y., & Al-Attar, D. (2017, November). Tidal tomography constrains earth's deep-mantle buoyancy. *Nature*, *551*, 321–326. doi: 10.1038/nature24452; 10.1038/nature24452

Le Mouël, J. L., Narteau, C., Greff-Lefftz, M., & Holschneider, M. (2006). Dissipation at the core-mantle boundary on a small-scale topography. *Journal of Geophysical Research: Solid Earth*, *111*(B4). Retrieved from https://agupubs.onlinelibrary.wiley.com/doi/abs/ 10.1029/2005JB003846 doi: 10.1029/2005JB003846

Li, M., & McNamara, A. K. (2013). The difficulty for subducted oceanic crust to accumulate at the earth's core-mantle boundary. *Journal of Geophysical Research: Solid Earth*, *118*(4), 1807–1816. Retrieved from https://agupubs.onlinelibrary.wiley.com/doi/abs/ 10.1002/jgrb.50156 doi: 10.1002/jgrb.50156

Li, Y., Deschamps, F., & Tackley, P. J. (2014, 09). The stability and structure of primordial reservoirs in the lower mantle: insights from models of thermochemical convection in three-dimensional spherical geometry. *Geophysical Journal International*, *199*(2), 914–930. Retrieved from

`https://doi.org/10.1093/gji/ggu295` doi: 10.1093/gji/ggu295

Mancinelli, N., & Shearer, P. (2016). Scattered energy from a rough core-mantle boundary modeled by a monte carlo seismic particle method: Application to pkkp precursors. *Geophysical Research Letters*, *43*(15), 7963–7972. Retrieved from `https://agupubs.onlinelibrary.wiley.com/doi/abs/10.1002/2016GL070286` doi: 10.1002/2016GL070286

McNamara, A. K. (2019). A review of large low shear velocity provinces and ultra low velocity zones. *Tectonophysics*, *760*, 199–220. Retrieved from `http://www.sciencedirect.com/science/article/pii/S0040195118301586` (Linking Plate Tectonics and Volcanism to Deep Earth Dynamics – a tribute to Trond H. Torsvik) doi: 10.1016/j.tecto.2018.04.015

McNamara, A. K., & Zhong, S. (2004). Thermochemical structures within a spherical mantle: Superplumes or piles? *Journal of Geophysical Research: Solid Earth*, *109*(B7). Retrieved from `https://agupubs.onlinelibrary.wiley.com/doi/abs/10.1029/2003JB002847` doi: 10.1029/2003JB002847

Mulyukova, E., Steinberger, B., Dabrowski, M., & Sobolev, S. V. (2015). Survival of llsvps for billions of years in a vigorously convecting mantle: Replenishment and destruction of chemical anomaly. *Journal of Geophysical Research: Solid Earth*, *120*(5), 3824–3847. Retrieved from `https://agupubs.onlinelibrary.wiley.com/doi/abs/10.1002/2014JB011688` doi: 10.1002/2014JB011688

Restivo, A., & Helffrich, G. (2006). Core–mantle boundary structure investigated using sks and skks polarization anomalies. *Geophysical Journal International*, *165*(1), 288–302. Retrieved from `https://onlinelibrary.wiley.com/doi/abs/10.1111/j.1365-246X.2006.02901.x` doi: 10.1111/j.1365-246X.2006.02901.x

Roberts, P. H., & Aurnou, J. M. (2012). On the theory of core-mantle coupling. *Geophysical & Astrophysical Fluid Dynamics*, *106*(2), 157–230. Retrieved from `https://doi.org/10.1080/03091929.2011.589028` doi: 10.1080/03091929.2011.589028

Rolf, T., & Tackley, P. J. (2011). Focussing of stress by continents in 3d spherical mantle convection with self-consistent plate tectonics. *Geophysical Research Letters*, *38*(18). Retrieved from `https://agupubs.onlinelibrary.wiley.com/doi/abs/10.1029/2011GL048677` doi: 10.1029/2011GL048677

Schlaphorst, D., Thomas, C., Holme, R., & Abreu, R. (2015, 12). Investigation of core–mantle boundary topography and lowermost mantle with p4kp waves. *Geophysical Journal International*, *204*(2), 1060–1071. Retrieved from `https://doi.org/10.1093/gji/ggv496` doi: 10.1093/gji/ggv496

Schuberth, B. S. A., Zaroli, C., & Nolet, G. (2012, 03). Synthetic seismograms for a synthetic earth: long-period p- and s-wave traveltime variations can be explained by temperature alone. *Geophysical Journal International*, *188*(3), 1393–1412. Retrieved from `https://doi.org/10.1111/j.1365-246X.2011.05333.x` doi: 10.1111/j.1365-246X.2011.05333.x

Shen, Z., Ni, S., Wu, W., & Sun, D. (2016). Short period scp phase amplitude calculations for core–mantle boundary with intermediate scale topography. *Physics of the Earth and Planetary Interiors*, *253*, 64–73. Retrieved from http://www.sciencedirect.com/science/article/pii/S0031920116000200 doi: 10.1016/j.pepi.2016.02.002

Soldati, G., Boschi, L., & Forte, A. M. (2012, 05). Tomography of core–mantle boundary and lowermost mantle coupled by geodynamics. *Geophysical Journal International*, *189*(2), 730–746. Retrieved from https://doi.org/10.1111/j.1365-246X.2012.05413.x doi: 10.1111/j.1365-246X.2012.05413.x

Soldati, G., Koelemeijer, P., Boschi, L., & Deuss, A. (2013). Constraints on core-mantle boundary topography from normal mode splitting. *Geochemistry, Geophysics, Geosystems*, *14*(5), 1333–1342. Retrieved from https://agupubs.onlinelibrary.wiley.com/doi/abs/10.1002/ggge.20115 doi: 10.1002/ggge.20115

Steinberger, B., & Holme, R. (2008). Mantle flow models with core-mantle boundary constraints and chemical heterogeneities in the lowermost mantle. *Journal of Geophysical Research: Solid Earth*, *113*(B5). Retrieved from https://agupubs.onlinelibrary.wiley.com/doi/abs/10.1029/2007JB005080 doi: 10.1029/2007JB005080

Steinberger, B., & Torsvik, T. H. (2012). A geodynamic model of plumes from the margins of large low shear velocity provinces. *Geochemistry, Geophysics, Geosystems*, *13*(1). Retrieved from https://agupubs.onlinelibrary.wiley.com/doi/abs/10.1029/2011GC003808 doi: 10.1029/2011GC003808

Tackley, P. J. (2012). Dynamics and evolution of the deep mantle resulting from thermal, chemical, phase and melting effects. *Earth-Science Reviews*, *110*(1), 1–25. Retrieved from http://www.sciencedirect.com/science/article/pii/S0012825211001486 doi: 10.1016/j.earscirev.2011.10.001

Tanaka, S. (2010). Constraints on the core-mantle boundary topography from p4kp-pcp differential travel times. *Journal of Geophysical Research: Solid Earth*, *115*(B4). Retrieved from https://agupubs.onlinelibrary.wiley.com/doi/abs/10.1029/2009JB006563 doi: 10.1029/2009JB006563

Torsvik, T. H., Steinberger, B., Ashwal, L. D., Doubrovine, P. V., & Trønnes, R. G. (2016). Earth evolution and dynamics—a tribute to kevin burke. *Canadian Journal of Earth Sciences*, *53*(11), 1073–1087. Retrieved from https://doi.org/10.1139/cjes-2015-0228 doi: 10.1139/cjes-2015-0228

Trønnes, R. G., Baron, M., Eigenmann, K., Guren, M., Heyn, B., Løken, A., & Mohn, C. (2019). Core formation, mantle differentiation and core-mantle interaction within earth and the terrestrial planets. *Tectonophysics*, *760*, 165–198. Retrieved from http://www.sciencedirect.com/science/article/pii/S0040195118303494 (Linking Plate Tectonics and Volcanism to Deep Earth Dynamics – a tribute to Trond H. Torsvik) doi:

10.1016/j.tecto.2018.10.021

Williams, C. D., Li, M., McNamara, A. K., Garnero, E. J., & van Soest, M. C. (2015, November). Episodic entrainment of deep primordial mantle material into ocean island basalts. *Nature Communications*, *6*, 8937. Retrieved from `https://www.nature.com/articles/ncomms9937#supplementary-information` doi: 10.1038/ncomms9937; 10.1038/ncomms9937

Wu, W., Ni, S., & Shen, Z. (2014). Constraining the short scale core–mantle boundary topography beneath kenai peninsula (alaska) with amplitudes of core-reflected pcp wave. *Physics of the Earth and Planetary Interiors*, *236*, 60–68. Retrieved from `http://www.sciencedirect.com/science/article/pii/S0031920114002003` doi: 10.1016/j.pepi.2014.09.001

Yoshida, M. (2008). Core-mantle boundary topography estimated from numerical simulations of instantaneous mantle flow. *Geochemistry, Geophysics, Geosystems*, *9*(7). Retrieved from `https://agupubs.onlinelibrary.wiley.com/doi/abs/10.1029/2008GC002008` doi: 10.1029/2008GC002008

Appendices

Appendix A

Supporting Information for Paper I

Contents

1. Text S1 to S2

2. Figure S1 to S2

3. Tables S1 to S2

Introduction

This supporting information provides a discussion about the chosen model resolution, the imposed degree-2 strcuture and tables with all parameters characterizing the geodynamical models discussed in the paper.

Text S1.

In order to ensure that our models capture the dynamics of entrainment, we performed resolution tests with three different meshes:

1. 45 nodes in radial and 157 nodes in longitudinal direction, uniform mesh (LR-models)

2. 69 nodes in radial and 237 nodes in longitudinal direction, radially refined in the lowermost 809 km (MHR-models)

3. 91 nodes in radial and 313 nodes in longitudinal direction, radially refined in the lowermost 809 km (VHR-models, used in the main document).

The resolution at the CMB (radial x horizontal) is approximately 65 km x 35 km for LR, 21 km x 23 km for MHR and 17 km x 17 km for VHR. We compared our models using a thermal viscosity contrast of $\eta_{\Delta T} = 65$ by mapping the contours of 20%, 50% and 80% remaining pile mass. The results are shown in Figure S1a-c. As can be seen, more combinations of the buoyancy number B and the compositional viscosity contrast η_C result in piles with more than 80% mass if the resolution is increased. This holds true for the other contour lines as well. However, the lines get flatter in the η_C-B-space, indicating a reduced importance of the excess density while the viscosity remains a controlling factor.

We also performed a few additional tests with even higher resolution (UHR-models, 139 by 481 nodes, thus 10 km x 11 km) for $B = 0.7$, $\eta_{\Delta T} = 65$ and

two different compositional viscosity contrasts of $\eta_C = 10$ (case 1) and $\eta_C = 4$ (case 2). The resulting piles have almost the same mass as for the VHR-cases, the differences being $\sim 1\%$ for the stable pile with $\eta_C = 10$ and $\sim 11\%$ for the unstable und time-dependent case of $\eta_C = 4$. The pile masses retained after 4.5 Gyrs for case 1 with different resolutions (LR, MHR, VHR, and UHR) are compared in Figure S1d. While both LR- and MHR-models result in piles with about 20% remaining mass, VHR- and UHR-models produce piles with $> 80\%$ mass and only minor differences. This confirms that our VHR-models are able to capture the evolution of the pile mass qualitatively well enough for our purpose. Minor adjustments of the contour lines for 20%, 50% and 80% might be expected for resolutions $< 10\,\mathrm{km}$, but they should not affect our general conclusions.
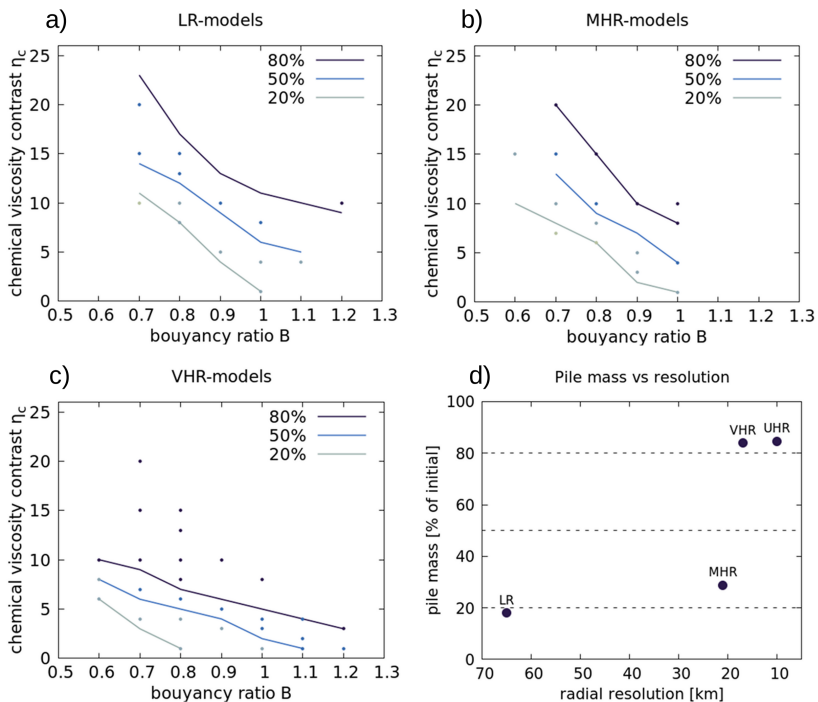

Figure S1: (a)-(c) Contour lines of 20%, 50% and 80% remaining pile mass after 4.5 Gyrs for models with different resolution: (a) LH-models, (b) MHR-models and (c) VHR-models as used in the main text. The thermal viscosity contrast is fixed to $\eta_{\Delta T} = 65$. The general trend of a trade-off between η_C and B is not affected by the resolution, although the necessary η_C value for a given contour decreases with higher resolution. (d) Comparison of obtained pile masses for $B = 0.7$, $\eta_{\Delta T} = 65$ and $\eta_C = 10$ after 4.5 Gyrs with LR-, MHR-, VHR- and UHR-models. Piles for both LR- and MHR-models are in the unstable regime with time-dependent mass, while VHR- and UHR-models result in stable piles of the same mass.

Apart from the resolution, the shape of the chosen elements affects the observed entrainment of the dense material. A few tests with a resolution of 45 by 313 nodes (34 x 17 km at the CMB) and mesh refinement in the lowermost mantle show increased entrainment compared to LR-models, although the higher resolution would suggest the oppsite. However, elements stretched in radial direction significantly overestimate entrainment, even overcompensating the effect of increased resolution. As a consequence, we chose cubic-shaped elements and avoided elongated elements.
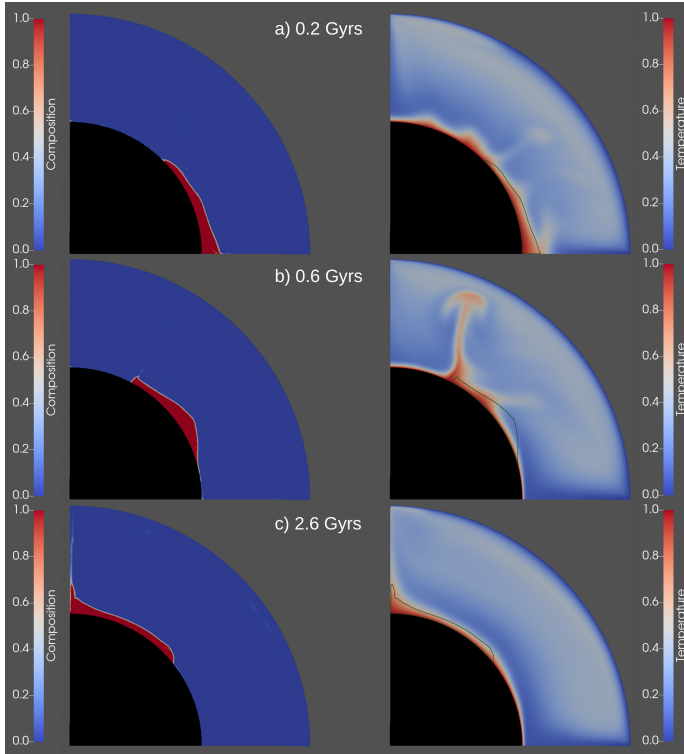
Text S2.

Figure S2: Examples of the temporal evolution for $B = 0.7$, $\eta_C = 7$ and $\eta_{\Delta T} = 65$ for a case in which the imposed surface velocity is reversed after pile formation is completed. (a), (b) and (c) show the compositional field (left) and the corresponding temperature fields (right) for timesteps 0.2 Gyrs, 0.6 Gyrs and 2.6 Gyrs after velocity reversal. Dark lines in the temperature fields indicate the pile shapes for $cl = 0.8$.

To test the affect of the imposed degree-2 pattern on our results, we examined models in which we reversed the plate velocity after succesful formation of the piles. More specifically, we developed piles using models with $B = 1.2$, $\eta_C = 10$

and $\eta_{\Delta T} = 2.3$ after $5.0\,\mathrm{Gyrs}$. We then reversed the plate velocities and forced subduction on top of the pile. An example of 3 snapshots during the temporal evolution of the pile for $B = 0.7$, $\eta_C = 7$ and $\eta_{\Delta T} = 65$ is shown in Figure S2. As can be seen, the pile is initially pushed away from its original position (Figure S2a), gets trapped between the old and the new slab (Figure S2b) until the remaining slab material is heated up sufficiently and finally the pile gets pushed to the opposite boundary (Figure S2c). During this process, the dense material gets deformed and entrainment increases, but remains smaller than during the initial overturn preceeding pile formation.

Table S1: Characteristic parameters for thermochemical calculations. Non-dimensional values are converted according to the scaling laws given in the CitcomS manual[a]. For the conversion of B, we assume a temperature drop across the mantle of $3200\,\mathrm{K}$ and a thermal expansivity of $\alpha = 1 \cdot 10^{-5}$ at the CMB (Tackley, 2012); values give the chemical excess density of the pile material in percent relative to the reference density. Ra is set to 10^8, which results in an effective Rayleigh number of about 10^7 due to the use of the Earth's radius R_0 instead of the mantle thickness d in the definition of Ra.

Parameter	Symbol	Non-dim. value	value [Unit]
Gravitational acceleration	g		9.81 [m/s^2]
Mantle thickness	d	0.45	2891 [km]
Reference density	ρ		$3.34 \cdot 10^3$ [kg/m^3]
Reference viscosity	η	1.0	$1.0 \cdot 10^{21}$ [Pa s]
Thermal diffusivity	κ		$1.0 \cdot 10^{-6}$ [m^2/s]
Thermal expansivity	α		$3.0 \cdot 10^{-5}$ [1/K]
Buoyancy ratio/ chemical excess density	B	0.4-1.2	1.28%-3.84%
Rayleigh number	$Ra = \frac{\alpha\rho g \Delta T d^3}{\eta\kappa}$	10^7	
Internal heating rate	H	10	$2.96 \cdot 10^{-16}$ [W/kg]
Initial thickness of dense layer	d	0.02	127 [km]
Imposed surface velocity	v_{surf}	3000	1.48 [cm/yr]
Compositional viscosity contrast	η_C	1-20	
Thermal viscosity contrast	$\eta_{\Delta T}$	2.3-330	

[a]CitcomS User Manual Version 3.3.0, CIG, www.geodynamics.org.

Table S2: Parameters defining the viscosity profiles according to the thermal viscosity contrast $\eta_{\Delta T}$. Steps for the activation energy E_η, the temperature offset T_η and the viscosity prefactor η_0 are set at non-dimensional depths of 0.047, 0.064 and 0.104, which scale to $299\,\mathrm{km}$, $410\,\mathrm{km}$ and $660\,\mathrm{km}$, respectively. Values are sorted by increasing depth.

$\eta_{\Delta T}$	η_0				E_η				T_η			
2.3	5 /	0.5 /	2.5 /	10	1 /	1 /	1 /	1	0.02 /	0.4 /	0.6 /	0.7
65	5 /	0.5 /	2.5 /	10	1 /	1 /	1 /	1	0.02 /	0.2 /	0.2 /	0.2
330	5 /	0.5 /	2.5 /	5	1 /	1 /	1 /	1	0.02 /	0.15 /	0.15 /	0.15
1700	5 /	0.5 /	2.5 /	5	1 /	1 /	1 /	1	0.02 /	0.12 /	0.12 /	0.12
7500	5 /	0.5 /	2.5 /	5	1.2 /	1.2 /	1.2 /	1.2	0.02 /	0.12 /	0.12 /	0.12